ORTA DOĞU TEKNİK ÜNİVERSİTESİ
FEN BİLİMLERİ ENSTİTÜSÜ MÜDÜRLÜĞÜ

TEZ ŞABLONU ONAY FORMU
THESIS TEMPLATE CONFIRMATION FORM

1. Şablonda verilen yerleşim ve boşluklar değiştirilmemelidir.
2. Jüri tarihi Başlık Sayfası, İmza Sayfası, Abstract ve Öz'de ilgili yerlere yazılmalıdır.
3. İmza sayfasında jüri üyelerinin unvanları doğru olarak yazılmalıdır.
4. Tezin son sayfasının sayfa numarası Abstract ve Öz'de ilgili yerlere yazılmalıdır.
5. Bütün chapterlar, referanslar, ekler ve CV sağ sayfada başlamalıdır. Bunun için **kesmeler** kullanılmıştır. **Kesmelerin kayması** fazladan boş sayfaların oluşmasına sebep olabilir. Bu gibi durumlarda paragraf (¶) işaretine tıklayarak kesmeleri görünür hale getirin ve yerlerini **kontrol edin**.
6. Figürler ve tablolar kenar boşluklarına taşmamalıdır.
7. Şablonda yorum olarak eklenen uyarılar dikkatle okunmalı ve uygulanmalıdır.
8. Tez yazdırılmadan önce PDF olarak kaydedilmelidir. Şablonda yorum olarak eklenen uyarılar PDF dokümanında yer almamalıdır.
9. **Bu form aracılığıyla oluşturulan PDF dosyası arkalı-önlü baskı alınarak tek bir spiralli cilt haline getirilmelidir.**
10. Spiralli hale getirilen tez taslağınızdaki ilgili alanları imzalandıktan sonra, Tez Juri Atama Formu ile birlikte bölüm sekreterliğine teslim edilmelidir.
11. Tez taslağınız bölüm sekreterliğiniz aracılığıyla format ve görünüm açısından kontrol edilmek üzere FBE'ye ulaştırılacaktır.
12. FBE tarafından kontrol işlemleri tamamlanan tez taslakları, öğrencilere teslim edilmek üzere bölüm sekreterliklerine iletilecektir.
13. Tez taslaklarının kontrol işlemleri tamamlandığında, bu durum öğrencilere METU uzantılı öğrenci e-posta adresleri aracılığıyla duyurulacaktır.
14. Tez taslakları bölüm sekreterlikleri tarafından öğrencilere iletileceği için öğrencilerimizin tez taslaklarını enstitümüzden elden alma konusunda ısrarcı olmamaları beklenmektedir.
15. Tez yazım süreci ile ilgili herhangi bir sıkıntı yaşarsanız, **Sıkça Sorulan Sorular (SSS)** sayfamızı ziyaret ederek yaşadığınız sıkıntıyla ilgili bir çözüm bulabilirsiniz.

1. Do not change the spacing and placement in the template.
2. Write defense date to the related places given on Title page, Approval page, Abstract and Öz.
3. Write the titles of the examining committee members correctly on Approval Page.
4. Write the page number of the last page in the related places given on Abstract and Öz pages.
5. All chapters, references, appendices and CV must be started on the right page. **Section Breaks** were used for this. **Change in the placement** of section breaks can result in extra blank pages. In such cases, make the section breaks visible by clicking paragraph (¶) mark and **check their position.**
6. All figures and tables must be given inside the page. Nothing must appear in the margins.
7. All the warnings given on the comments section through the thesis template must be read and applied.
8. Save your thesis as pdf and Disable all the comments before taking the printout.
9. **Print two-sided the PDF file that you have created through this form and make a single spiral bound.**
10. Once you have signed the relevant fields in your thesis draft that you spiraled, submit it to the department secretary together with your Thesis Jury Assignment Form.
11. Your thesis draft will be delivered to the GSNAS via your department secretary for controlling in terms of format and appearance.
12. The thesis drafts that are controlled by GSNAS, will be sent to the department secretary to be delivered to the students.
13. This will be announced to the students via their METU students e-mail addresses when the control of the thesis drafts has been completed.
14. As the thesis drafts will be delivered to the students by the department secretaries, we are expecting from our students no to insist about getting their theses drafts from the Institute.
15. If you have any problems with the thesis writing process, you may visit our **Frequently Asked Questions (FAQ)** page and find a solution to your problem.

☒ **Yukarıda bulunan tüm maddeleri okudum, anladım ve kabul ediyorum. / I have read, understand and accept all of the items above.**

Name : Pelin
Surname : Gündoğmuş
E-Mail : pelin.gundogmus@metu.edu.tr
Date : 30.01.2020
Signature : ________________________

SYNTHESIS OF g-C_3N_4/TiO_2 HETEROJUNCTION COMPOSITES WITH ENHANCED SOLAR LIGHT PHOTOCATALYTIC ACTIVITY

A THESIS SUBMITTED TO
THE GRADUATE SCHOOL OF NATURAL AND APPLIED SCIENCES
OF
MIDDLE EAST TECHNICAL UNIVERSITY

BY

PELİN GÜNDOĞMUŞ

IN PARTIAL FULFILLMENT OF THE REQUIREMENTS
FOR
THE DEGREE OF MASTER OF SCIENCE
IN
METALLURGICAL AND MATERIALS ENGINEERING

JANUARY 2020

Approval of the thesis:

SYNTHESIS OF g-C_3N_4/TiO_2 HETEROJUNCTION COMPOSITES WITH ENHANCED SOLAR LIGHT PHOTOCATALYTIC ACTIVITY

submitted by **PELİN GÜNDOĞMUŞ** in partial fulfillment of the requirements for the degree of **Master of Science in Metallurgical and Materials Engineering, Middle East Technical University** by,

Prof. Dr. Halil Kalıpçılar
Dean, Graduate School of **Natural and Applied Sciences**

Prof. Dr. C. Hakan Gür
Head of the Department, **Met. and Materials Eng, METU**

Prof. Dr. Abdullah Öztürk
Supervisor, **Met. and Materials Eng, METU**

Prof. Dr. Jongee Park
Co-Supervisor, **Met. and Materials Eng, Atılım Uni.**

Examining Committee Members:

Prof. Dr. Caner Durucan
Metallurgical and Materials Eng, METU

Prof. Dr. Abdullah Öztürk
Metallurgical and Materials Eng, METU

Prof. Dr. Jongee Park
Metallurgical and Materials Eng, Atılım Uni.

Prof. Dr. H. Emrah Ünalan
Metallurgical and Materials Eng, METU

Assoc. Prof. Dr. Volkan Kalem
Metallurgical and Materials Eng, Konya Tech. Uni.

Date: 30.01.2020

I hereby declare that all information in this document has been obtained and presented in accordance with academic rules and ethical conduct. I also declare that, as required by these rules and conduct, I have fully cited and referenced all material and results that are not original to this work.

Name, Last name: Pelin Gündoğmuş

Signature:

ABSTRACT

SYNTHESIS OF g-C_3N_4/TiO_2 HETEROJUNCTION COMPOSITES WITH ENHANCED SOLAR LIGHT PHOTOCATALYTIC ACTIVITY

Gündoğmuş, Pelin
Master of Science, Metallurgical and Materials Engineering
Supervisor: Prof. Dr. Abdullah Öztürk
Co-Supervisor: Prof. Dr. Jongee Park

January 2020, 93 pages

The solar light sensitive g-C_3N_4/TiO_2 composites containing various amounts of graphitic carbon nitride (g-C_3N_4) and titania (TiO_2) were prepared by the hydrothermal and sol-gel processes for photocatalytic applications. Hydrothermally derived g-C_3N_4/TiO_2 composites were subjected to regulated heat treatments at temperatures ranging from 350 to 500 ^{o}C for 1 h to improve their photocatalytic efficiency. Particle size, crystal structure, morphology, and optical properties of the g-C_3N_4/TiO_2 nanocomposites were investigated and were compared with those of the pristine TiO_2 and g-C_3N_4 powders using particle size analyzer, X-ray diffractometer, Field emission scanning electron microscope, Fourier transform infrared spectroscopy, Raman spectroscopy, diffuse reflectance spectroscopy (DRS) and UV-Vis spectrophotometer. Photocatalytic activity of all powders was assessed by the Methylene Blue (MB) degradation test under solar light illumination. The results revealed that g-C_3N_4/TiO_2 composites exhibited better photocatalytic activity for the degradation of MB than both pristine TiO_2 and g-C_3N_4. Hydrothermally derived and sol-gel derived g-C_3N_4/TiO_2 composites showed 100% and 87.05%, respectively photocatalytic efficiency under 180 min solar light illumination. The enhancement in photocatalytic activity was related to the generation of reactive oxidation species induced by photogenerated electrons and reduced recombination rate of the electron-hole pairs.

Keywords: Heterojunction, Hydrothermal process, Sol-gel process, g-C_3N_4/TiO_2 composites, Photocatalytic activity.

ÖZ

GELİŞMİŞ SOLAR IŞIK FOTOKATALİTİK AKVİTEYE SAHİP g-C_3N_4/TiO_2 HETEROJONKSİYON KOMPOZİTLERİN SENTEZİ

Gündoğmuş, Pelin
Yüksek Lisans, Metalurji ve Malzeme Mühendisliği
Tez Yöneticisi: Prof. Dr. Abdullah Öztürk
Ortak Tez Yöneticisi: Prof. Dr. Jongee Park

Ocak 2020, 93 sayfa

Farklı miktarlarda grafitik karbon nitrit (g-C_3N_4) ve titanya (TiO_2) içeren solar ışığa duyarlı g-C_3N_4/TiO_2 kompozitleri, hidrotermal ve sol-gel yöntemi kullanılarak fotokatalitik uygulamalar için sentezlendi. Hidrotermal yöntem kullanılarak sentezlenen g-C_3N_4/TiO_2 kompozitleri, fotokatalitik özelliklerini iyileştirmek amacıyla sıcaklığın 350 ile 500 ^oC arasında değiştiği 1 saatlik ısıl işleme tabi tutuldu. g-C_3N_4/TiO_2 kompozitlerinin tanecik büyüklüğü, kristal yapısı, morfolojisi ve optik özellikleri incelendi ve saf TiO_2 ve g-C_3N_4 tozları ile tanecik büyüklüğü analizörü, X-ışını kırınım ölçeri, alan emisyonlu taramalı elektron mikroskopu, Fourier dönüşümlü kızılötesi spektroskopisi, Raman spektroskopisi, Dağınık yansıma spektroskopisi ve UV-vis spektrofotometre kullanılarak karşılaştırıldı. Tüm tozlarının fotokatalitik aktiviteleri solar ışık aydınlatması altında Metilen mavisi (MB) bozunum testi ile değerlendirildi. MB bozunum sonuçları g-C_3N_4/TiO_2 kompozitlerinin saf g-C_3N_4 ve TiO_2 tozlarına göre daha iyi fotokatalitik aktivite sahip olduğunu gösterdi. Hidrotermal ve sol-gel ile üretilen kompozitler 180 dakikalık solar ışık altında sırasıyla %100 ve %87.05 fotokatalitik aktivite gösterdi. Fotokatalitik aktivitedeki artış, fotojenere elektronlar tarafından indüklenen reaktif oksidasyon türlerinin üretilmesi ve elektron-boşluk çiftlerinin rekombinasyonunun azaltılması ile ilgilidir.

Anahtar Kelimeler: Heterojunction, Hidrotermal yöntem, Sol-gel yöntemi, g-C_3N_4/TiO_2 kompozitleri, Fotokatalitik aktivite.

To my family beloved,

ACKNOWLEDGMENTS

I would like to express my deepest thanks to my supervisor, Prof. Dr. Abdullah Öztürk, for his guidance, advice and endless support. Without his patience and encouragement, this thesis would not have been completed.

I also want to thank my co-supervisor Prof. Dr. Jongee Park for his guidance, criticism, encouragements and positivity insight throughout the research.

This work was financially supported by TÜBİTAK with project number 216M391, and METU BAP with project number YLT-404-2018-3751. These financial supports are appreciated.

I want to special thanks to my lovely friends Merve Nur Doğu, Seren Özer, and Anıl Erdal for their endless support, motivations and not letting me give up. I would like to thank Emel Erdal, İbrahim Aydın, Çağlar Karaoğlu, Tolgahan Ulucan, Doğuhan Sarıtürk, Berk Aytuna, also my laboratory neighbors, Esra Karakaya Sütçü, Çağlar Polat and Elif Yeşilay for their support and helps. I appreciate also to my former and new labmates Asmae Bouziani, Sıtkı Can Akkuş, Nursev Erdoğan, Melis Kaplan, Emre Burak Ertuş, Yiğit Cansın Öztürk, Dilara Çisel Varan, and Merve Begüm Köksal.

I would like to thank my close friends Aydın Albayrak, Ayşemine Semerci, İrem Özge Saraç and Seda Ahi for their unconditional supports and motivations.

I am also grateful for all staff of the Metallurgical and Materials Engineering Department, especially Serkan Yılmaz, Gökhan Polat, and Nilüfer Özel for their help and teaching FESEM and XRD analyses.

My deepest gratitude goes to my mother Hülya, my father Tamer, my sister İpek and my cat Muffin for their unconditional love, understanding and emotional support the whole of my life.

TABLE OF CONTENTS

CHAPTERS

LIST OF TABLES

TABLES

LIST OF FIGURES

FIGURES

CHAPTER 1

INTRODUCTION

Energy consumption and environmental pollution are among the two main global problems people face in their daily life in modern societies. In order to solve environmental problems, nowadays semiconductor materials and environmentally friendly processes are practiced [1]. The semiconductors are involved in the production of clean energy by using light for various applications including reduction of carbon dioxide [2], pollutants degradation [3], and hydrogen or oxygen production by water photolysis [4].

In the last three decades, a well-known semiconductor, Titanium dioxide (TiO_2), has received considerable attention from both industry and academia for photocatalytic applications especially for the water remediation processes due to its superior properties including high oxidizing ability, low-cost, long term chemical and biological stability, and non-toxicity [5]. Such highly desirable engineering properties make TiO_2 one of the most commonly practiced photocatalytic materials in both wastewater and air purification treatments. It is also used for the degradation of many organic and inorganic pollutants [6–8]. Despite its pronounced advantages as photocatalytic material, two main drawbacks of TiO_2 restrict its widespread photocatalytic applications. The first one is that it is active only in UV light region of the solar spectrum ($\lambda \leq 388$ nm) because of its larger band gap; c.a. 3.2 eV for anatase, 3.02 eV for rutile, and 2.96 for brookite [9]. The large band gap inhibits its photocatalytic activity under sunlight since only a small portion (~5%) of solar spectrum covers UV as compared to visible region (~45%) [10–12]. The second drawback is related to its low photo quantum efficiency. The fast recombination of photogenerated electron-hole (e^-/h^+) pairs leads to a decrease in the photocatalytic performance [13,14].

Different strategies including doping [15], dye sensitization [16], capping [12] and, semiconductor coupling (coupled/composite TiO_2) [17] have been experienced to improve the photocatalytic efficiency of TiO_2 under sunlight. These strategies are directed towards the enlargement of the absorption wavelength range and enhancement of photocatalytic activity. Among all strategies, semiconductor coupling in other words development of heterojunction with another semiconductor has become very popular in recent years. Heterojunction structure has conjunction between the two semiconductors, and this conjunction inhibits the recombination of e^-/h^+ pairs via transferring photogenerated charge carriers. In heterojunction photocatalysts, the separation of photogenerated e^-/h^+ pairs are promoted through charge transfers between the two semiconductors [18]. Photogenerated holes in the valance band (VB) of TiO_2 transfer to the VB of the other semiconductor and photogenerated electrons in the conduction band (CB) of the other semiconductor transfer to the CB of TiO_2 in TiO_2 based heterojunction composites [19].

Various narrow band gap semiconductors for instance WO_3 [17], ZnO [20], SnO_2 [21], and Fe_2O_3 [22] have been involved to construct heterojunction with TiO_2. Recently, some of the carbonaceous materials like fullerene [23], carbon nitride [24], graphene [25], and carbon nanotubes [26] have been tried to develop heterojunction composites with TiO_2.

Graphitic carbon nitride (g-C_3N_4) is a narrow band gap semiconductor (ca. 2.7 eV) with applicable properties such as good thermal and chemical stability, lightweight, high absorption and acceptable photocatalytic activity in visible light, non-toxicity and, low cost [24,27]. Moreover, it has absorption in the visible light region and photocatalytic activity in the visible light region of the solar spectrum [28–30]. Like TiO_2, g-C_3N_4 has fast recombination rate of e^-/h^+ pairs that restricts its photocatalytic efficiency and limits its photocatalytic applications. However, its band position (−1.3 to +1.4 eV) makes g-C_3N_4 suitable for the production of a heterojunction with TiO_2

[31]. The CB edge potential of g-C_3N_4 is more negative than that of TiO_2. Hence, the photoinduced electrons on the CB of g-C_3N_4 can easily transfer to CB of TiO_2 via the well-developed g-C_3N_4/TiO_2 interface [19]. Also, the more negative VB edge potential of TiO_2 with regard to that of g-C_3N_4 helps easy transfer from the photoinduced holes on the VB of TiO_2 to the VB of g-C_3N_4. For that reasons, g-C_3N_4 with TiO_2 is very promising to produce oxygen and hydrogen via oxidation of organic products. In addition, g-C_3N_4/TiO_2 heterojunction composites have adequate chemical and thermal stability under ambient conditions [32]. Consequently, construction of g-C_3N_4/TiO_2 heterojunction is a promising way to enhance visible light photocatalytic efficiency of both TiO_2 and g-C_3N_4 [33,34].

Production of g-C_3N_4/TiO_2 heterojunction can be achieved through physical admixing of g-C_3N_4 and TiO_2 powders, growing TiO_2 on g-C_3N_4 powders, and loading g-C_3N_4 on TiO_2 powder [1] by various routes including one-pot method [35], solvothermal method [36], ball-milling [37] sol-gel process [38] and, hydrothermal method [39,40]. Production routes of g-C_3N_4/TiO_2 heterojunction photocatalysts directly affect chemistry and morphology of the resultant product and its photocatalytic activity. Hydrothermal method is preferred because it offers controllable synthesis conditions, feasibility, and good crystallinity in the products. Despite a few publications reporting the outcomes of the studies on the g-C_3N_4/TiO_2 heterojunctions by the hydrothermal process, only little is known for the influence of hydrothermal reaction parameters on the construction of g-C_3N_4/TiO_2 composites.

Hydrothermal synthesis conditions like temperature, dwelling time, rotating speed, and volume of the solution in the vessel, etc., directly affect the composite structure [1]. Interfacial interaction influenced also by the synthesis conditions, which in turn affects the photocatalytic properties. The mechanisms taking place during the hydrothermal evolution of heterojunction composites still remain mysterious. Further research is needed to explore the development mechanism of g-C_3N_4/TiO_2 composites and to upgrade their photocatalytic properties under sun like light that comprises UV and visible light depending on the wavelength experienced.

Therefore, a study directed towards the preparation and photocatalytic activity of solar light sensitive g-C_3N_4/TiO_2 heterojunction photocatalysts has both scientific and technological significance.

The aim of the present study is to synthesize solar light sensitive g-C_3N_4/TiO_2 heterojunction photocatalysts by growing TiO_2 nanoparticles on the surfaces of g-C_3N_4 particles by the hydrothermal and sol-gel processes. The effects of synthesis conditions were kept constant but, g-C_3N_4 content of the composite was varied to get a g-C_3N_4/TiO_2 heterojunction photocatalyst with enhanced photocatalytic activity. The photocatalysts prepared were subsequently heat treated at various temperatures. Impacts of the preparation method, amount of the constituents, and the heat treatment temperatures on the structure and photocatalytic efficiency were studied.

CHAPTER 2

LITERATURE REVIEW

2.1 Photocatalysis Phenomena

An alteration of the chemical reaction rates during light exposure is referred to as photocatalysis that was also was defined as acceleration of chemical reaction (generally oxidation and reduction) without consuming a reactant by using light and catalyst [41]. Photocatalytic materials, also known as photocatalysts, are generally semiconductors, which can be alone, or it can combine with metals, organics or inorganics for light absorption. The photocatalytic reactions are categorized to two groups regarding the physical phase of reactants; homogeneous and heterogeneous photocatalysis [27]. When the semiconductor and the reactant have been the same phase that solid, liquid, or gas. This reaction type is named as homogenous photocatalysis. When the semiconductor and the photocatalysis have been in different states, the reaction type is heterogeneous photocatalysis.

Depending on the band gap (Eg) structures, materials are classified in three main groups; conductors, semiconductors, and insulators. Their band gap energies are schematically shown in Figure 2.1 [42].

In presence of light, semiconductors can act as photocatalysts because they have ability to conduct electricity at room temperature. When photocatalyst is exposed to light by enough energy (desired wavelength), the photons with energy is absorbed by electron (e^-) of the valance band (VB) and it is excited to conduction band (CB) leaving behind the hole (h^+) in VB. At the same time, there is an e^-/h^+ pairs formation in this process [41].

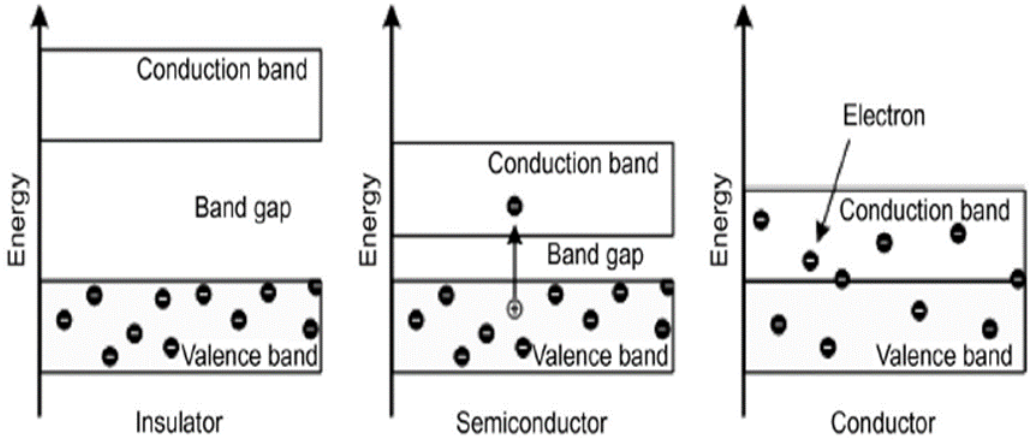

Figure 2.1. Three types of materials as classified regarding their band gap energies [42].

2.1.1 Photocatalytic Materials

Different semiconductors including ZnO [20], Fe_2O_3 [22], g-C_3N_4 [43], $SrTiO_3$ [44], CdS [45], Ag_3PO_4[46], $BiPO_4$ [47], WO_3 [17], and TiO_2 [15] are known as photocatalysts. Band gap energies and the band edge energies of the various semiconductor photocatalysts are tabulated in Figure 2.2. TiO_2 is one of the most commonly practiced photocatalysts due to its powerful ability to degrade many organic and inorganic pollutants resulting from industrial wastes. Because of its superior properties such as high oxidizing ability, low-cost, long term chemical and biological stability, and non-toxicity [5], it is used in special photocatalytic applications to degrade various organic and inorganic pollutants [6–8].

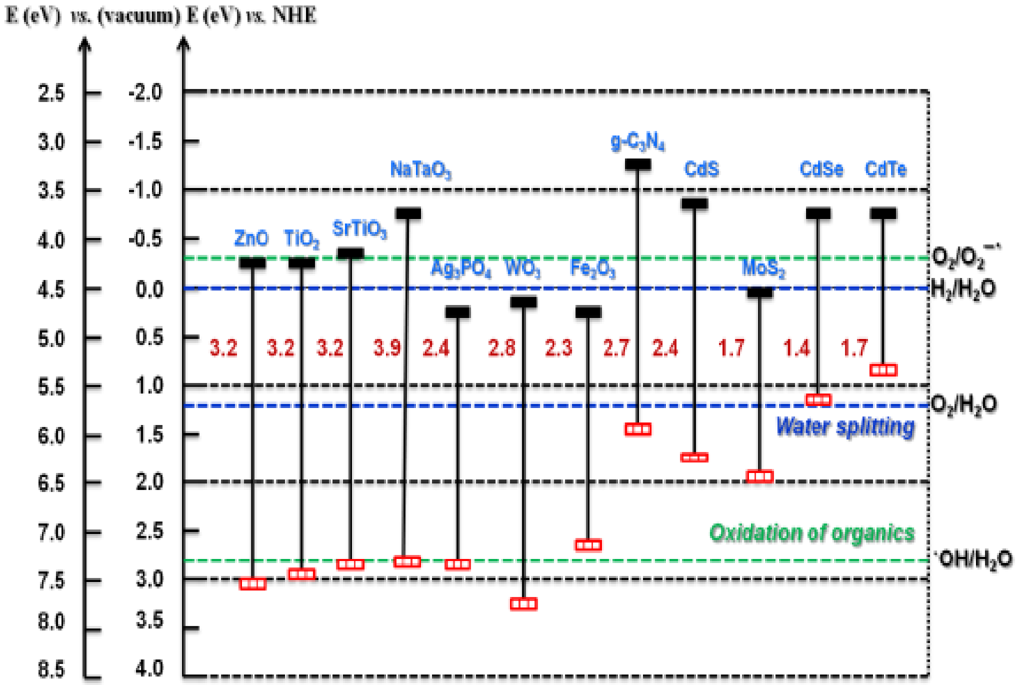

Figure 2.2. Band gap values of selected semiconductors [27].

2.1.1.1 Fundamentals and Mechanism of TiO_2

Photocatalysis is related to the Eg energy of photocatalysts. Irradiation of the photon which is equal to or higher than Eg energy excites the electrons in VB. The excited electrons transfer to CB of the photocatalyst leaving behind the holes. Holes in VB can oxidize donor molecule and react with water molecules to generate hydroxyl radicals which possess strong oxidizing power. At the same time, electrons in VB react with dissolved oxygen for producing superoxide ions. These charge carriers induce the redox reactions [41]. The reactions with the adsorbed components are initiated by the excited e^- and h^+ moving to surface of photocatalyst. The photocatalysis mechanism of TiO_2 in UV/visible light is depicted in Figure 2.3. Hydroxyl ions or adsorbed water can be oxidized from hydroxyl radicals by h^+ in VB. Also, oxygen is transformed to superoxide radicals by helping e^- in CB. Surface of adsorbed molecules degrade by these reactive compounds (superoxide and hydroxyl radicals) [48].

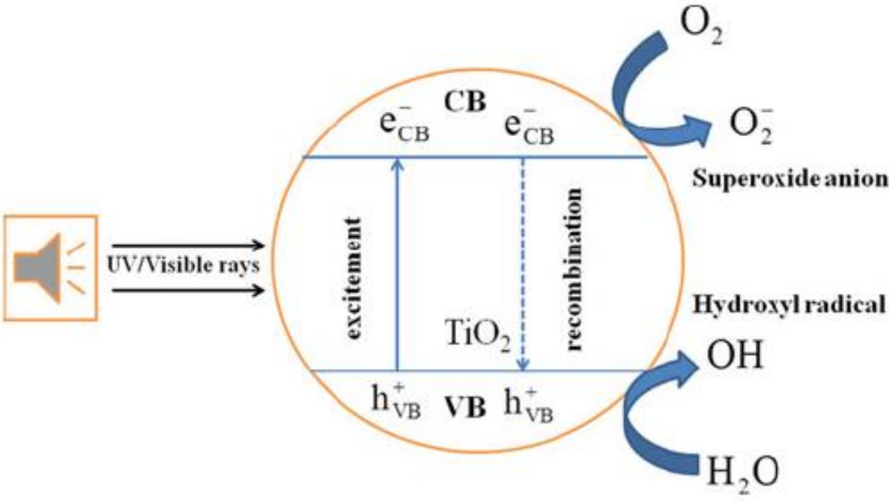

Figure 2.3. Photocatalysis mechanism of TiO_2 under UV/visible light [49].

The redox reactions occurring during photocatalysis phenomena are [48]:

$TiO_2 + h\nu \longrightarrow h^+(VB) + e^-(CB)$ Eq. 2.1

$e^-(CB) + O_2 \longrightarrow {}^\bullet O_2$ (reduction) Eq. 2.2

$h^+(VB) + H_2O \longrightarrow {}^\bullet OH + H^+$ (oxidation) Eq. 2.3

${}^\bullet O_2 + H_2 \longrightarrow HO_2^\bullet$ Eq. 2.4

$e^-(CB) + HO_2^\bullet \longrightarrow HO_2^-$ Eq. 2.5

$HO_2^- + h^+(VB) \longrightarrow H_2O_2$ Eq. 2.6

TiO_2 has four polymorphs namely; anatase, rutile, brookite, and TiO_2(B). Anatase and rutile have tetragonal crystal structure but, brookite and TiO_2(B) have orthorhombic and monoclinic crystal structure, respectively [12]. Crystal structures of TiO_2 polymorphs are shown in Figure 2.4. All polymorphs consist of TiO_6 octahedra while they are different in terms of their stacking [50].

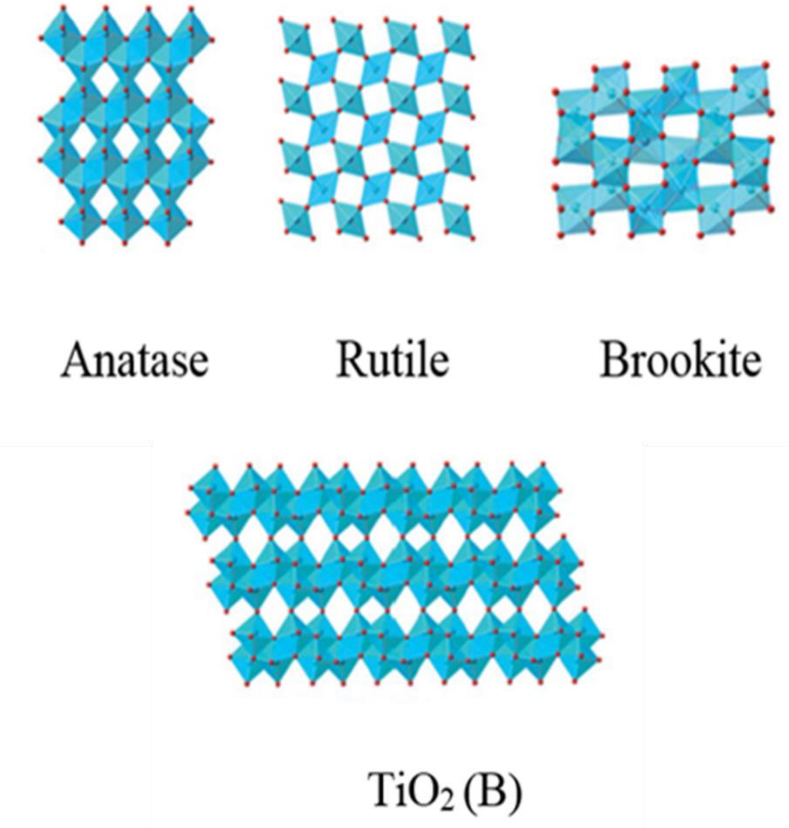

Figure 2.4. Crystal structures of TiO_2 polymorphs [50].

Rutile is thermodynamically the most stable phase. Anatase and brookite are metastable phases, which transform into rutile phase when they are heated [51]. The crystal structure, morphology and particle size of TiO_2 directly affect the properties as well as application areas of TiO_2. Rutile is generally used for pigments, construction, plastic and cosmetic industry, due to its light scattering and reflecting ability, highest density and refractive index [12]. Because anatase crystal structure possesses higher electron mobility and lower density, it is generally used for solar cell and photocatalytic applications. Information about the pure brookite is limited because the synthesis of brookite is extremely difficult [51].

TiO_2 is photoactive only in UV region at wavelengths less than 387 nm because of its large Eg (3.2 eV for anatase) [9,52]. The UV region covers only about 5% of solar spectrum. Also, the photocatalysis efficiency and visible light activation are reduced by the e^-/h^+ recombination. Various strategies have been applied to improve its solar light photocatalytic efficiency. Some strategies developed to decrease Eg and expand the wavelength ranges of the TiO_2 are;

- Doping
    - ✓ Doping with cations
    - ✓ Doping with anions
    - ✓ Co-doping
- Dye sensitization
- Capping
- Coupled/composite with another semiconductor material

2.2 Ways to Enhance Photocatalytic Effectiveness of TiO_2

2.2.1 Dye Sensitization

Dye sensitization is one of the effective way to enhance solar light efficiency, especially for the wide band gap semiconductors like TiO_2 [53]. This process is generally used for enlarging the range of active spectrum. Dye sensitized TiO_2 degrade hydrazine, phenol, pesticide, chlorophenol, and benzyl alcohol [54]. Transition metal-based dyes are good for electron transfer for the semiconductors. However, they are not cheap and not environmentally friendly. Consequently, organic dyes or complexes are commonly used for this purpose. Photocatalytic reaction is initiated when these dyes or complexes inject electrons to the CB of TiO_2 upon exposure to visible light [42].

2.2.2 Doping

Doping with anions or cations is an effective way to broaden the active spectral range of TiO_2 and enhance solar light photocatalytic efficiency. Doping provides the usage of main range of solar light and it traps the joining of photogenerated e^-/h^+ pairs [55]. Doping decreases the band gap of semiconductor by adding impurities. Thus, photocatalytic activity enhances [56]. Every impurity has different effect on crystal structures of semiconductors.

2.2.2.1 Cation-doped TiO_2

Doping of TiO_2 with metallic ions decrease Eg, increase the visible absorption edge and redox potential of TiO_2. Thanks to addition of metal oxides, a new energy develops so that the electrons easily move to catalyst's surface and are trapped with noble metals, earth metals, poor metals and, transition metals. At the same time, the e^-/h^+ recombination rate is hindered by keeping the electrons away from the holes. Separation of the electrons from the holes for longer times enhance the quantum efficiency of TiO_2 [48, 57]. Doping of Fe, Zn, Cu, Ni, Ag, Au, Pt, and V narrow the Eg of TiO_2 [56].

2.2.2.2 Anion-doped TiO_2

Carbon [58], Nitrogen [59], Sulphur [60], and Iodine [61] are the most attractive anionic elements for TiO_2 doping.. When compared to cationic doping, anionic doping minimizes the center of the recombination. The non-metal ions can be replaced by the oxygen vacancies in TiO_2. Thus, Eg is decreased and the visible light photocatalytic activity is enhanced [62].

2.2.3 Coupled/Composite TiO_2

Coupling of TiO_2 with another semiconductors having dissimilar energy levels is an accepted way to improve visible light photocatalytic activity of TiO_2 [63]. In semiconductor coupling, the large Eg semiconductors are coupled with low Eg semiconductors. Electrons in the low Eg semiconductor, that has more negative Eg, transfer to the larger Eg of TiO_2. This process hampers the recombination of e^-/h^+ pairs. Movement of the photogenerated charge carriers depends on the CB and VB potential difference between the two semiconductors. Only the low Eg semiconductor absorbs the visible light, during visible light irradiation [53].

The most popular couples are TiO_2/CdS, TiO_2/WO_3, TiO_2/SnO_2, TiO_2/MO_3 and, TiO_2/Fe_2O_3. Nano carbon based photocatalysts like carbon nanotubes (CNT) and graphene have been tried recently. Graphitic carbon nitride (g-C_3N_4) coupled with TiO_2 has been shown to improve visible light photocatalytic activity of TiO_2. They possess good chemical stability, high mechanical strength, and high specific surface area. These components supply rapid heat and electron transfer. Also, organic compounds were absorbed by these nano carbons in aqueous solutions [26,64].

2.3 Graphitic Carbon Nitride (g-C_3N_4)

Carbon nitride (C_3N_4) has five allotropes namely; α- C_3N_4, β-C_3N_4, cubic- C_3N_4, pseudocubic-C_3N_4, and graphitic C_3N_4. Graphitic carbon nitride (g-C_3N_4) is the most stable allotrope of carbon nitride class under ambient conditions [65]. g-C_3N_4 with various structures and properties can be synthesized using various methods like chemical vapor deposition (CVD), physical vapor deposition (PVD), solid state, solvothermal, ionothermal synthesis, thermal condensation, and single step nitration. Among all the synthesizing routes, thermal condensation with nitrogen-rich solutions is the most prevalent method. Some of the nitrogen-rich sources are melamine, urea, thiourea, cyanamide, dicyanamide, triazoles and guanidine which are cheap, accessible and easily producible.

In recent years, g-C_3N_4 has appealed considerable attention for visible light photocatalytic applications. It has superior visible light photocatalytic activity to many metal oxide semiconductors because of its low Eg energy (ca. 2.7 eV) as compared to TiO_2 [66]. It has remarkable properties for example good chemical stability, low density, and high absorption and acceptable photocatalytic activity in visible light [67]. It is insoluble in water, ethanol and diethyl eter and toluene which are the most popular solvents. It is resistive to acidic and basic medias due to its Van der Waals forces [68]. Dong et al. [18] published that g-C_3N_4 is non-volatile up to 600 °C but, decomposes at 700 °C. Additionally, g-C_3N_4 is non-toxic, cheap, easily fabricated from nitrogen-rich solutions, and available for enhancing electronic and optical properties [69]. Moreover, its Eg position (-1.3±1.4 eV) makes it suitable for heterojunction construction with TiO_2 [30]. Although g-C_3N_4 has good optical and electronic properties, utilization of g-C_3N_4 in photocatalytic applications is limited due to its low photocatalytic efficiency in visible light. Small specific surface area (4-26 m^2/g), lower electrical conductivity, and fast recombination of e^-/h^+ pairs are other disadvantages restricting the widespread application of g-C_3N_4 in photocatalytic applications [70]. The recombination of photogenerated charge carriers hampers the formation of radical species responsible for the redox reaction during photocatalytic reactions. Smaller specific surface area negatively affects the light harvesting and reduces the separation time of the charge carriers [70,71]. An Eg of 2.7 eV is large for efficient visible light spectrum [72].

In order to improve charge separation and surface area of g-C_3N_4 hence photocatalytic activity, various nanostructures such as nanoribbons, nanobelts, nanoparticles etc. can be engineered [73] or another modification can be applied by using organic dyes and polymers. But, coupling with other semiconductors (construction of a heterojunction) have been among the most popular strategies practiced in recent years [74]. Creation of g-C_3N_4/TiO_2 heterojunction is an encouraging way to improve visible light photocatalytic activity of both TiO_2 and g-C_3N_4 [75].

2.4 g-C_3N_4/TiO_2 Nanocomposite

In heterojunction systems, the separation time for the charge carriers are encouraged through charge transfers between the two semiconductors so that e^-/h^+ recombination rate is reduced and photocatalytic activity of the both constituents are enhanced.

Additionally, TiO_2 nanoparticles are combined with the g-C_3N_4 nanosheets by simple and environmentally friendly methods. Because of the enhanced photocatalytic activity and easy production, they have found various promising applications such as production of clean energy and waste water treatment [30,39].

2.4.1 Production Methods of g-C_3N_4/TiO_2 Nanocomposite

Some researchers [30,66,74] have tried different methods to produce g-C_3N_4/TiO_2 nanocomposites. Production techniques of the g-C_3N_4/TiO_2 can be classified into three main groups [1].

2.4.1.1 Physical Mixing of g-C_3N_4 and TiO_2

In this method, g-C_3N_4 and TiO_2 are synthesized separately. After that, these two constituents are mixed by using physical mixing methods like ball mill or solvent evaporation. Yan et al. [75] produced g-C_3N_4 by heating the melamine powder under Ar gas atmosphere, and TiO_2 was synthesized by using $TiCl_4$ as a precursor. After synthesizing two components individually, g-C_3N_4/TiO_2 heterojunction structure was obtained by ball milling method. Zhou et al. [37] applied the same method to prepare g-C_3N_4/TiO_2 hybrid structure. They first heated melamine to produce layered structure of g-C_3N_4. Then, they utilized the commercial TiO_2 powder, and mixed it with the synthesized g-C_3N_4. By this way, they achieved a highly photoactive g-C_3N_4/TiO_2 heterostructure.

Evaporation of the dispersion solution is another physical method for synthesizing the g-C_3N_4/TiO_2 heterostructure powders. In this method, both components are dissolved in a solvent that is evaporated until a connection between g-C_3N_4 and TiO_2 structures is made [76,77]. TiO_2 nanosheets are synthesized using tetra butyl titanate (TBOT) as a precursor by solvothermal reaction. Urea is calcined to obtain g-C_3N_4. After that, both constituents are dispersed into methanol and the mixture is sonicated for 30 min to complete dispersion. Later, methanol is evaporated, remaining powder is dried, and heterostructure is obtained.

These physical synthesis methods are easy methods for mass production but, they are not easy for the control of the consequential morphology. Also, connection between the two powders has lower stability compared to the heterojunction catalysts prepared by other methods [1].

2.4.1.2 Loading g-C_3N_4 on TiO_2

First TiO_2 is prepared by any one of the processes. Then, the TiO_2 produced is added into a g-C_3N_4 precursor solution. After washing, filtering, drying and, calcination g-C_3N_4/TiO_2 nanocomposite is obtained. Wang et al. [77] first synthesized TiO_2 nanorods hydrothermally. Then, they produced g-C_3N_4 using melamine as a precursor through CVD. After that, a fluorine doped tin oxide (FTO) glass was coated by TiO_2 in an autoclave. Next, the TiO_2 coated FTO was treated with melamine so that g-C_3N_4/TiO_2/FTO is obtained. This heterojunction shows photocatalytic activity 10 times better than pure TiO_2/FTO under visible light.

Boonprakob et al. [78] utilized Titanium tetra isopropoxide (TTIP) as a TiO_2 precursor. After hydrolysis and condensation of TTIP solution, TiO_2 nanoparticles were obtained. The TiO_2 nanoparticles and melamine were directly mixed to produce g-C_3N_4/TiO_2 films under Ar flow. Their results revealed that the composite containing 50 wt% g-C_3N_4 shows enhanced photocatalytic efficiency

2.4.1.3 Growing of TiO_2 Nanoparticles on g-C_3N_4 Surface

First g-C_3N_4 is synthesized. Then, TiO_2 precursor is introduced to the g-C_3N_4 synthesized for the growth of TiO_2 on the g-C_3N_4 surfaces. Lu et al. [79] applied this routine to produce of g-C_3N_4/TiO_2 hybrid nano composite with higher photocatalytic activity than phase pure constituents under both UV and the visible light. Shen et al.

[80] produced g-C_3N_4/TiO_2 hybridized structure by using template-free method. First, melamine was heated to obtain g-C_3N_4. Then, synthesized g-C_3N_4 was added to titanium sulfate $Ti(SO_4)_2$ solution. After that, hydrothermal reaction was allowed to produce g-C_3N_4/TiO_2 nanocomposite. Synthesized nanocomposite possesses superior visible light photocatalytic activity.

Growing TiO_2 is an operational way for the construction of g-C_3N_4/TiO_2 hetero structure even though fully dispersion of TiO_2 is difficult on the surface of g-C_3N_4 because of the rapid hydrolysis ability of titanium precursors. Also, the heterojunctions prepared by this way has higher chemical stability [1,81].

There is no difference between resulting structures of the products prepared by the three different methods [1]. Nevertheless, growing of TiO_2 nanoparticles on g-C_3N_4 surface method was chosen in this study to produce g-C_3N_4/TiO_2 heterojunction photocatalysts due to its advantages over the other methods.

2.4.2 Production Routes of g-C_3N_4/TiO_2 Nanocomposites

g-C_3N_4/TiO_2 nanocomposites are produced through different production routes including one-pot method [35], solvothermal method [36], ball-milling [37], sol-gel process [82], and hydrothermal process [83]. In this section a brief information for the sol-gel and hydrothermal processes will be given since these methods were selected to produce g-C_3N_4/TiO_2 nano composites in this study.

2.4.2.1 Hydrothermal Process

Hydrothermal method enables scientists to control mechanisms of diffusion kinetics, crystallinity and purity of the product, and temperature and time of the reaction(s) taking place during processing. The hydrothermal reactions are also affected by pH and viscosity of the prepared solution [83]. Hao et al. [84] prepared g-C_3N_4/TiO_2 heterojunction photocatalysts by dissolving some amount of melamine in DI water to obtain a homogeneous solution. After that, $TiCl_4$ solution was added into the mother solution dropwise and the resultant white solution was transferred to an autoclave. Reaction occurred at 180 ºC for 4 h. Following washing and drying process a g-C_3N_4/TiO_2 heterojunction composite was produced.

2.4.2.2 Sol-gel Process

Dispersion of colloidal particles in fluid media is referred to as sol. Water, air, organic liquids and aerosol can be fluid media. The sol-gel process can be employed for the production of different products like ceramics, abrasive minerals, membranes, films, and catalysts under ambient temperatures. In sol-gel process, there are five main steps. First, precursor is mixed with sol or solution to allow hydrolysis and condensation reactions. Then, chemical reactions yield gelation that is followed by drying. Finally curing is applied. Some of the main advantages of this process are lower processing temperature, sample purity, easy control of dopant concentrations, and synthesizing multicomponent compositions in various product forms [85,86].

Sun et al. [82] produced g-C_3N_4/TiO_2 composites by modified sol-gel process. First, they prepared g-C_3N_4 suspension by mixing g-C_3N_4 powder with ethanol. TBOT was introduced to suspension during magnetic stirring. Then, water and ethanol was added while stirring continues until TiO_2 colloids immobilize onto g-C_3N_4. After that, the product obtained was dried and exposed to heat treatment.

CHAPTER 3

EXPERIMENTAL PROCEDURE

3.1 Materials

Titanium tetra isopropoxide (TTIP, 97%) and melamine powder (2,4,6 Triamino-1,3,5-triazine, 99%) were used as TiO_2 precursor and g-C_3N_4 precursor, respectively to prepare g-C_3N_4/TiO_2 photocatalysts by the hydrothermal process. Nitric acid (HNO_3, 70%) was employed as catalyzer. All chemicals were purchased from Sigma Aldrich. Deionized water (DI) was used for the preparation of solutions. Ethanol (96%, Limko) was used as solvent for the sol-gel synthesis. Methylene Blue (MB, 97%) was utilized as a dye for photocatalytic activity measurements. Except HNO_3, all chemicals were analytical grade and were used without purification.

3.2 Powder Synthesis

Heterojunction photocatalysts were synthesized via hydrothermal and sol-gel routes.

3.2.1 g-C_3N_4/TiO_2 Powder Preparation by the Hydrothermal Process

Hydrothermal synthesis of TiO_2 and g-C_3N_4/TiO_2 powders were achieved in a Teflon lined vessel made from hast alloy in a high-pressure reactor (ITO Instruments® Imax). The vessel had 300 mL volume. The working principle of the reactor includes various variables such as dwell time, temperature, and pressure. This system involves a magnetic stirrer which is also covered by Teflon. The speed of the magnetic stirrer could be adjusted between 0 to 1500 rpm. Synthesis temperature is set in a range between 0 and 1000 °C. The pressure changes autogenously depending on the temperature, solution type, and solution volume present in the vessel. The hydrothermal system has also a cooling system to keep the solution in desired temperature. In this study, acidic hydrothermal method was used to produce g-C_3N_4/TiO_2 heterojunction photocatalysts using HNO_3 as catalyzer.

3.2.1.1 Preparation of the g-C_3N_4 Powder

g-C_3N_4 powder was prepared through heat treatment of melamine powder according to the procedure as described by Tong et al. [19]. First, predetermined amount of melamine powder was placed into an alumina crucible and heated to 550 °C at a heating rate of 2 °/min in an electrical furnace. It was kept at this temperature for 4 h then, cooled to room temperature without controlling the cooling rate but turning the power of the furnace off. After that, the resulting yellow agglomerate was collected and ground by using mortar with pestle to obtain g-C_3N_4 powder. The photograph of g-C_3N_4 powder is shown in Figure 3.1 (a).

3.2.1.2 Preparation of the g-C_3N_4/TiO_2 Powder

The g-C_3N_4/TiO_2 heterojunction photocatalysts were synthesized in one step hydrothermal synthesis by growing of TiO_2 nanoparticles on the surfaces of g-C_3N_4 powders. First, necessary amount of g-C_3N_4 powder was mixed with 118 mL of DI water. Then, this mixture was sonicated by ultrasonic liquid processor (Misonix XL2020^{TM}, NY, US) at 20 kHz vibration frequency for 30 min to disperse the size of g-C_3N_4 sheets and to produce homogeneous suspension. Before catalyzer addition, some time was allowed to reduce the temperature of the suspension to room temperature since sonication increased the temperature of the suspension. After cooling to room temperature, the suspension was magnetic stirred at 200 rpm for 0.5 h. Then, 0.833 mL of HNO_3, used as catalyzer, was added into the suspension to get acid molarity of 0.1 M. Next, 6.67 mL of TTIP was introduced to the yellow color suspension dropwise while magnetic stirring. The TTIP was addition was done at 300 rpm for 30 min.

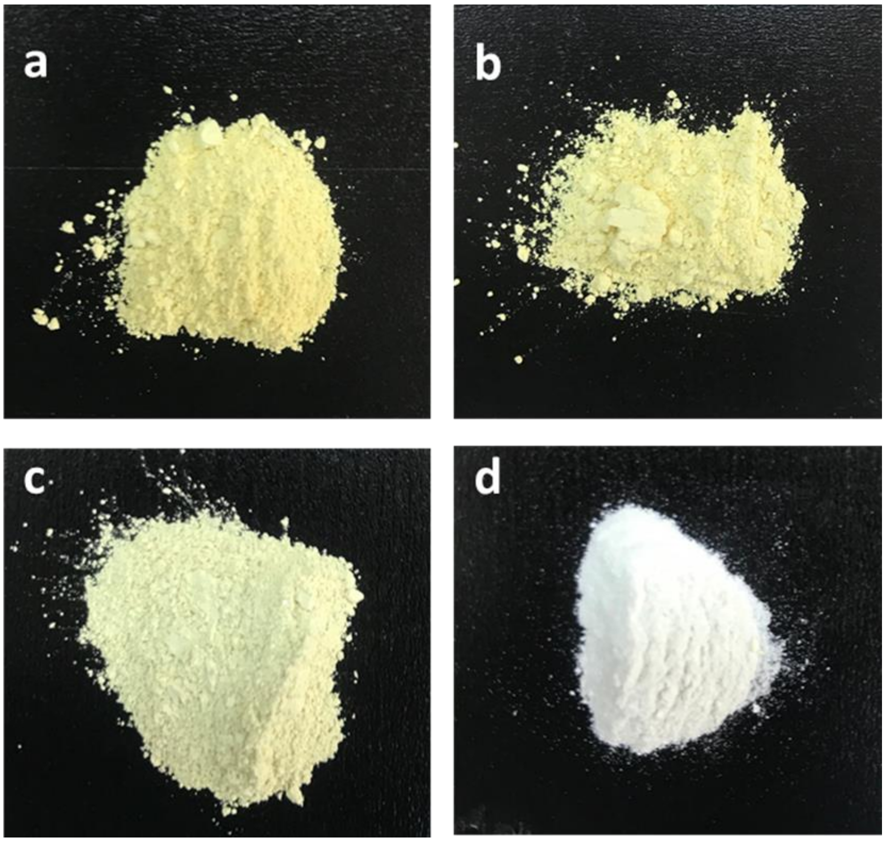

Figure 3.1. Photographs of some of the hydrothermally derived powders. a) g-C_3N_4, b) TCN-80, c) TCN-20, and d) TiO_2.

After all, TTIP was dissolved in the suspension, the resultant solution was transferred into the vessel of high-pressure reactor with 300 mL capacity. The hydrothermal synthesis was performed at 110 °C for 1 h. The pressure of the vessel varied autogenously between 0 and 10 bar. After hydrothermal synthesis, the resultant product in light yellow color was collected and washed with DI water several times until the pH become neutral. This product was centrifuged and dried at 80 °C for 24 h. Finally, the dried agglomerates were ground using mortar with pestle to get g-C_3N_4/TiO_2 powder. The steps involved in the hydrothermal synthesis of g-C_3N_4/TiO_2 powders are shown in Figure 3.2.

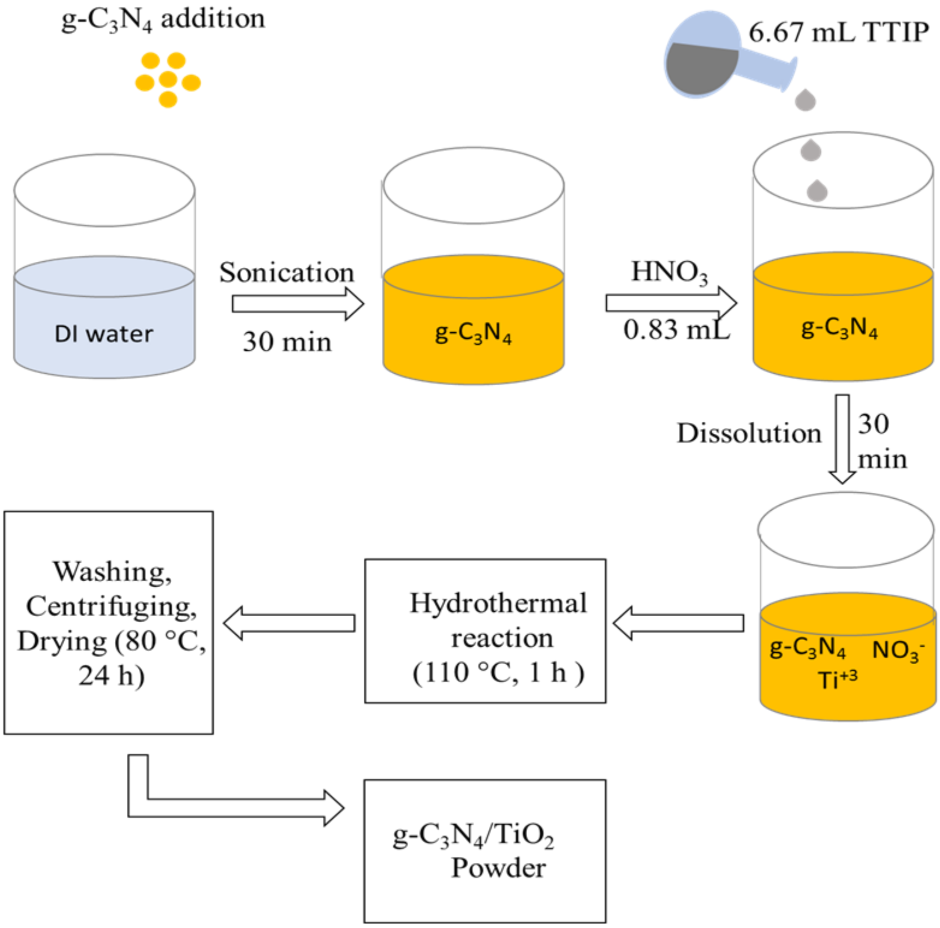

Figure 3.2. Flowchart showing the steps involved in the hydrothermal synthesis of g-C_3N_4/TiO_2 powders.

The g-C_3N_4/TiO_2 powders synthesized were named based on their g-C_3N_4 content as TCN-XX, where the last two digits represent the amount (in weight percentage, wt%) of g-C_3N_4 involved in the powder. The TCN-80 powder was subjected to heat treatment at various temperatures ranging from 350 to 500 ^{o}C for 1 h. The heat-treated powders were named with respect to the temperature applied as TCN-80-XXX, where the last three digits represent the temperature applied during heat treatment. Codes of the g-C_3N_4/TiO_2 powders synthesized were presented in Table 3.1. Photographs of TCN-20 and TCN-80 powders are shown also in Figure 3.1 (b) and (c).

Table 3.1 Code of the hydrothermally derived g-C_3N_4/TiO_2 powders.

Powder code	g-C_3N_4 content (wt%)	TiO_2 content (wt%)	Calcination Temperature (°C)
TCN-20	20	80	-
TCN-50	50	50	-
TCN-60	60	40	-
TCN-70	70	30	-
TCN-80	80	20	-
TCN-90	90	10	-
TCN-80-350	80	20	350
TCN-80-400	80	30	400
TCN-80-450	80	20	450
TCN-80-500	80	20	500

3.2.1.3 Preparation of TiO_2 Powder

In addition to g-C_3N_4/TiO_2 powders, TiO_2 powders were hydrothermally synthesized in the same experimental conditions to compare the photocatalytic properties of g-C_3N_4/TiO_2 and TiO_2 powders prepared at the same conditions. First, 0.833 mL of HNO_3 was mixed with 118 mL of DI water to obtain acid molarity of 0.1 M. Then, 6.67 mL of TTIP was added dropwise into the acid solution during magnetic stirring for 30 min. After complete dissolution of the TTIP in the solution, a homogeneous and transparent solution was obtained. This homogeneous solution was transferred into the vessel of the high-pressure autoclave. Then, hydrothermal reaction was allowed to occur at 110 °C for 1 h. After the hydrothermal synthesis, the solution was cooled in the vessel to room temperature. After that it was collected, washed for several times, centrifuged and dried at 80 °C for 24 h in an oven. The synthesized product was TiO_2 powder and was named as TiO_2. Some amount of the TiO_2 powder was exposed to heat treatment at 400 °C for 1 h. The heat treated TiO_2 powder was named as TiO_2-400.

3.2.2 g-C_3N_4/TiO_2 Powder Preparation by Sol-gel Process

3.2.2.1 Preparation of g-C_3N_4/TiO_2 Powder

The first step in the synthesis of g-C_3N_4/TiO_2 powders via sol-gel method was the same as that of TiO_2 powder. First, 54.75 mL of ethanol was diluted with 67.5 mL of DI water and 0.275 mL of HNO_3 was added into this solution. Then, 18.5 mL of TTIP was supplemented dropwise. The solution was stirred until all TTIP was dissolved. Dissolution process took approximately 1 h. After that, predetermined amount of g-C_3N_4 powder that varied according to weight percentages of g-C_3N_4 in the g-C_3N_4/TiO_2 composite was added into the solution. The solution containing g-C_3N_4 powder was mixed at 300 rpm for 48 h using a magnetic stirrer. Later, the solution was washed with DI water for several times until pH became neutral, centrifuged at 6000 rpm for 10 min, and dried at 80 °C for 24 h. The dried agglomerates were collected and ground using mortar with pestle to get g-C_3N_4/TiO_2 powder. The steps involved in the sol-gel synthesis of g-C_3N_4/TiO_2 powders are shown in Figure 3.3.

Some amount of the sol-gel derived g-C_3N_4/TiO_2 powder was exposed to a regulated heat treatment at 400 °C for 2 h. The heating rate was 5 °/min. The g-C_3N_4/TiO_2 powders derived by the sol-gel process were named based on their g-C_3N_4 content as STCN-XX, where the last two digits represent the amount (in weight percentage, wt%) of g-C_3N_4 involved in the powder. All the sol-gel derived powders were heat treated at 400 ^{o}C for 1 h. Codes of the sol-gel derived g-C_3N_4/TiO_2 powders are shown in Table 3.2. Photographs of STCN-80 and STCN-20 powders are shown in Figure 3.4 (a) and (b), respectively.

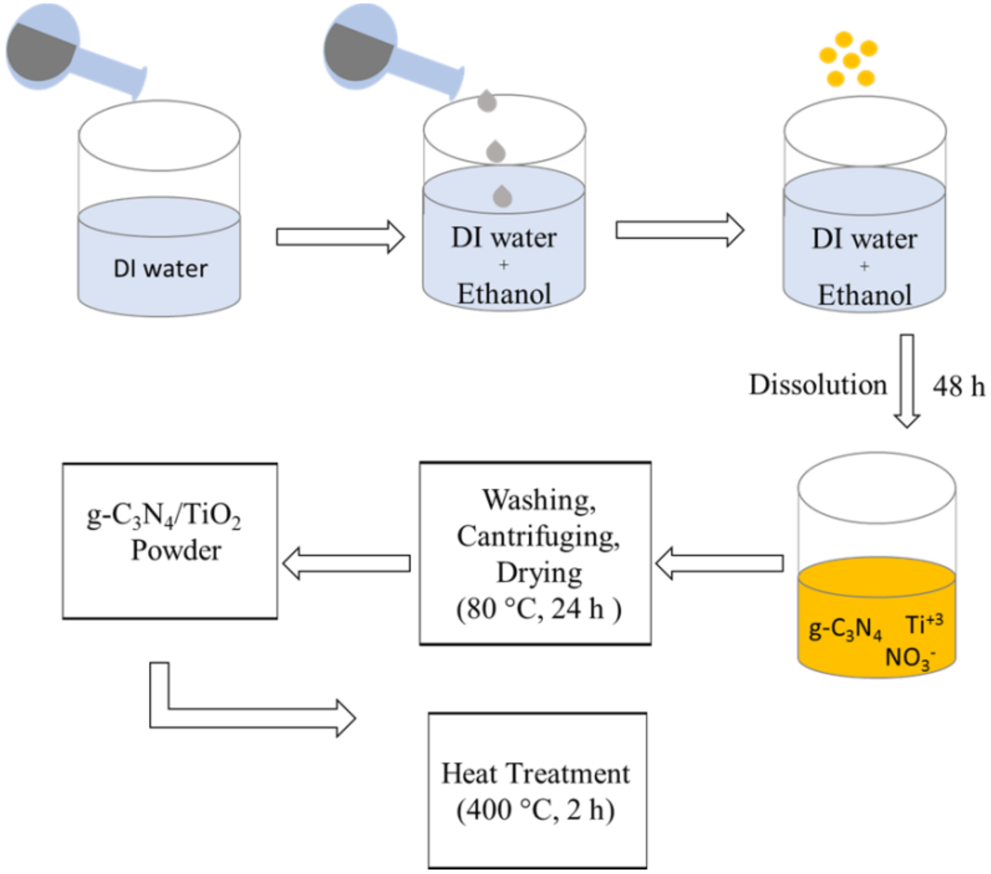

Figure 3.3. Flowchart showing the steps involved in the sol-gel synthesis of g-C_3N_4/TiO_2 powders.

Table 3.2 Codes of the sol-gel derived powders.

Powder code	g-C_3N_4 content (wt%)	TiO_2 content (wt%)	Calcination temperature (°C)
$STiO_2$	-	100	400
STCN-20	20	80	400
STCN-50	50	50	400
STCN-80	80	20	400

Figure 3.4. Photos of some of the sol-gel derived powders. a) STCN-80, b) STCN-20, and c) $STiO_2$.

3.2.2.2 Synthesis of TiO_2 Powder

In addition to $g\text{-}C_3N_4/TiO_2$ powders, TiO_2 powders were synthesized by the sol-gel process in the same experimental conditions to compare the photocatalytic properties of $g\text{-}C_3N_4/TiO_2$ and TiO_2 powders prepared at the same conditions. First, 67.5 mL of DI water was mixed with 54.75 mL of ethanol in a glass beaker. Then, this mixture was blended during magnetic stirring at 150 rpm for 30 min. Next, 0.275 mL of HNO_3 was added into solution as a catalyzer to get 0.1 M acid molarity. After that, 18.5 mL TTIP was added into the solution dropwise while magnetic stirring at 300 rpm for 48 h. After 48 h, all TTIP dissolved in the solution and a white milky solution was obtained. This solution was washed with DI water several times until pH become neutral. Finally, the resultant solution was filtered and centrifuged at 6000 rpm for 10 min. The agglomerates collected were dried at 80 °C for 24 h in an oven. The agglomerates synthesized were ground using mortar with pestle. At the end, approximately 3 g of TiO_2 powder was obtained. Some amount of the TiO_2 powder was exposed to a regulated heat treatment at 400 °C for 2 h at a heating rate of 5°/min. The powders had white color after heat treatment and were named as $STiO_2$ as shown in Figure 3.4 (c).

3.3 Characterization of the Powders

3.3.1 Particle Size Analysis

Particle size analysis of the powders prepared was done using a particle size analyzer (Mastersizer 2000, Malvern Panalytical, Malvern, UK). It measures the size of particles in the range from 0.01 to 3000 μm. It uses both helium neon and solid-state light source for coarser and finer particles, respectively.

3.3.2 X-Ray Diffraction (XRD) Analysis

XRD analysis was done to identify of the phases present in the powders prepared using an X-Ray diffractometer (AXS D8 Advance A25, Bruker, Tokyo, Japan). Powders were scanned in the two-theta range between 10 and 70° at a scanning rate of 2°/min using CuKα radiation at wavelength (λ) of 1.5406 Å. The applied voltage and current were 40 kV and 40 mA, respectively. The peak positions and their intensities for the phases developed were quoted from the Joint Committee on Powder Diffraction Standards (JCPDS) database. The verification of the phase identification was confirmed using Diffrac. Eva. 3.1 software program.

Size of crystallites was calculated from the diffraction line of XRD assuming all the crystallites have spherical shape by using Debye-Scherrer formula [87]:

$$D = \frac{0.9}{\beta\cos\theta} \qquad \text{Eq. 3.1}$$

where;

λ: 0.154056 nm and represents the X-ray wavelength from Cu Kα radiation

β: full width at half maximum (FWHM).

3.3.3 Field Emission Scanning Electron Microscopy (FESEM) and Elemental Analysis

Size, shape, and morphology of the powders synthesized were examined by field emission scanning microscope (FESEM, Nova, Nanosem) at an operating voltage range between 18 and 20 kV. Before FESEM analysis, all powders were coated by gold using gold sputter (Quorum SC7640, UK) to get desired conductivity. Elemental and compositional analyses were done using an energy dispersive X-ray spectrometer (EDS, JEOL 2100 F, Tokyo, Japan). EDS was operated at 20 kV.

3.3.4 Fourier Transform Infrared Spectra (FT-IR) Analysis

FT-IR analysis was applied to identify chemical structures and molecular interactions of the powders synthesized using an FTIR spectrometer (Perkin Elmer, USA). Before the analysis, the powder was mixed with the conventional KBr powder. The synthesized powder to KBr weight ratio was 3:200. Then, the mixture was uniaxially pressed (~7 tons, for 40 sec) to form pellets. FT-IR data was collected in a range between 4000 cm^{-1} and 500 cm^{-1} by using absorbance mode.

3.3.5 Raman Spectroscopy Analysis

Raman spectroscopy analysis was performed to identify crystalline phases present in the powders synthesized using dispersive Raman spectrometer (Renishaw in Via Raman Microscope, UK). Powders were analyzed using ccd detector with an excitation of 785 nm/300 mW variable diode laser light. Analyses were conducted at a range between 100 cm^{-1} and 1600 cm^{-1} Raman shifts.

3.4 Property Measurements of the Powder

3.4.1 Diffuse Reflectance Spectra (DRS) Analysis

The band gap measurements of the powders were performed using a diffuse reflector apparatus attached to the UV-Vis spectrophotometer (Scinco, S-3100, Korea). First, measurement was done at dark. Then, a completely white blank sample was measured to obtain baseline. White blank measurements were applied depending on the USRS-99-010 standard. After these measurements, measurements of the synthesized powders were done. The band gap values of the powders are calculated using following equation [88].

$$\alpha hv = A(hv - Eg)^{n/2} \qquad \text{Eq. 3.2}$$

where;

α: absorption coefficient

hv: photon energy

A: constant

Eg: the band gap energy

n=1 for direct transition, and n=4 for indirect transition.

Absorbance percent versus wavelength graph was transformed to $(\alpha hv)^2$ versus hv plot. Then, Eg values of the powders were read from the intercept of the tangent point in X axis (hv) of the graph.

Also, conduction band and valance band potentials of the pristine TiO_2 and the g-C_3N_4 powders were calculated using the formulae given below.

$E_{VB} = X - E^e + 0.5Eg$ Eq. 3.3

$E_{CB} = E_{VB} - Eg$ Eq. 3.4

where;

E_{VB} and E_{CB}: valance band and the conduction band potentials, respectively

E^e: energy of free electrons on the hydrogen scale which is ~4.5 eV

Eg: the band gap values of the semiconductors

X: geometric means of electronegativity values of the components of the semiconductors. X values of TiO_2 and g-C_3N_4 were taken 5.81 and 4.73 eV, respectively [89].

3.4.2 Photocatalytic Activity Measurements

The photocatalytic activity of the powders synthesized was evaluated through methylene blue (MB) degradation test under 500 W Xenon lamp (XSS-5XD, Shangai Biological Science Inc, China) using a UV-Vis spectrophotometer (Scinco, S-3100). First, an aqueous MB solution was prepared by dissolving 0.01 g of MB powder in 1 L of DI water during magnetic stirring to obtain an initial MB concentration of 10 ppm. MB is affected from the daylight. Thus, this solution was prepared in dark.

For the activity measurements, 0.1 g of the powder synthesized was mixed with 100 mL of the aqueous MB solution. Before exposing the suspension to Xenon light, it was magnetic stirred continuously in dark for 30 min in a homemade wooden box to assure the absorption/desorption equilibrium. Then, 4 mL of this suspension was taken in every 5 min using syringe filters (Millex Millipore, 0.22 µm) and transferred to the UV-Vis spectrophotometer for measurement. It was recognized that absorption/degradation equilibrium was achieved after 30 min. Accordingly, dark stirring step of the MB degradation test was 30 min for all experiments.

Degradation of DI water was measured using run blank button of the spectrophotometer to get a baseline, then MB solution without any powder addition was measured using run sample button of the spectrophotometer to get a reference. For the MB degradation test of the powders synthesized, 50 mg of the synthesized powder was mixed with 50 mL of the MB solution inside of the wooden box. Prepared suspension was kept for 30 min in dark while magnetic stirring to measure absorbance values. After dark measurement, Xenon lamp was turned on. Then, 4 mL of this suspension was taken in every hour using syringe filters and transferred to the UV-Vis spectrophotometer for measurement. After 1, 2 and 3 h under solar (UV + Vis) light illumination degradation of MB was measured.

UV-Vis spectrophotometer gives absorbance data in a range between 200-800 nm. Top value of the peaks corresponds to 664 nm. Thus, photocatalytic activity calculation was done according to the following equation:

$$\text{Degradation } \% = (C_o - C)/C_o \times 100 \qquad \text{Eq. 3.5}$$

where;
C_o: initial concentrations of the MB and
C: concentrations of MB at dark and at different irradiation time, respectively.

CHAPTER 4

RESULTS AND DISCUSSION: PHOTOCATALYTIC ACTIVITY OF THE g-C_3N_4/TiO_2 HETEROJUNCTION COMPOSITES DERIVED BY THE HYDROTHERMAL PROCESS

4.1 General Remarks

In this part of the thesis the results of the hydrothermally derived g-C_3N_4/TiO_2 heterojunction composites were presented and discussed. Hydrothermal method was selected because of the controllable synthesis conditions, feasibility, and good crystallinity in the products. Six different composites with increasing weight percentage (wt%) of g-C_3N_4 from 20 to 90 wt% with 10% increments were prepared. In addition, the composite containing 80 wt% g-C_3N_4 was heat treated at calcination temperatures of 350, 400, 450, and 500 °C. After preparation, effect of the g-C_3N_4 content on g-C_3N_4/TiO_2 composites and the heat treatment temperatures on the microstructure developed were investigated by various characterization techniques. Finally, photocatalytic activity of g-C_3N_4/TiO_2 heterojunction composites were measured and compared with that of TiO_2 and g-C_3N_4 powders along with a commercially available TiO_2 powder. Moreover, the possible photocatalytic mechanism taking place in the g-C_3N_4/TiO_2 nanocomposites upon solar light illumination was outlined.

The g-C_3N_4/TiO_2 nanocomposites prepared were yellow in color. Depending on the g-C_3N_4 content they appeared in light yellow to dark yellow colors as indicated in Figure 3.1. As the g-C_3N_4 content decreases, the yellow color becomes lighter approaching the white color of pristine TiO_2 powder.

4.2 Characterization of the Powders

4.2.1 Particle Size Analysis

Hereafter, the g-C_3N_4 powder prepared will be referred to as pristine g-C_3N_4. The particle size distribution curve of pristine g-C_3N_4 powder is shown in Figure 4.1. The pristine g-C_3N_4 powder has trimodal distribution meaning that the particles are composed of fine, medium, and coarse size of particles. Fine, medium, and coarse particles have the average size of ~0.6, ~10.5, and ~200 μm, respectively. The particle size analysis suggests that size of the g-C_3N_4 particles ranges between 0.28 to 870 μm. The d_{10}, d_{50}, and d_{90} values are 6.2, 98.6, and 278.2 μm, respectively.

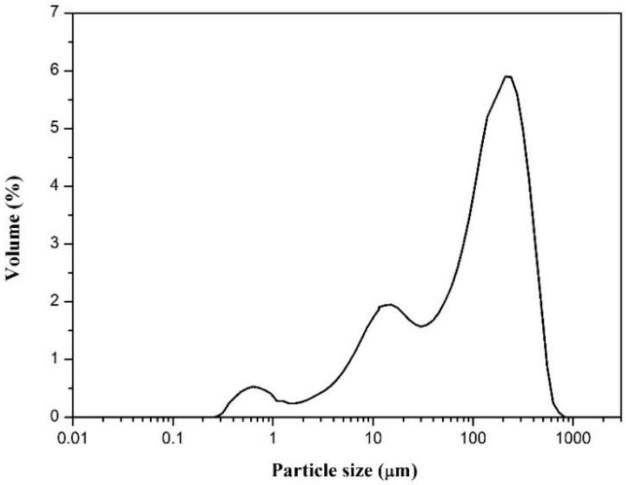

Figure 4.1. Particle size distribution curve of g-C_3N_4 powder.

The particle size distribution curve of the TiO_2 powder prepared, hereafter will be referred to as pristine TiO_2, is shown in Figure 4.2. The pristine TiO_2 powder shows bimodal distribution, meaning that the particles are composed of fine and coarse size of particles. Fine and coarse particles have the average size of ~0.7 and ~57.5 μm, respectively. The particle size analysis suggests that size of the particle's ranges between d_{10}= 3.6 μm and d_{90}=173.6 μm. The average size is 43.6 μm.

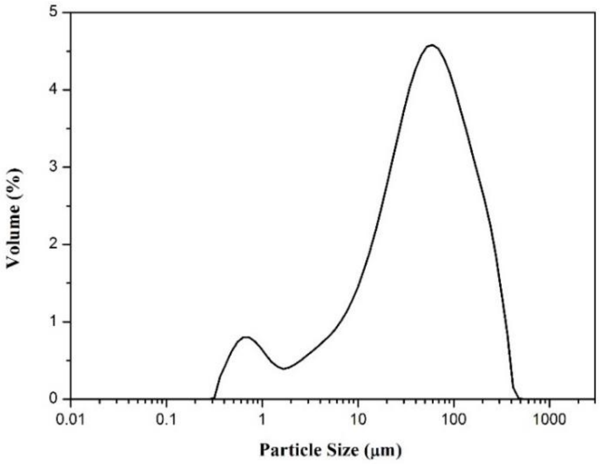

Figure 4.2. Particle size distribution curve of TiO_2 powders.

After this point, the g-C_3N_4/TiO_2 powders prepared will be referred to the codes presented in Table 3.1. The particle size distribution curve of the hydrothermally derived TCN-80 powder is shown in Figure 4.3. The particle size analysis recommends that TCN-80 powder has trimodal distribution. Fine, medium, and coarse particles have the average size of ~0.2, ~0.7, and ~6.4 μm, respectively. A 10% of the particles have sizes smaller than 0.1 μm whereas, a 90% of the particles have sizes smaller than 5.7 μm. Mean size of the particles is 0.2 μm, which is smaller than that of the pristine g-C_3N_4 and TiO_2 powders. Obviously, the hydrothermal treatment at 110 °C for 1 h decreased the particle size and narrowed the particle size distribution range of both pristine g-C_3N_4 and TiO_2 powders.

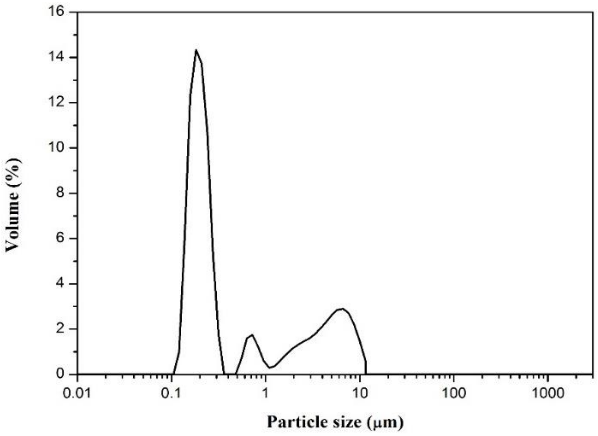

Figure 4.3. Particle size distribution curve of TCN-80 powder.

4.2.2 X-Ray Diffraction (XRD) Analysis

The XRD pattern of pristine g-C_3N_4 is shown in Figure 4.4. The diffraction peaks at 13.0° and 27.4° were attributed to characteristic peaks of (100) and (002) planes of g-C_3N_4 (JCPDS 01-087-1526). The diffraction peaks at 44.5° and 56.5° belong to (201) and (004) planes, respectively of hexagonal g-C_3N_4 (JCPDS 01-087-1526). Moreover, there is a small but visible peak at 17.75° belonging to (020) planes for the leftover carbon phase (JCPDS 01-073-5048). The data imply that pristine g-C_3N_4 is analytically pure.

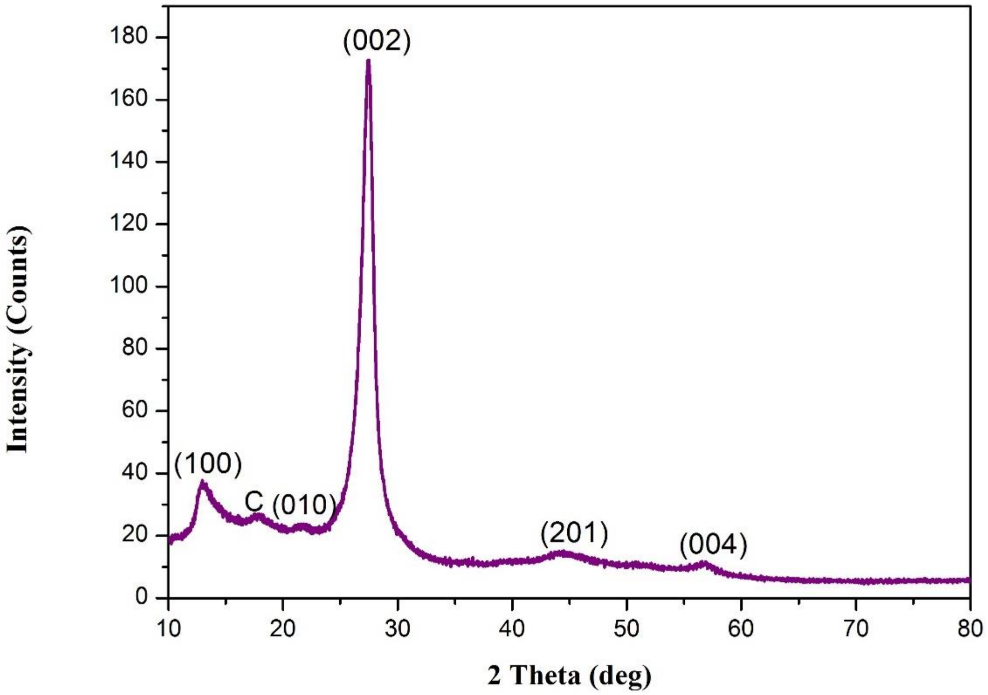

Figure 4.4. XRD pattern of pristine g-C_3N_4 powder.

The XRD pattern of the pristine TiO_2 powder derived by the hydrothermal process is shown in Figure 4.5. The diffraction peaks located at 25.4°, 37.6°, 48°, 54°, and 63° belong to (101), (004), (200), (105), and (204) planes of tetragonal anatase TiO_2 (JCPDS 00-021-1272), respectively. The diffraction peaks located at 25.4° and 30.8° are the characteristic peaks of (120) and (121) planes of brookite TiO_2 (JCPDS 00-029-1360). No diffraction peaks belonging to the other polymorph of TiO_2 (rutile) or other crystalline phases or contaminations were detected. The data imply that pristine TiO_2 is analytically pure. After this point, the peak angles presented in the text are for the 2θ angles.

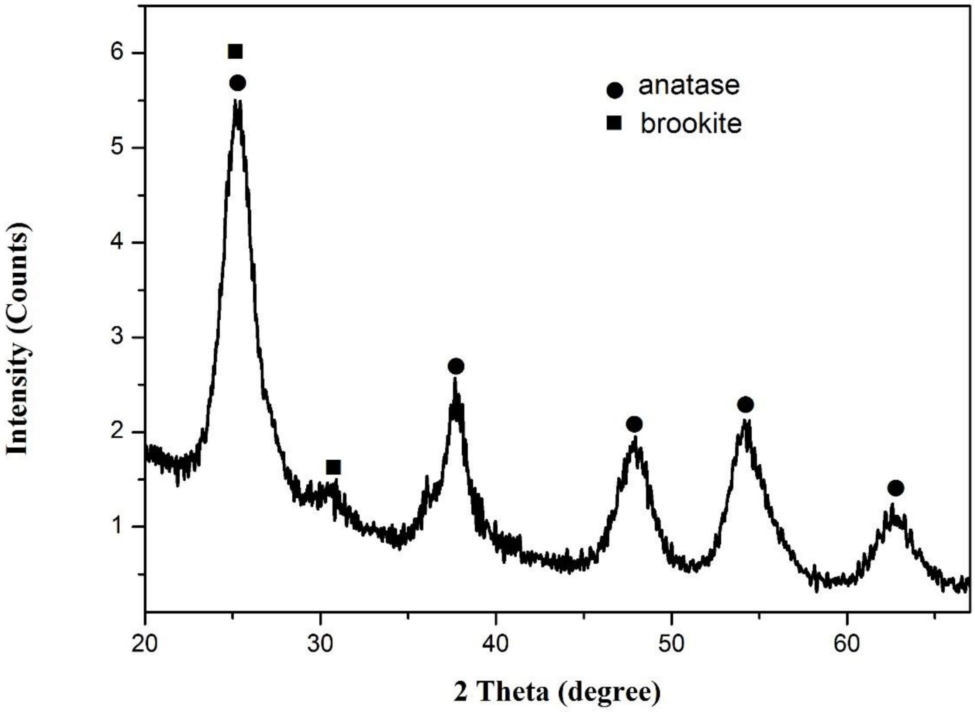

Figure 4.5. XRD pattern of pristine TiO_2.

The XRD patterns of the TCN powders are shown in Figure 4.6. The XRD patterns of the pristine TiO_2 and pristine g-C_3N_4 powders are included in Figure 4.6 for better understanding the peak positions in TCN composites. The XRD patterns of all TCN powders exhibit only main diffraction peaks belonging to only characteristic anatase TiO_2 and g-C_3N_4 crystallites. It is evident that hydrothermal synthesis hindered the development of brookite crystallites during hydrothermal reaction(s). Of course, another possibility is that the amount of brookite phase is very small so that it is below the detection limit of the diffractometer. Hence, XRD analysis may not be capable of detecting the brookite crystallites. Furthermore, because of the low synthesis temperature of 110 °C, there is no rutile phase in the prepared TCN powders.

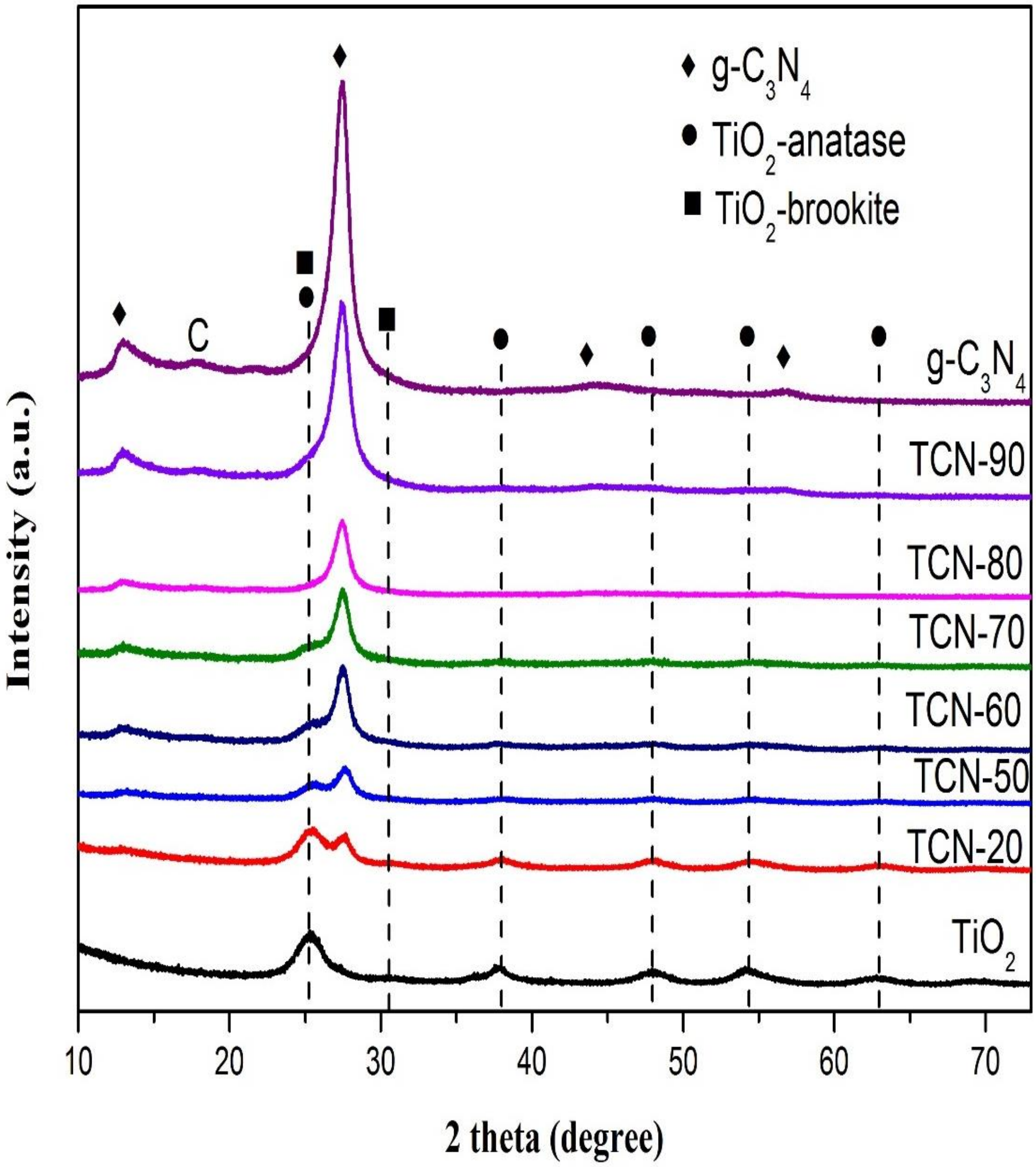

Figure 4.6. XRD patterns of the hydrothermally derived TCN powders together with pristine g-C_3N_4 and TiO_2 powders.

As seen in Figure 4.6, the intensity of the peak of g-C_3N_4 at 27.4° increased as the g-C_3N_4 content in the TCN powders increased without shifting the g-C_3N_4 peak position to higher or lower angles. The intensity of the main characteristic peak of the anatase TiO_2 at 25.4° belonging to 101 planes gradually decreased and eventually disappeared when the g-C_3N_4 content was 50 %. Anatase phase was not detected in the XRD patterns of the TCN powders containing more than 50 wt% of g-C_3N_4 because of the overlapping of the main characteristic peak of the anatase with the peak of g-C_3N_4. The XRD peaks belonging to the anatase and g-C_3N_4 phases are separated for TCN-20 and TCN-50 powders. Li et. al [82] published similar results. They reported that the intensity of peak at 27.6° belonging to g-C_3N_4 increases while main characteristic peak of TiO_2 at 25.2° decreases as g-C_3N_4 content in the g-C_3N_4/TiO_2 nanocomposite is increased.

Table 4.1 shows the crystallite sizes of the TCN powders together with pristine TiO_2 and pristine g-C_3N_4 powders. The crystallite sizes were calculated by using Debye-Scherrer formula. The anatase crystallites have size of 3.6 nm in pristine TiO_2. This value is almost the same as that 3.9 nm reported by Erdogan et al. [90] for TiO_2 containing only anatase phase. The crystallite size of pristine g-C_3N_4 is 5.01 nm. Svoboda et al. [91] published alike values. g-C_3N_4 powders prepared at different synthesis temperatures have variable crystalline sizes ranging between 4 and 6 nm. It was recognized that the data obtained by the XRD analysis do not agree with the data obtained by the particle size analysis as reported in Section 4.2.1. Because particle size and crystallite size are different from each other. Crystallite size is the smallest crystal in the powder form which is commonly calculated by using Debye-Scherrer formula. However, particle size reports a value for a single crystallite or for an agglomerate of several crystallites. Particle size cannot be smaller than crystallite size but, they may be the same in ultrafine particles [92]. This is an explanation of why the sizes reported in Section 4.2.1 are certainly bigger than the ones presented in Table 4.1. The size of anatase crystallites decreased with increasing g-C_3N_4 content in TCN powders. Because of the insufficient intensity of anatase peak at 25.4° in the XRD patterns of TCN-80 and TCN-90 powders, the anatase crystallite size for these powders could be calculated. The findings are in accord with the results published by Hao et al. [84] who reported that the composite formation provides a tendency to increase anatase TiO_2 phase.

There is no information in the literature related to the crystallite size of the g-C_3N_4 phase present in the g-C_3N_4/TiO_2 heterojunction composites. Some researchers calculated only average crystallite size in the composites [52,84,93] However, when compared to pristine g-C_3N_4 powder, crystallite size of the g-C_3N_4 phase present in TCN powders decreased with small additions of g-C_3N_4, i.e. until the g-C_3N_4 content reaches 60 wt%. When g-C_3N_4 content is more than TiO_2 content in the composites, size of the g-C_3N_4 crystallites present in TCN powders increased. Our fundemantal understanding to explain the flactuations in the size of the g-C_3N_4 crystallites in TCN powders is yet limited. Further investigation is needed to elucidate the reversal in the size of the g-C_3N_4 crystallites with increasing g-C_3N_4 content.

Table 4.1 Size of the crystallites present in the hydrothermally derived powders.

Powder name	Crystallite Size (nm)	
	Anatase	g-C_3N_4
TiO_2	3.60	-
TCN-20	3.57	4.17
TCN-50	3.12	4.91
TCN-60	3.11	5.55
TCN-70	2.80	5.98
TCN-80	-	6.13
TCN-90	-	5.14
g-C_3N_4	-	5.01

Figure 4.7 shows the XRD pattern of TCN-80 powder together with the XRD patterns taken after heat treating the same composite at various temperatures ranging from 350 to 500 °C. XRD analysis of the TCN powders was performed between at 10 and 70°. The main characteristic peaks belonging to the anatase-TiO_2 and g-C_3N_4 are detected in all TCN powders.

In TCN-80, the main characteristic anatase peak located at 25.4° was not detected due to the overlapping of the anatase and g-C_3N_4 peaks. When heat treatment temperature was increased, the intensity of this main anatase peak increased as seen in Figure 4.7. The anatase peak was distinguished by naked eye clearly especially in the patterns of TCN-80-450 and TCN-80-500 powders. Also, with increasing heat treatment temperature, the XRD peak belonging to the g-C_3N_4 phase weakened due to decomposition of g-C_3N_4. Dong et al. [18] stated that g-C_3N_4 decomposes fully at the temperatures up to 700 °C. In this study the decomposition of g-C_3N_4 started at lower temperatures, which inhibited overlapping of the peaks and reduced the intensity of g-C_3N_4 peak suggesting that the amount of g-C_3N_4 decreased. The reasons why the decomposition of g-C_3N_4 started at lower temperatures need further detailed investigations.

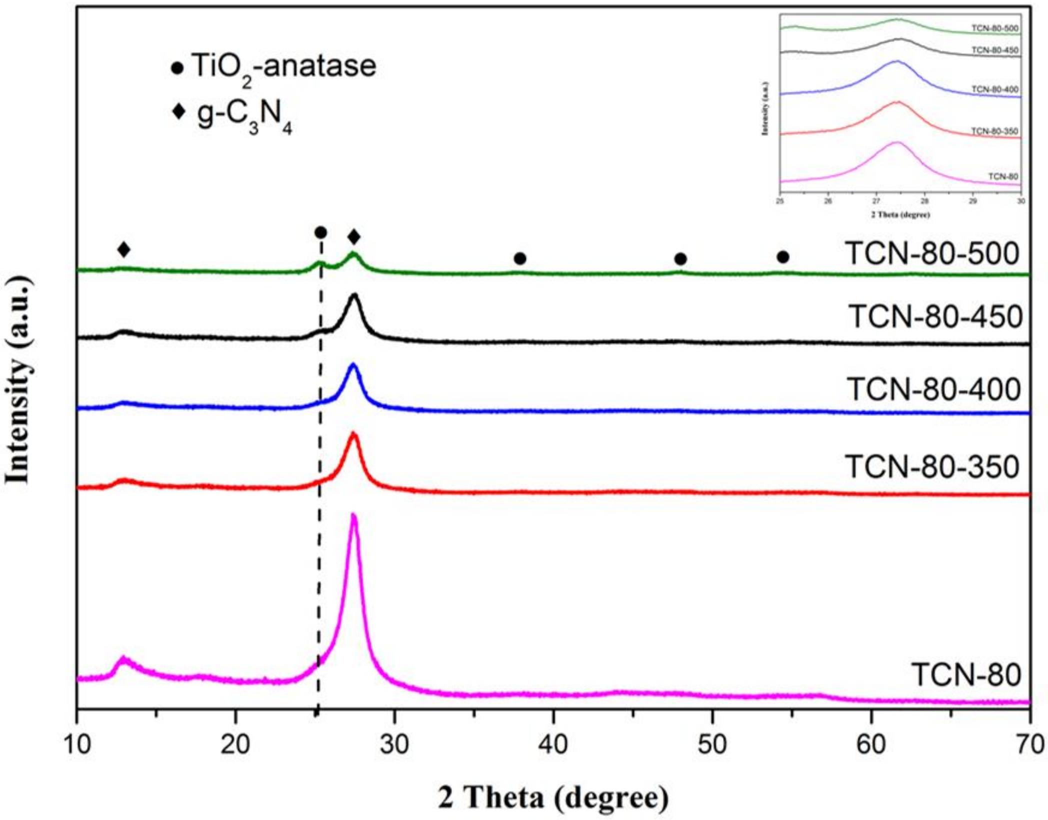

Figure 4.7. XRD patterns of TCN-80 powder before and after heat treatment at various temperatures.

The heat treatment also causes anatase to rutile transition in the temperature range between 600-700 °C [94]. However, in the TCN powders anatase crystallites transformed to rutile crystallites at lower temperatures. The XRD peak at 27.3° corresponding to (110) planes of the main characteristic peak of rutile phase of TiO_2 (JCPDS 00-021-1276) was detected in the pattern of TCN-80-500 powder but, it was not detected in all heat-treated TCN powders in the 25-30° range. Main characteristic peaks of rutile and g-C_3N_4 at 27.3° and 27.4°, respectively are very close to each other and mostly overlaps. Thus, concealment of rutile phase in some of the heat treated TCN powders may be due to the overlapping of the peaks. It is predicted that increasing heat treatment temperature increases the rutile phase. However, the intensity of the peak at 27.4° decreased with increasing temperature as shown in the inset in Figure 4.7. This finding verifies that there is no overlapping between the rutile and g-C_3N_4 particles. The peak present at 27.4° belongs only to g-C_3N_4 phase.

In order to find out whether rutile phase forms in pristine TiO_2 powder during heat treatment or not, pristine TiO_2 powder was heat treated at 400 °C. This powder was named TiO_2-400. Rutile phase was detected clearly in the XRD pattern of TiO_2 – 400 powder as shown in Figure 4.8. The XRD peaks at 27.3°, 36°, 41.3°, 54.4°, and 62.8° corresponds to (110), (101), (111), (211), and (002) planes of the rutile phase of TiO_2 (JCPDS 00-021-1276). The XRD pattern suggested that the powder also contains anatase and brookite phases of TiO_2.

Table 4.2 presents the crystallite sizes of phases developed in the heat-treated TCN-80 powders. The crystallite size of the anatase phase could not be calculated in the TCN-80 powders heat treated at 350, 400, and 450 °C because of the insufficient intensity of the anatase peak. It is recognized that crystallite size of anatase TiO_2 grows to 5.45 nm upon heat treatment of TCN-80 powder at 500 °C. However, there is a fluctuation in the size of g-C_3N_4 crystallites present in the heat-treated TCN-80 powders. The reason is unknown to us at the present time. Nonetheless, it is believed that the size fluctuation is related to the disintegration of g-C_3N_4 particles that decompose and shrink as the heat treatment temperature increases. It is for sure that increase in temperature causes a decrease in size of g-C_3N_4 crystallites. See Table 4.2. As mentioned earlier, there is no information reported in the open literature for the crystallite size of the g-C_3N_4 phase present in the g-C_3N_4/TiO_2 powders for comparison.

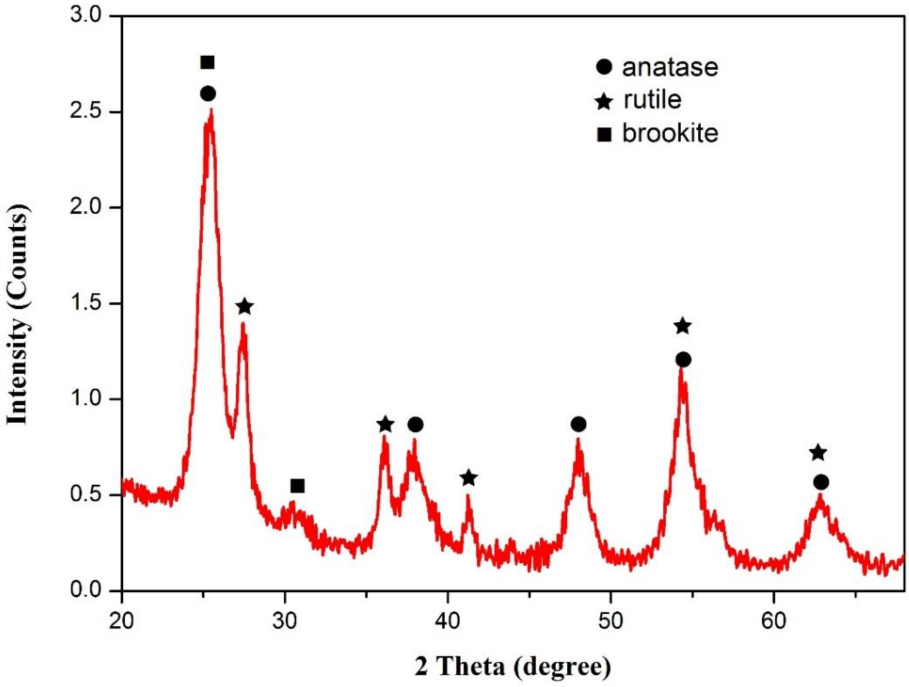

Figure 4.8. XRD pattern of TiO_2-400 powder.

Table 4.2 Crystallite sizes of heat-treated TCN-80 powders.

Powder name	Crystallite Size (nm)	
	Anatase	g-C_3N_4
TCN-80-350	-	5.14
TCN-80-400	-	5.04
TCN-80-450	-	4.98
TCN-80-500	5.45	4.73

4.2.3 Morphological and Elemental Analysis

Figure 4.9 shows the representative FESEM images taken from the surface of pristine g-C_3N_4 and pristine TiO_2 powders together with TCN powders. The effect of TiO_2 content on the morphology of TCN powders was examined in detail. The images for TCN powders were taken at 100000 magnifications. However, the magnification of the image of pristine g-C_3N_4 powder is 10000 though that of pristine TiO_2 powder is 250000. As seen in Figure 4.9 (a), pristine g-C_3N_4 particles consist of a lamellar structure with particles of various sizes ranging from 1 μm to 7 μm. The layers stacked with each other due to thermal polymerization. Also, surfaces of the layers are smooth and flat without irregularities. Size of pristine TiO_2 nanoparticles varies between 12 nm and 32 nm as demonstrated in Figure 4.9 (b). All TiO_2 nanoparticles seem in nearly spherical shape and their morphologies are almost uniform.

The FESEM examinations of TCN powders revealed that lamellar structure of pristine g-C_3N_4 remained in TCN powders but, its surface became rougher as the TiO_2 crystallites grew and attached on their surfaces and covered them as shown in Figure 4.9 (c)-(h). It is remarked that dosing of g-C_3N_4 provides the nucleation and growth of TiO_2 particles on the surfaces of g-C_3N_4 sheets [82]. Obviously, TiO_2 nanoparticles are denser and more uniform than g-C_3N_4 sheets. Because of low amount of TiO_2 in TCN-90, nearly spherical agglomerates of TiO_2 crystallites are shown in the edges of g-C_3N_4 sheets as seen in Figure 4.9 (c). These agglomerates related with the high surface energy of TiO_2 crystallites. Size of the particle's ranges between ~0.07 and 0.25 μm. With increasing TiO_2 content, the surface of TCN powders becomes rougher and the amount and the size of agglomerates increase as shown in Figures 4.9 (d)-(h). Figure 4.9 (f) shows that TiO_2 crystallites covered the g-C_3N_4 layer. Shape of the composite particles is more spherical when TiO_2 content reaches 50 wt% as seen in Figure 4.9 (g). When TiO_2 content was more than g-C_3N_4 content in the composites, more uniform morphology was observed since all g-C_3N_4 particles were covered by TiO_2 and there was excess amount of TiO_2 in the structure as displayed in Figure 4.9 (h). Additionally, the size of the particles decreased to nanoscale i.e., 20-80 nm. Among all TCN powders, TCN-20 probably had the smallest particles. Conclusively, the TiO_2 content is very effective for the development of the morphology in TCN powders.

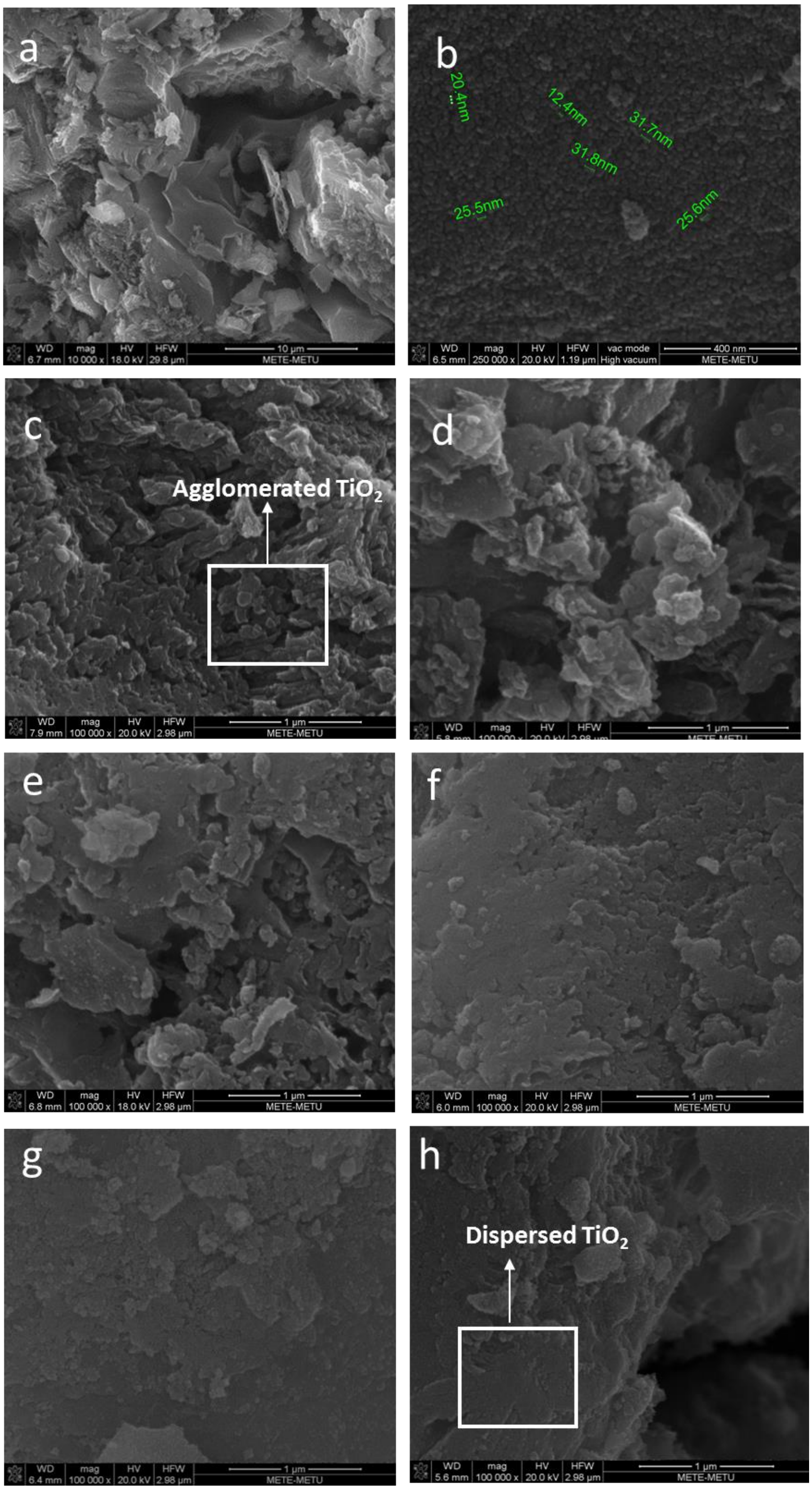

Figure 4.9. FESEM images of the powders a) g-C_3N_4, b) TiO_2, c) TCN-90, d) TCN-80, e) TCN-70, f) TCN-60, g) TCN-50, and h) TCN-20.

The EDS spectra of pristine g-C_3N_4, TCN-50, and pristine TiO_2 powders are depicted in Figure 4.10. Pristine g-C_3N_4 consisted of only C and N elements. Pristine TiO_2 composed of only Ti and O elements. Data agree very well with that obtained from XRD analysis implying that pristine g-C_3N_4 and pristine TiO_2 powders are analytically pure. TCN-50 powder contained the elements present in both pristine TiO_2 and pristine g-C_3N_4 namely; C, N, O, and Ti. The Au element in the spectra comes from sputter coating of the powders to obtain desired conductivity in FESEM analysis.

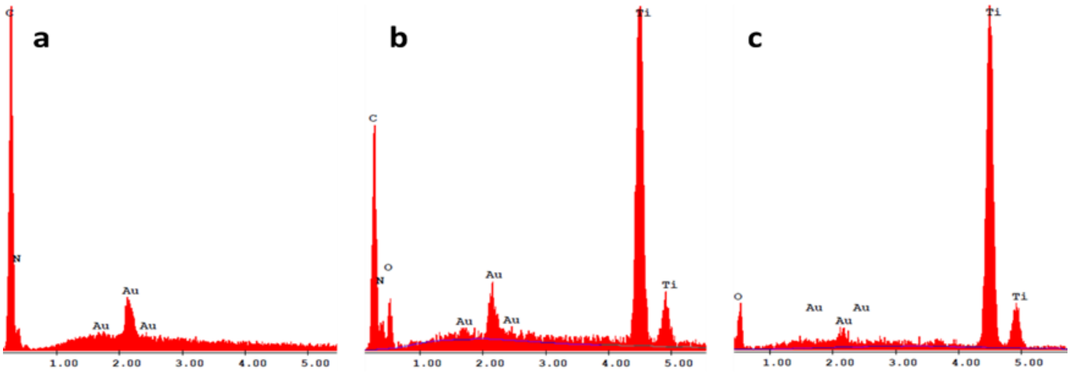

Figure 4.10. EDS spectra of powders a) pristine g-C_3N_4, b) TCN-50, and c) pristine TiO_2.

The EDS analysis data with respect to elemental composition of the powders are listed in Table 4.3 Chemical composition of the powders prepared.. The data reveal that stoichiometric compositions of TiO_2 and g-C_3N_4 were not obtained exactly in TCN powders but, they are very close to desired stoichiometric values. The elements (C, N, O, Ti) present in TCN powders also suggest that there is an interfacial joining between g-C_3N_4 and TiO_2 particles.

Table 4.3 Chemical composition of the powders prepared.

Powder	Composition (wt %)			
	C	**N**	**O**	**Ti**
TiO_2	0	0	36.35	63.65
TCN-20	8.58	4.38	26.95	60.09
TCN-50	36.41	11.87	15.32	36.40
TCN-60	38.42	15.00	30.55	16.03
TCN-70	39.29	17.42	29.88	13.41
TCN-80	48.25	29.75	3.60	18.40
TCN-90	56.24	40.02	1.06	2.67
g-C_3N_4	48.56	15.79	0	0

The representative FESEM images of the heat-treated TCN-80 powders are shown in Figure 4.11. It is obvious that, the heat-treated TCN-80 powders have similar microstructural features with untreated TCN-80 powder as shown in Figure 4.11 (a)-(c). Microstructure of the heat-treated powders consist of sheets. The shapes of the g-C_3N_4 sheets transformed to curly lamellar porous structure [95]. Upon heat treatment, the surface of the particles became rougher and TiO_2 nanoparticles attached on the g-C_3N_4 sheets. However, the sheets become thinner as compared to the sheets in TCN-80 powder when heat-treatment temperature is increased from 350 to 450 °C. The morphology of TCN-80-500 powder is quite different than the other the heat-treated TCN-80 powders as a result of the decomposition of g-C_3N_4. As explained in XRD and TGA studies, the content of g-C_3N_4 gradually decreased in terms of wt%. When temperature reaches the 500 °C, almost all the g-C_3N_4 disappeared. Table 4.4 tabulates the EDS data for the heat-treated TCN-80 powders. Data revealed that an increase in the heat-treatment temperature causes a decrease in the amount of g-C_3N_4 in the TCN-80 powders.

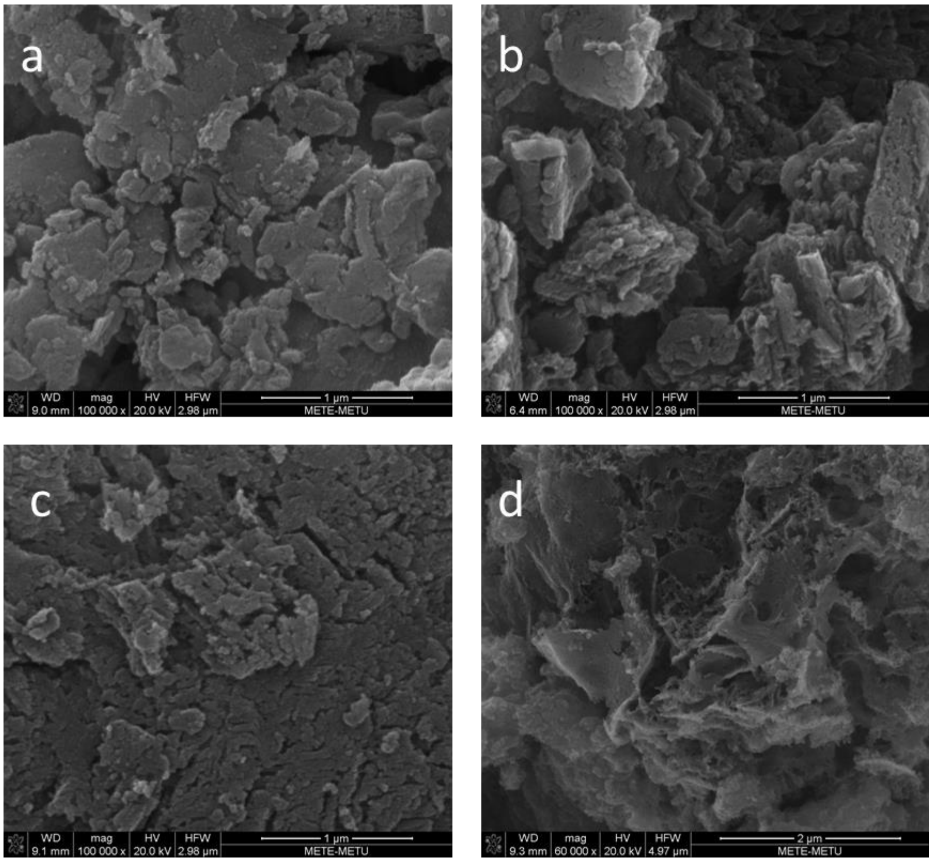

Figure 4.11. FESEM images of powders a) TCN-80-350, b) TCN-80-400, c) TCN-80-450, and d) TCN-80-500.

Table 4.4 Chemical composition of the heat-treated TCN-80 powder.

Powder	Composition (wt %)			
	C	**N**	**O**	**Ti**
TCN-80-350	44.62	31.54	3.47	20.38
TCN-80-400	41.06	27.50	5.39	26.05
TCN-80-450	44.92	19.77	4.08	31.22
TCN-80-500	38.45	17.7	13.57	30.38

4.2.4 Fourier Transform Infrared Spectroscopy (FT-IR) Analysis

The FT-IR transmission spectra of TCN powders along with those of pristine g-C_3N_4 and pristine TiO_2 powders are shown in Figure 4.12. For pristine TiO_2 powder, the absorption peaks at 400-700 cm^{-1} and at 1395 cm^{-1} are attributed to Ti-O and Ti-O-Ti stretching vibrations. The band at 1693 cm^{-1} shows O-H bending of physiosorbed water [96,97]. The broad band at 3142 cm^{-1} corresponds to hydroxyl group or the absorbed water molecules [40]. In the spectra, the 1232 - 1620 cm^{-1} range dominates for g-C_3N_4 peak. The bands at 1534 cm^{-1} and 1620 cm^{-1} for pristine g-C_3N_4 powder are related to C=N stretching. The 1317 cm^{-1}, 1393 cm^{-1}, and 1534 cm^{-1} bands correspond to rotating vibration of C-N heterocycles. s-triazine ring vibrations are represented by 806 cm^{-1} band. When the spectra of TCN powders are compared with that of pristine TiO_2 and g-C_3N_4, they possess the main characteristic spectrum of g-C_3N_4 along with TiO_2 absorption peaks. The intensity of the bands of TiO_2 at 400-700 cm^{-1} decreases as g-C_3N_4 content in TCN powders increases. Also, the absorption peaks at a range between 1232 and 1620 cm^{-1} have 6 cm^{-1} redshifts (movement of the adsorption edge to higher wavelengths).

The results reveal that there is an interfacial construction between g-C_3N_4 and TiO_2, implying composite formation. Similar results have been published by several researchers [39,98]. New bond of g-C_3N_4/TiO_2 interface lead to a decline for long range ordered arrangement of ultrathin g-C_3N_4 layer and the conjugation network structure is also slightly reduced [38].

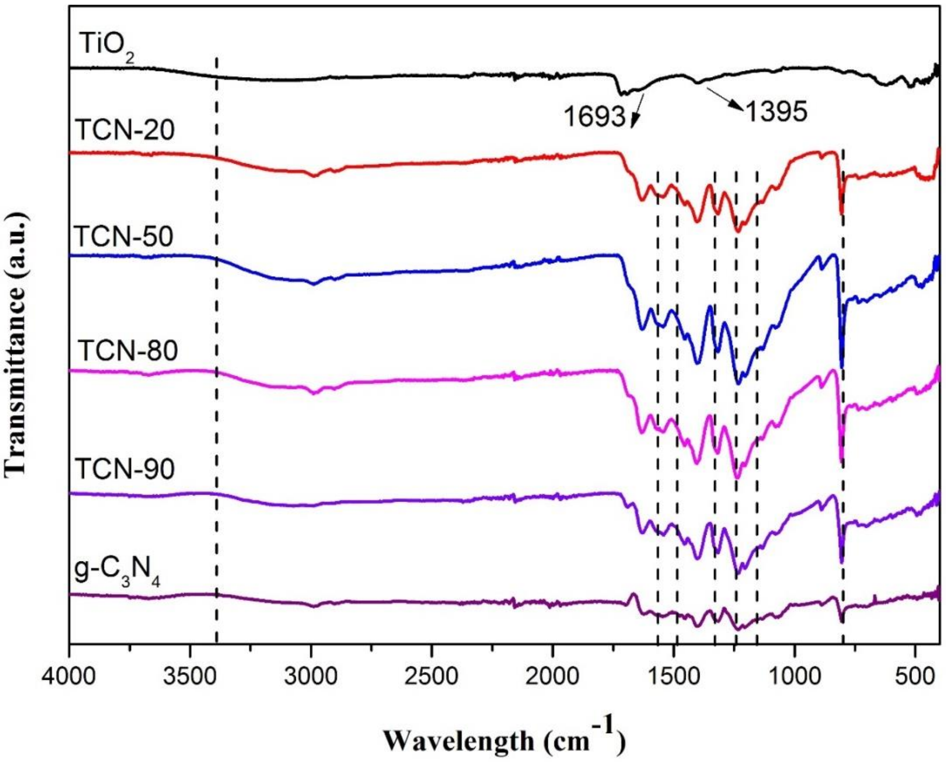

Figure 4.12. The FT-IR transmission spectra of pristine g-C_3N_4, pristine TiO_2, and TCN powders.

Figure 4.13 presents the FT-IR transmission spectra of TCN-80 powder and the heat-treated TCN-80 powders. The spectra of pristine g-C_3N_4 and pristine TiO_2 powders are included in the figure for comparison purpose. The spectra of TCN-80 and the heat-treated TCN-80 powders possess the characteristic absorption peaks of both TiO_2 and g-C_3N_4, Compared to pristine powders, the characteristic bands of the heat-treated TCN-80 powders redshifted. Redshift is another similarity between the spectra of TCN-80 and the heat-treated TCN-80 powders. Redshift is related with the interaction between TiO_2 and g-C_3N_4 particles, which prevents recombination of photogenerated electrons and holes. It enhances the photocatalytic activity for the composites, which will be discussed later in Section 4.2.7.

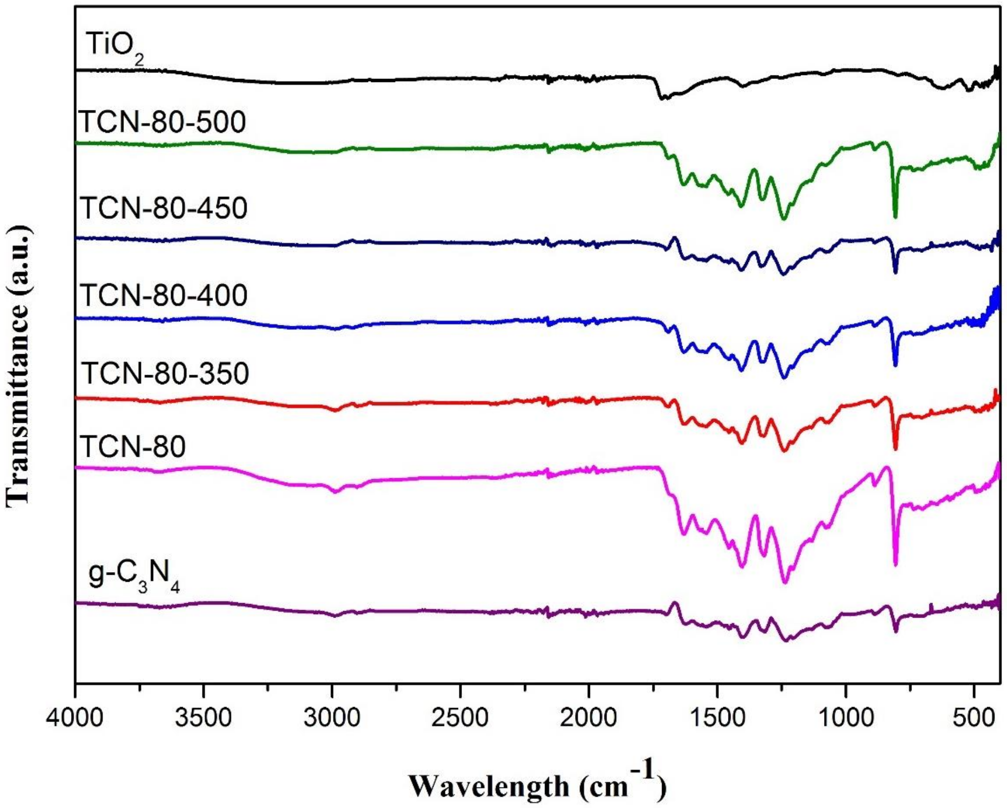

Figure 4.13. FT-IR transmission spectra of TCN-80 and the heat-treated TCN-80 powders together with pristine TiO_2 and g-C_3N_4 powders.

4.2.5 Raman Analysis

Raman spectra of TCN-80 and TCN-80-400 powders are shown in Figure 4.14. The spectra of both powders include the typical peaks of g-C_3N_4 at 707 cm^{-1} and 1232 cm^{-1} for TCN-80 powder and at 706 cm^{-1} and 1235 cm^{-1} for TCN-80-400 powder. Raman shift at 706 or 707 cm^{-1} originated from the s-triazine ring in pristine g-C_3N_4 powder. Also, the peak at 1232 or 1235 cm^{-1} arises from the stretching vibration modes of C-N and C=N cycles [43]. The main anatase peak which is located at 143 and 145 cm^{-1} is seen in the spectra of both TCN-80 and TCN-80-400 powders, respectively. Large degree of g-C_3N_4 Raman shifts provides a development of new bond alterations at the interface. The interface between g-C_3N_4 and the TiO_2 proves that g-C_3N_4/TiO_2 composite was achieved. Therefore, TCN powders and the heat-treated TCN-80 powders henceforward will be called TCN composites and the heat-treated TCN-80 composites, respectively.

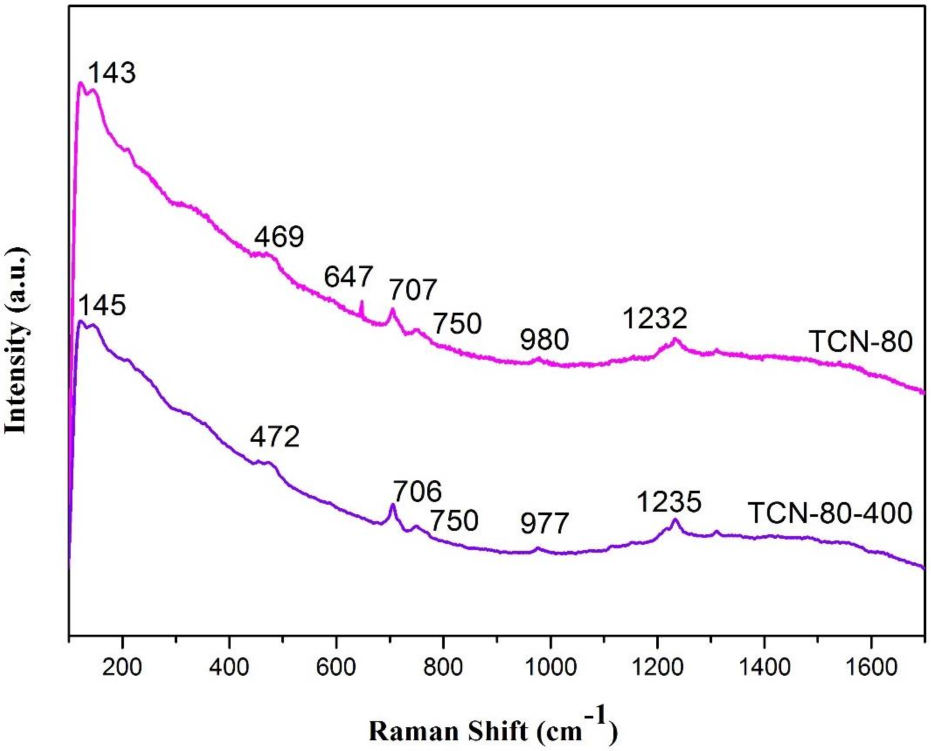

Figure 4.14. Raman spectra of TCN-80 and TCN-80-400 composites.

4.2.6 Diffuse Reflectance Spectra (DRS) Analysis

Figure 4.15 (a) shows absorption thresholds of pristine g-C_3N_4 and pristine TiO_2 powders together with TCN composites. The calculated absorption edge and band gap (E_g) values of the powders prepared are tabulated in Table 4.5. Data revealed that TiO_2 has the absorption edge in the UV-range at 439 nm. However, the absorption edge of g-C_3N_4 is 486.04 nm that involves in both UV and visible regions in solar spectrum. The TCN composites have absorption edge values in between the values of TiO_2 and g-C_3N_4. Also, the TCN composites had redshift to 439 nm. The data suggest that with composite formation, TiO_2 gained considerable extension in visible light region. When compared to pristine TiO_2, TCN composites have higher absorption intensity. The optical absorption intensity increases with increasing $g\text{-}C_3N_4$ content up to 80 wt%. The absorbance percent versus wavelength graphics shown in Figure 4.15 (a) was transformed to $(\alpha h v)^2$ versus hv plots as indicated in Figure 4.15 (b) by using Eq. 3.2. Both pristine $g\text{-}C_3N_4$ and TiO_2 have direct band gap. Therefore, the n value was taken as 1 [88]. It is obvious that all TCN composites have an Eg value in between the values of $g\text{-}C_3N_4$ and TiO_2.

Table 4.5 Absorbance edge and the band gap values of the powders prepared.

Powder	Absorbance edge (nm)	Eg (eV)
TiO_2	439.00	3.08
TCN-20	462.40	2.80
TCN-50	469.98	2.79
TCN-60	470.58	2.77
TCN-70	473.16	2.75
TCN-80	461.12	2.80
TCN-90	466.19	2.78
TCN-80-350	~461	2.80
TCN-80-400	~461	2.80
TCN-80-450	~461	2.80
TCN-80-500	~461	2.80
$g\text{-}C_3N_4$	486.04	2.70

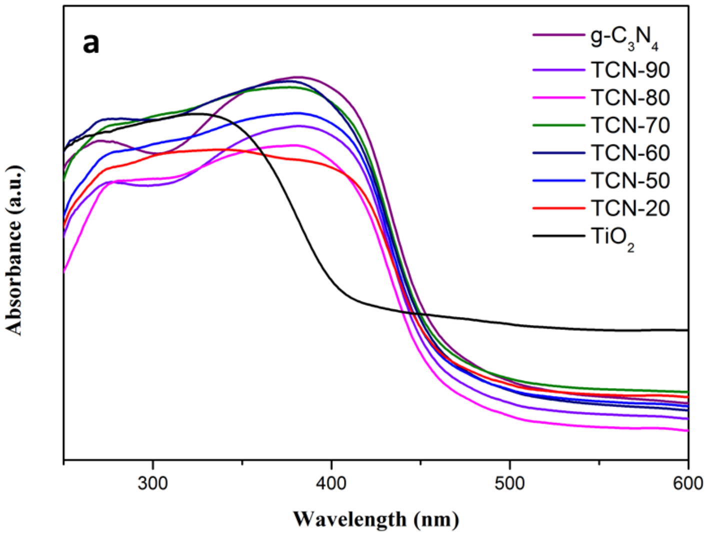

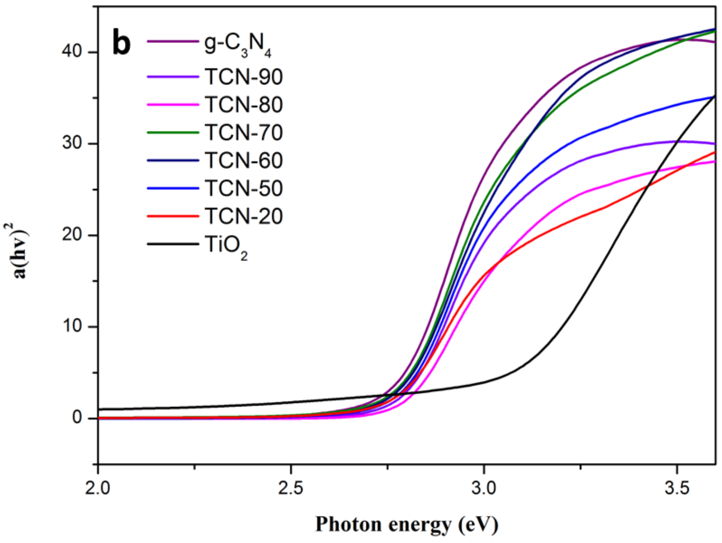

Figure 4.15. a) UV-vis diffuse reflectance spectra and b) $(\alpha hv)^2$ vs hv plots of the powders prepared.

The Eg values of the powders were calculated by the intersection point between linear part of the related line and x-axis of the graph as shown in Figure 4.16. Pristine TiO_2 has the lowest absorbance edge value. Thus, it has the largest Eg value of 3.08 eV among all the powders prepared. This calculated Eg value is the same as the value reported by Li et al. [83]. The calculated Eg value for pristine TiO_2 is lower than the value for anatase TiO_2 (3.2 eV) since it contains not only anatase but also brookite phase that has lower Eg (2.96 eV) than anatase [12]. Data revealed that the existence of even small amount of brookite phase in pristine TiO_2 powder affects the Eg value of TiO_2. g-C_3N_4 has the lowest Eg value of 2.70 eV that match up with the value given by Li et al. [29]. As expected, the Eg values of TCN composites decreased from 2.80 eV to 2.75 eV with increasing g-C_3N_4 content in TCN composites up to 70 wt% g-C_3N_4 additions since g-C_3N_4 has lower Eg value than TiO_2.

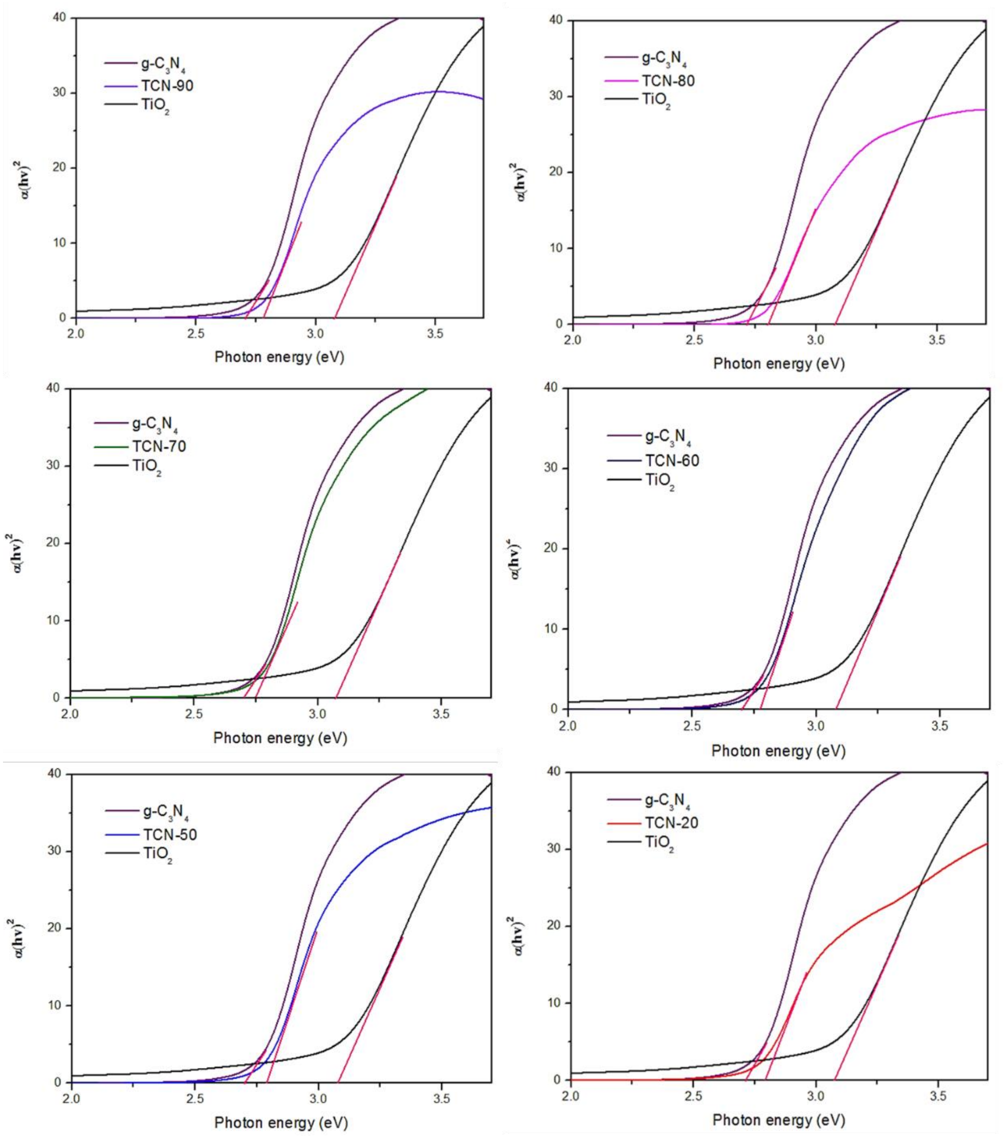

Figure 4.16. Band gaps of TCN composites as compared to pristine TiO_2 and g-C_3N_4 powders.

Although TCN-80 and TCN-90 composites contained more g-C_3N_4 than the other TCN composites, they exhibited the lower Eg values of ~2.80 and ~2.78 eV, respectively than TCN-70 composite that has Eg value of 2.75 eV. The reason(s) for the inconsistencies in Eg values are beyond our knowledge. However, the inconsistencies between the Eg values are small and within the experimental error limits. The absorbance spectra and the Eg values for the heat-treated TCN-80 composites are depicted in Figure 4.17 (a) and (b). Heat treatment did not have a significant effect on the absorbance edge and the Eg values of TCN-80 composite.

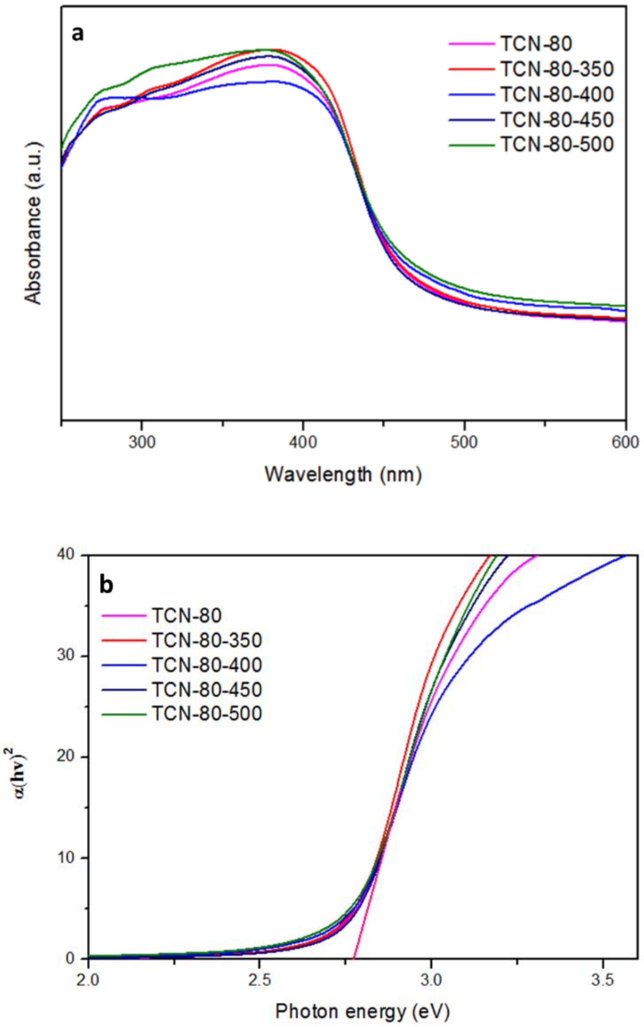

Figure 4.17. a) UV-vis diffuse reflectance spectra and b) band gap of the heat-treated TCN-80 composites.

The Eg configuration and the Eg values of the TCN composites are related with the incident photons, the photoexcitation of the electrons and holes, the transfer charge carriers, and the redox abilities of the electron hole pairs. For this reason, photocatalytic activity of the powder is directly affected by their Eg energies [87,99].

4.2.7 Photocatalytic Activity

Several researchers [7, 100] reported that the absorption-desorption equilibrium for TiO_2 at dark is reached in 30 min. Nonetheless, there is no information in literature reporting the absorption-desorption equilibrium time for TCN composites at dark. The MB degradation tests were performed to find out the absorption-desorption equilibrium time for TCN composites in accord with the procedure as described previously. The measurements were taken in very 5 min at dark for TCN-50 and TCN-80 composites. Results were plotted in Figure 4.18. The last 3 determinations for both composites were almost the same at 30 min and at 60 min.

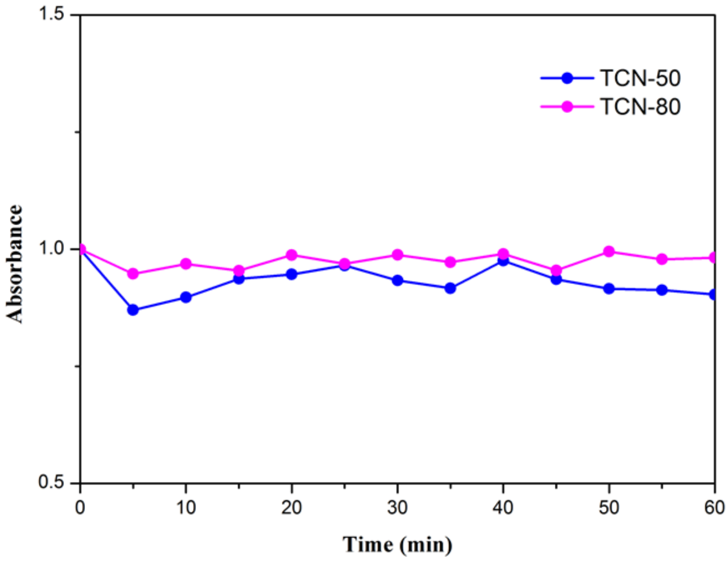

Figure 4.18. Absorption-desorption equilibrium plots for TCN-50 and TCN-80 composites.

It is believed that the absorption-desorption equilibrium was maintained at 30 min. Therefore, holding 30 min at dark was taken as the absorption-desorption equilibrium time for TCN composites and the MB suspensions prepared from TCN composites were kept at dark for 30 min for the photocatalytic activity tests. The photocatalytic activity graphs of pristine g-C_3N_4 and pristine TiO_2 powders together with TCN composites are shown in Figure 4.19. The absorbance and degradation values as calculated under solar light illumination for 180 min are given in Table 4.6. Results revealed that pristine TiO_2 nanoparticles has only 68.8% MB degradation of under 180 min solar light illumination although it had higher absorption (56.9%) at dark in 30 min. The achievement of only small amount of MB degradation is by reason of the wavelength of solar light is not enough for degradation. Pristine g-C_3N_4 particles exhibit lower absorption value (11.6%) than pristine TiO_2. However, it has degradation value of 45.5% under solar light because of its lower Eg (2.7 eV).

Table 4.6 MB degradation values of the powders after solar light illumination.

Powder	Absorbance (%) (at dark)	MB Degradation (%) (under solar light illumination)		
	30 min	**1 h**	**2 h**	**3 h**
TiO_2	56.9	60.5	62.4	68.8
TCN-20	11.2	15.1	40.5	54.1
TCN-50	27.3	35.7	51.2	70.7
TCN-60	50.0	66.4	72.2	75.6
TCN-70	19.6	46.9	61.8	77.1
TCN-80	27.4	44.1	61.2	79.7
TCN-90	28.9	40.3	54.4	67.9
TCN-80-350	64.0	73.5	79.2	85.1
TCN-80-400	68.2	86.4	95.3	100
TCN-80-450	54.2	69.6	83.4	89.4
TCN-80-500	59.4	61.2	70.9	84.7
g-C_3N_4	11.6	29.4	39.3	45.5
P25	37.8	49.7	71.5	80.6
MB	1.2	2.7	3.5	5.2

All TCN composites have absorption ability as realized from the decrease in MB concentration at the dark region, and MB degradation ability as understood from the decrease in MB concentration in the UV exposed region in Figure 4.19 (a). It was noticed that the absorbance values for the powders at dark positively affect the amount of MB degradation.

Figure 4.19 (b) demonstrates the variation of absorbance spectra of TCN-80 composite in the MB solution with wavelength. The intensity of absorption peak which has been 664 nm, was decreased gradually with increasing time. TCN-80 composite degraded almost all the MB under 360 min solar light illumination. When the MB degradation values under solar light illumination for 180 min considered, TCN-80 composite exhibited the highest photocatalytic activity among all TCN composites as shown in Figure 4.19 (a). It degraded 79.7% of MB. Except TCN-20 composite, all TCN composites had better MB degradation ability than pristine TiO_2 powder. TCN-20 composite degraded only 54.1% of MB. TCN-80 composite exhibited almost the same photocatalytic activity with P25 powder. See Table 4.6.

When g-C_3N_4 content in TCN composite exceeds 80 wt%, photocatalytic activity decreases. The MB degradation of TCN-90 composite decreased to 67.9%, remarkably. The reason can be, g-C_3N_4 create more surface to coat by the TiO_2 nanoparticles. But, amount of TiO_2 nanoparticles is not enough to cover the surfaces of all g-C_3N_4 sheets. The low amount of TiO_2 coating limits the active sites of the composites. Therefore, transfer of photoinduced carriers and photocatalytic activity decrease [82].

The results reveal that the TiO_2 provides excellent heterojunction effect in TCN composites. The heterojunction effect contributes to the transfer of charge carriers. Therefore, TiO_2 loading enhance photocatalytic activities of the TCN composites [101]. Decreasing crystallite size of the anatase phase in the composites is also accountable for the enhancement in photocatalytic activity.

The variation of photocatalytic MB degradation efficiency of TCN-80 composite and heat-treated TCN-80 composites with solar light illumination time are shown in Figure 4.19 (c). Application of a regulated heat-treatment positively affected the photocatalytic activity of TCN-80 composite. Increasing heat-treatment temperature led to an increase in photocatalytic activity up to 450 °C. One of the reasons for the increase is related to the crystallite size of g-C_3N_4 in the composites. Photocatalytic activity of the TCN composites increased with decreasing crystallite size of g-C_3N_4. With increasing heat-treatment temperature composite structure began to decompose. See Figure 4.11 (d). Especially for TCN-80-500 composite, amount of g-C_3N_4 decreased. This is the reason why photocatalytic activity decreases after temperature exceeds to 400 °C. Figure 4.11 (d) was drawn to compare the solar light photocatalytic activity of TCN-80-400 composite with control groups. That is, pristine TiO_2 powder, g-C_3N_4 powder, P25 powder, and MB without any photocatalyst addition (blank). TCN-80-400 composite has the highest photocatalytic activity for the degradation of MB among all TCN composites prepared and controls groups. See Figure 4.11 (c) and (d). TCN-80-400 composite degraded all of MB when exposed to solar light illumination for 180 min. The photocatalytic efficiency of TCN-80-400 composite is 1.5 times higher than pristine TiO_2 powder and 2.2 times higher than pristine TiO_2.

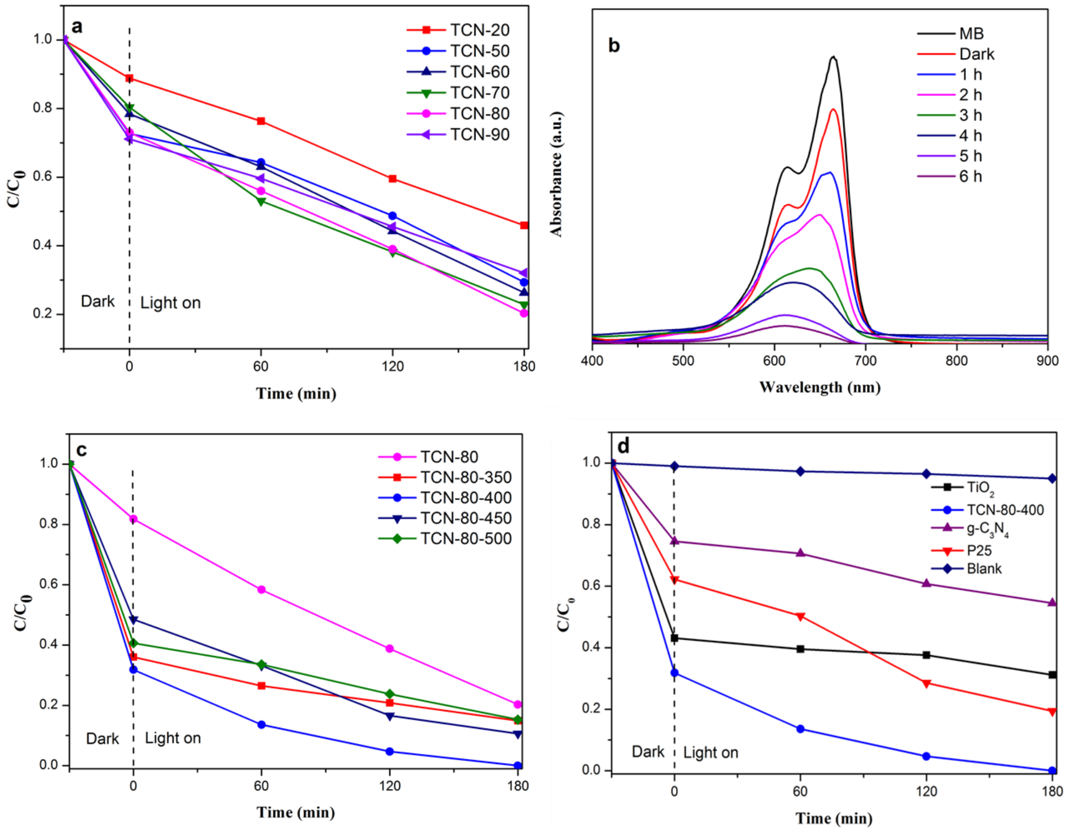

Figure 4.19. a) Solar light photocatalytic efficiencies of TCN composites, b) Absorbance of TCN-80 composite, c) Solar light photocatalytic efficiencies of TCN-80 composite and heat-treated TCN-80 composites, d) Solar light photocatalytic efficiencies of TCN-80-400 composite together with control groups.

The enhancement in the photocatalytic efficiency of TCN-80-400 composite is due to optimum band gap value which provides an extension of longer wavelength. Another reason for improving photocatalytic activity is an effective decrease of the

e^-/h^+ recombination rate. Li et al [82] reported similar results who stated that composites exhibit 80 wt% g-C_3N_4 with 500 °C heat treatment shows the best photocatalytic activity thanks to its smaller grain size and low band gap value.

4.3 Photocatalytic Mechanism

The photocatalysis mechanism proposed for the g-C_3N_4/TiO_2 heterojunction composites is schematically demonstrated in Figure 4.20 where the separation of e^-/h^+ pairs and their transportation are also shown. The VB and CB edge potentials of g-C_3N_4 were calculated by means of the Eqs.3.3 and 3.4 are 1.58 and -1.12 eV, respectively. The estimated VB and CB edge potentials of TiO_2 were 2.85 and -0.23 eV, respectively.

When g-C_3N_4 was exposed to the solar light (UV-vis), it absorbs the light and excites to produce photoinduced electrons as shown in Figure 4.20. First, electrons are transferred from its VB to CB. Then, since the CB edge potential of g-C_3N_4 (-1.14 eV) is more negative than that of TiO_2 (-0.225 eV), photoinduced electrons on the CB of g-C_3N_4 easily transfer to the CB of TiO_2 because of the well-built heterojunction structure [75]. Meantime, TiO_2 absorbs the UV light and excited for producing photoinduced electrons. These photoinduced electrons transfer from its VB to CB. The VB edge potential value of TiO_2 (2.85 eV) is more positive than g-C_3N_4 (1.58 eV). It provides easy transfer of photoinduced holes from TiO_2 to g-C_3N_4 due to heterojunction construction. As a result of this transfer, separation period of e^-/h^+ pairs increases [87]. Tthus the photocatalytic activity of the composites to the degradation of MB increases due to the transfer of interfacial charge-reactions [98].

First, to produce $\bullet O_2^-$, oxygen dissolves the collected electrons in the CB of TiO_2. These reactions contributed to produce active •OH radicals. Finally, produced •HO radicals react with the MB molecules. Then, CO_2 and H_2O are the final products. The redox reactions believed to take place are given in Section 2.1.1.1.

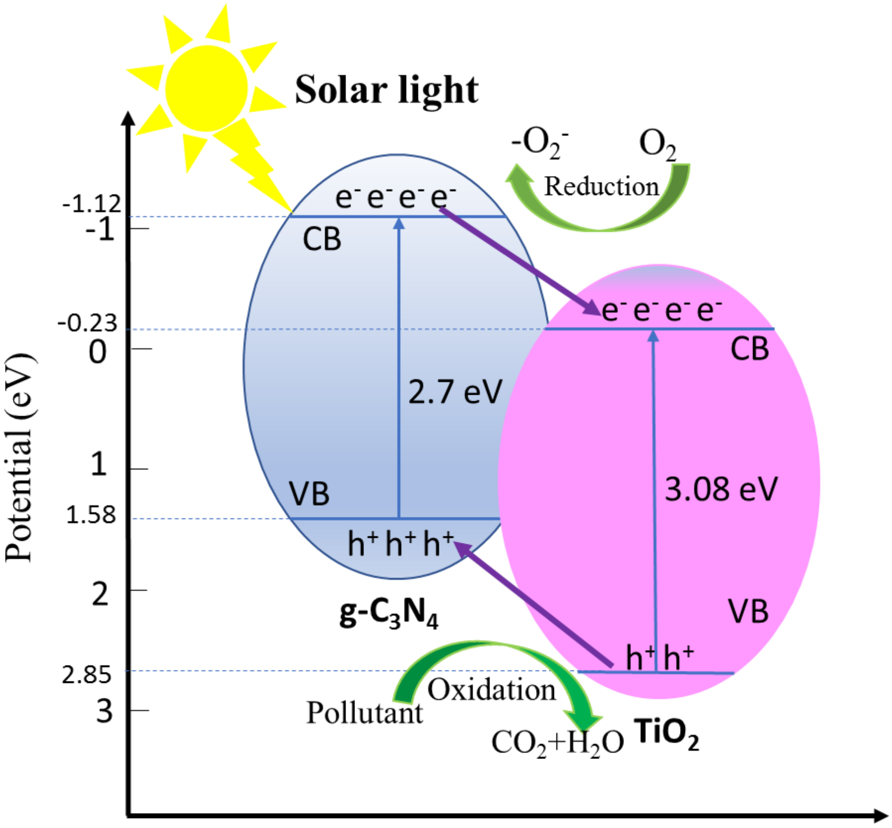

Figure 4.20. Schematic representation of the photocatalysis mechanism of g-C_3N_4/TiO_2 heterojunction composite.

CHAPTER 5

RESULTS AND DISCUSSION: PHOTOCATALYTIC ACTIVITY OF THE g-C_3N_4/TiO_2 HETEROJUNCTION COMPOSITES DERIVED BY THE SOL-GEL PROCESS

5.1 General Remarks

In this part of the thesis, the results of the sol-gel derived g-C_3N_4/TiO_2 heterojunction powders, hereafter will be named STCN powders, were presented and discussed. Three different composites with increasing g-C_3N_4 contents of 20, 50, and 80 wt% were synthesized along with pristine TiO_2. The powders were heat treated at 400 °C. After preparation, only the effect of the g-C_3N_4 content in the g-C_3N_4/TiO_2 nanocomposites on the photocatalytic efficiency was investigated. Results were compared with that of the pristine TiO_2 powders as well as a commercially available TiO_2 powder.

Similar to hydrothermally synthesized powders, the g-C_3N_4/TiO_2 nanocomposites derived by the sol-gel process were yellow in color as previously presented in Figure 3.3. Depending on the g-C_3N_4 content, they appeared in light yellow to dark yellow colors. The yellow color becomes lighter approaching the white color of pristine TiO_2 powder with decreasing g-C_3N_4 content.

5.2 Characterization of the Powder Synthesized

5.2.1 Particle Size Analysis

Particle size distribution curve of the sol-gel derived TiO_2 powder, hereafter will be called as $STiO_2$ powder, is shown in Figure 5.1. $STiO_2$ particles have bimodal distribution consisting of coarse and fine particles. The mean average size of fine particles are 0.54 µm and that of coarse particles are 23.6 µm. The particle size distribution of particles ranges between d(0.1)= 0.953 µm and d(0.9)=39.43 µm. The avarage particle size of all powders is 14.24 µm. When a comparision is made, $STiO_2$ powder consists of particles smaller than the hydrothermally synthesized pristine TiO_2 powders. See Figure 4.2. It is assumed that the calcination of $STiO_2$ powders at 400 °C reduces the particle size.

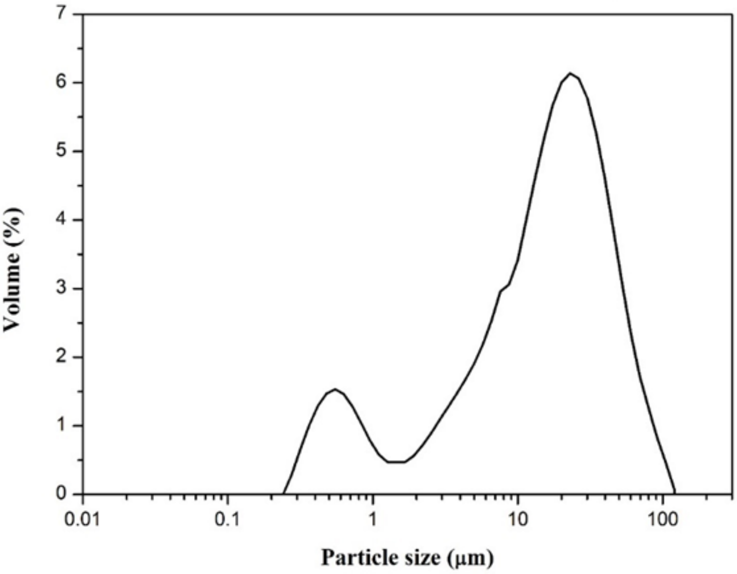

Figure 5.1. Particle size distribution curve of the $STiO_2$ powders.

The STCN powders will be referred to the codes given in Table 3.1. The particle size distribution curve of STCN-50 powder is demonstrated in Figure 5.2. The particle size analysis of this powder reveal that particles range between 0.3 µm and 200 µm. The avarage particle size of the particles is 18.11 µm. Similar to $STiO_2$ powder, it has bimodal distribution. Fine and coarse particles have average of 0.6 µm and 2.4 µm sizes, respectively. 10% of the particles is smaller than 3.2 µm while 90% of the particles is smaller than 48.8 µm. It is clear that STCN-50 powder has smaller particles than both constituents. That is, pristine g-C_3N_4 (Figure 4.1) and $STiO_2$.

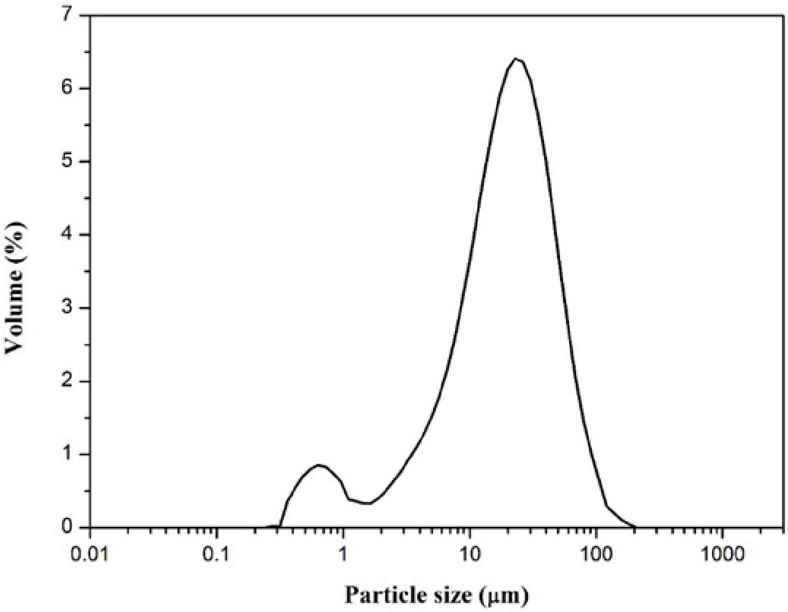

Figure 5.2. Particle size distribution curve of the STCN-50 powders.

5.2.2 X-Ray Diffraction (XRD) Analysis

XRD pattern of $STiO_2$ powder is demonstrated in Figure 5.3. The diffraction peaks located at 25.4°, 37.8°, 48°, 54°, 55°, 63°, and 69° corresponds to (101), (004), (200), (105), (211), and (204) of tetragonal anatase TiO_2 (JCPDS 00-021-1272), respectively. Additionally, main characteristics peak of brookite TiO_2 diffracting from (121) is situated at 30.8° (JCPDS 00-029-1360). There is an overlapping between brookite (120) and anatase (101) peaks at 25.4°. Similar results were reported previously by other researchers [15, 102].

As stated previously in Section 4.2.2, heat treatment leads to transformation of anatase to rutile or brookite to rutile. However, $STiO_2$ powder was consisted of only anatase phase even after the heat treatment at 400 °C. Rutile and contaminations were not observed. Brookite peak located 30.8° in $STiO_2$ powder, more visible than that present in pristine TiO_2, can be originated from long synthesizing durations of the sol-gel derived powders. Paola et al. [51] stated that brookite can be synthesized generally at low temperatures (110-220 °C) and for long synthesis times (24-48 h).

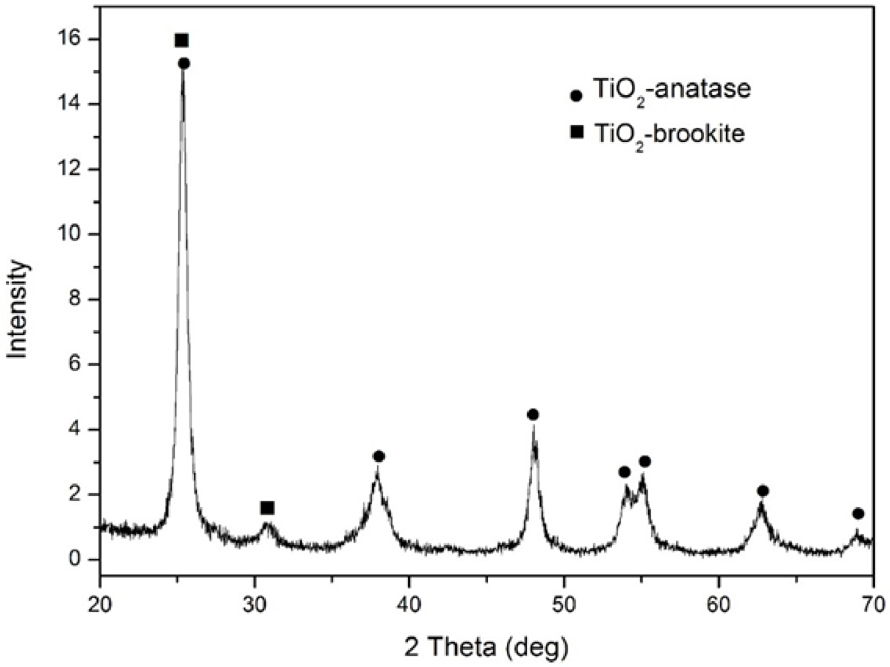

Figure 5.3. XRD pattern of $STiO_2$ powders.

Phases present in the STCN powders were identified by XRD analysis. Figure 5.4 shows the XRD patterns of the STCN powders together with g-C_3N_4 powder and $STiO_2$ powder. Except $STiO_2$ powder, all powders have diffraction peaks at 13.0° and 27.4° corresponding to (100) and (002) of g-C_3N_4 (JCPDS 01-087-1526) [83]. There is a graphitic like structure [33]. No other peak belonging to g-C_3N_4 was observed in the XRD of the STCN powders. Moreover, all of the STCN powders possessed the phases present in $STiO_2$ at almost the same peak positions of the phases. Tetragonal anatase peaks located at 25.4°, 37.8°, 48°, 54°, 55°, 63°, and 69°, corresponding to (101), (004), (200), (105), (211), and (204), respectively (JCPDS 00-021-1272) were detected. Unlike the TCN powders, the brookite peaks (JCPDS 00-029-1360) corresponding to (120) and (121) were observed at 25.4° and 30.8°, respectively in the XRD of the STCN powders. Also, addition of g-C_3N_4 hampered the formation of rutile phase despite calcination [85].

Intensity of g-C_3N_4 peaks in the STCN powders increased gradually as g-C_3N_4 content increased without shifting the peaks to lower or higher angles. Tough, the peak intensities for the anatase and brookite phases decreased. Wang et al. [33]

published akin results. It is obvious that the (101) peaks of anatase at 25.4° became distinct when TiO_2 content is 80 wt%. Other anatase peaks become clearer, too.

When the XRD patterns of the STCN powders are compared with each other, brookite TiO_2 phase is more visible in STCN-20. Unlike hydrothermal synthesis, the composite formation by the sol-gel process does not hinder brookite formation. Li et al. [29] detected brookite phase after the formation of g-C_3N_4/TiO_2 powders by the sol-gel process. Gunnar et.al [103] reported that anatase and brookite nano crystals formed as a result of low temperature and low pH synthesis conditions. It is believed that a 48 h mixing time and room temperature synthesis facilitate the brookite formation.

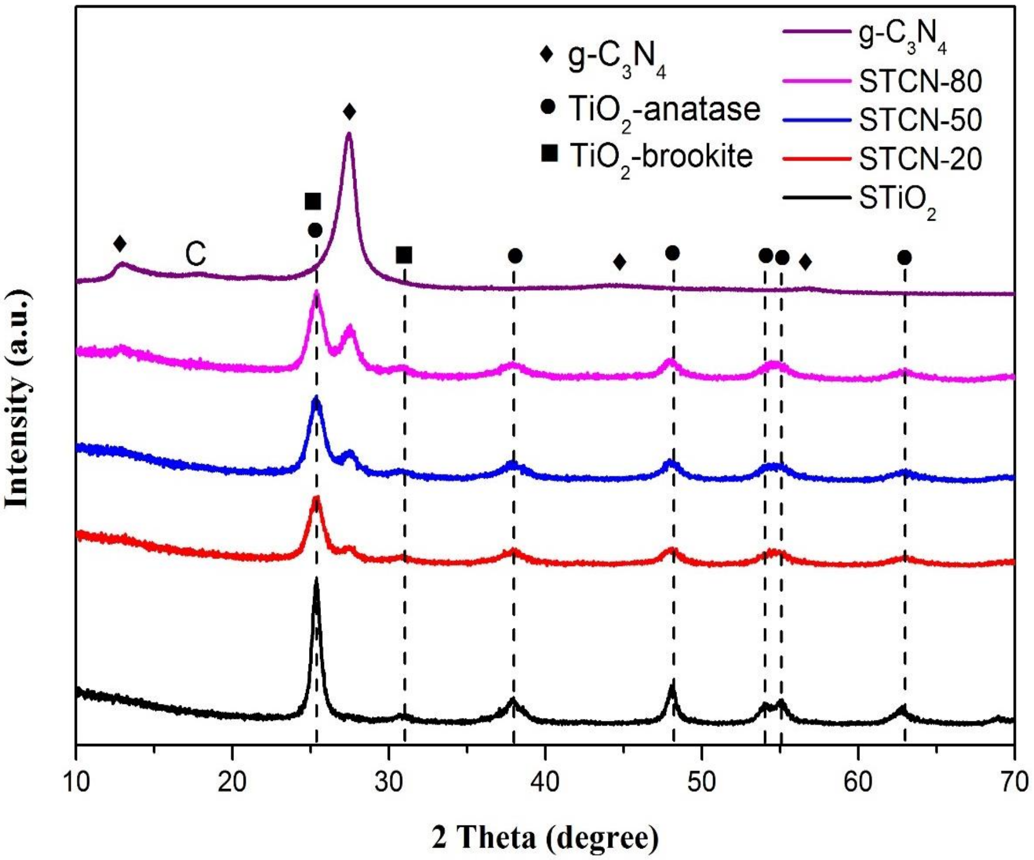

Figure 5.4. XRD patterns of the STCN, $STiO_2$, and g-C_3N_4 powders.

Table 5.1 lists the crystallite sizes of the STCN and $STiO_2$powders as calculated by Debye-Scherrer formula. Anatase crystallite size in the STCN powders is bigger than that in $STiO_2$ powder. Average size of anatase crystallites was 10.76 nm. With increasing g-C_3N_4 content in the STCN powders, anatase crystallite size decreased from 6.98 nm to 6.56 nm. These results reveal that g-C_3N_4 hinders the growth of anatase crystals [85].

As mentioned in Section 4.1.2, no data related to the crystallite size of g-C_3N_4 in the composites is available in literature. The crystallite size of pristine g-C_3N_4 is 5.01 nm as presented in Table 4.1. Crystallite size values of the STCN powders are closer to the size of g-C_3N_4 crystallites rather than that of anatase crystallites, which range between 4.46 and 5.52 nm. As seen in Table 5.1, g-C_3N_4 addition leads to the growth of g-C_3N_4 crystals.

The measured particle sizes reported in Section 5.2.1 is very different from the calculated crystallite sizes for both TiO_2 and g-C_3N_4 particles since they are different terms as discussed in Section 4.2.2.

Table 5.1 Crystallite sizes of the STCN powders.

Powder name	Crystallite Size (nm)	
	Anatase	g-C_3N_4
$STiO_2$	10.76	-
STCN-20	6.98	4.46
STCN-50	6.68	5.35
STCN-80	6.56	5.52

5.2.3 Morphological and Elemental Analyses

Representative FESEM images of the STCN powders are shown in Figure 5.5. Effect of g-C_3N_4 content on the morphology developed in the powders was investigated.

All images were taken at 100000 magnification but the image for the $STiO_2$ powder was taken at 400000 magnification as depicted in Figure 5.5 (a). Similar to pristine TiO_2 powder, $STiO_2$ powder consists of nearly spherical particles with a diameter of ranging from 8 to 33 nm. g-C_3N_4 powder was in a lamellar structure and its surface was flat as demonstrated in Figure 4.9 (a) but, the STCN powders comprised irregular shaped particles as shown in Figure 5.5 (b-d). The surface of g-C_3N_4 sheets became rougher because of the growth of TiO_2 particles [52]. Almost all g-C_3N_4 sheets were covered by the nano size TiO_2 particles. As seen in Figure 5.5 (b), STCN-20 powder includes some agglomerated TiO_2 particles with 11 to 37 nm particle size. There is no distinct difference in the morphologies between STCN-20 and STCN-50 powders. See Figure 5.5 (c). Particle sizes and shapes are more or less the same in both powders. Nonetheless, TiO_2 nanoparticles in STCN-50 powder are more uniform representing good heterojunction formation. Figure 5.5 (d) shows the image of STCN-80 powder. Although TCN-80 powder includes particles as big as micrometer in size, STCN-80 powder comprises smaller particles in the range from 13 to 35 nm in size. The microstructure of this powder is a bit different from the other particles. It is observed that TiO_2 nanoparticles with an average diameter of 35 nm are agglomerated on some edges or corners of the g-C_3N_4 sheets.

All of the STCN powders are in the nano size range hence, they are named nanopowders based on the FESEM images. When the morphologies of STCN-50 and STCN-80 nanopowders are compared with each other, the dispersity of TiO_2 nanoparticles were higher in STCN-50 powders which directly affect the photocatalytic activity [83].

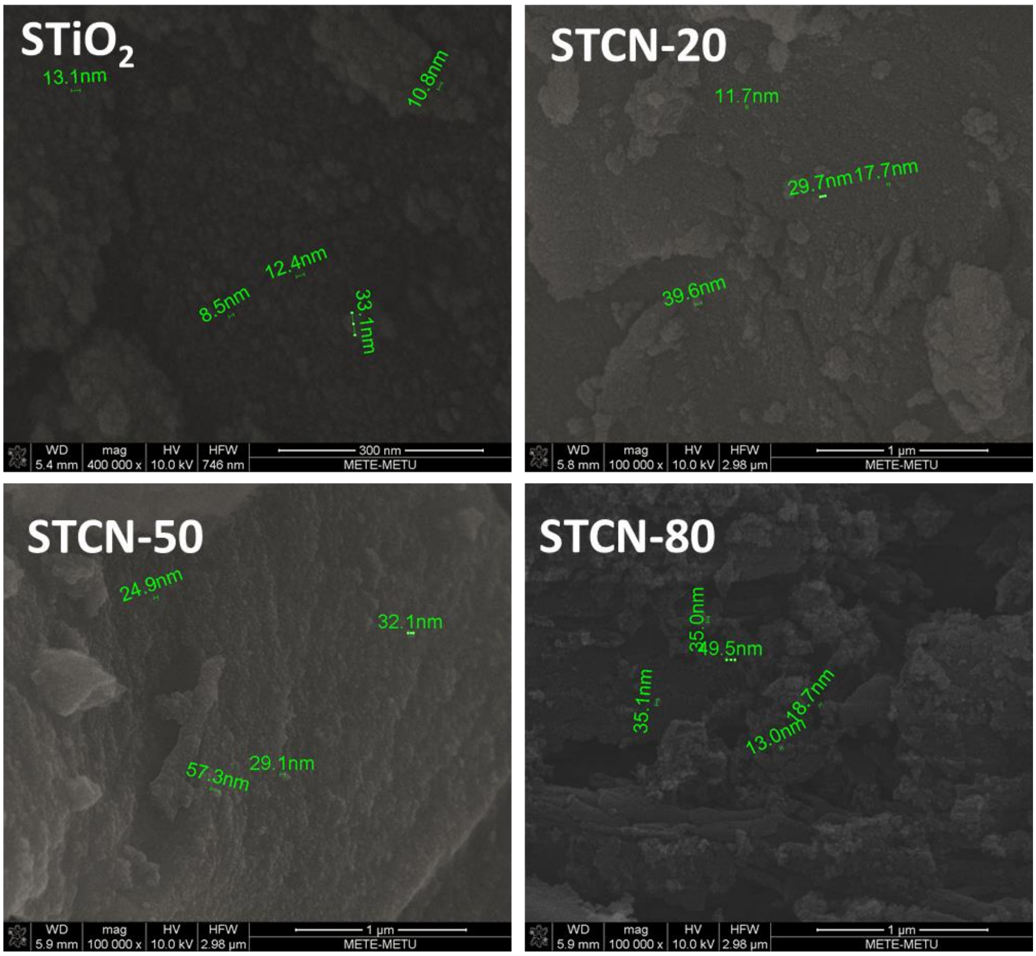

Figure 5.5. FESEM images of a) $STiO_2$ powders, b) STCN-20, c) STCN-50 and d) STCN-80 powders.

The EDS spectra of $STiO_2$ and STCN-50 powders are shown in Figure 5.6. $STiO_2$ powder composed of only Ti and O whereas, STCN-50 nanopowder contains C and N in addition to Ti and O. Au is detected due to Au coating of the powders.

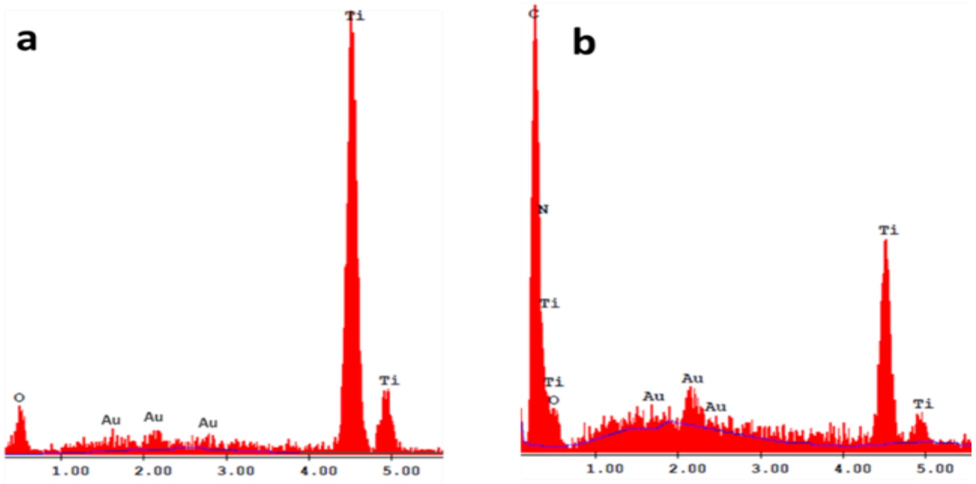

Figure 5.6. EDS spectra of a) pristine $STiO_2$ and b) STCN-50 powders.

EDS data in terms of elemental composition for the STCN powders are given in Table 5.2. The findings confirmed that the STCN powders attained the desired quantity of the expected elements in terms of chemical composition. For example, STCN-50 powder has 55.77 wt% g-C_3N_4 and 44.23 wt% TiO_2. Moreover, the STCN powders consist of C, N, O and Ti. The EDS data suggest that there is an interfacial connection between TiO_2 and g-C_3N_4.

Table 5.2 Elemental analysis data for the STCN powders.

Powder	Composition (wt %)			
	C	N	O	Ti
$STiO_2$	0	0	32.61	67.61
STCN-20	11.35	6.12	26.51	59.07
STCN-50	45.39	10.38	8.54	25.52
STCN-80	47.41	24.33	6.02	22.23

5.2.4 Diffuse Reflectance Spectra (DRS) Analysis

Absorption threshold plots of the STCN powders together with pristine g-C_3N_4 powder are shown in Figure 5.7 (a). Estimated absorption edge values of the STCN powders are listed in Table 5.3. Similar to pristine TiO_2, $STiO_2$ powder has the absorption edge value of 431.4 nm that is in the UV-range. As previously described in Section 4.2.1, the absorption edge of g-C_3N_4 powder is 486.04 nm which is in the solar spectrum range. As anticipated, heterojunction formation extended operational wavelength region of $STiO_2$ powder. These nanopowders have an absorption range between 473.8 and 486.04 nm that is closest to value of g-C_3N_4. Growing $STiO_2$ nanoparticles on the g-C_3N_4 sheets improved the visible light absorption ability of TiO_2. [104]. Therefore, the STCN nanopowders exhibit a redshift when compared to $STiO_2$ nanopowder and they have absorption ability in both UV and visible light zone. This visible light absorption ability decreases the e^-/h^+ recombination with increasing oxidation and reduction reactions [83].

Absorbance versus wavelength graph shown in Figure 5.7 (a) was transformed into $(\alpha h v)^2$ versus photon energy plot using Tauc's transformation formula and depicted in Figure 5.7 (b). This plot provides a calculation of Eg values using an extrapolation of the linear part of the x vs y-axis. Calculated Eg values are listed in Table 5.3.

The STCN powders exhibit larger absorption edge values than the TCN powders whose absorption edge values were given previously in Table 4.5. They have lower E_g values than the TCN powders since the STCN powders still have some amount of brookite phase that has lower E_g value and decreases the E_g value of the STCN powders.

Table 5.3 Absorbance edge and band gap values of sol-gel synthesized powders.

Powder	Absorbance edge (nm)	Eg (eV)
$STiO_2$	431.4	3.10
STCN-20	473.8	2.75
STCN-50	479.2	2.72
STCN-80	481.2	2.71

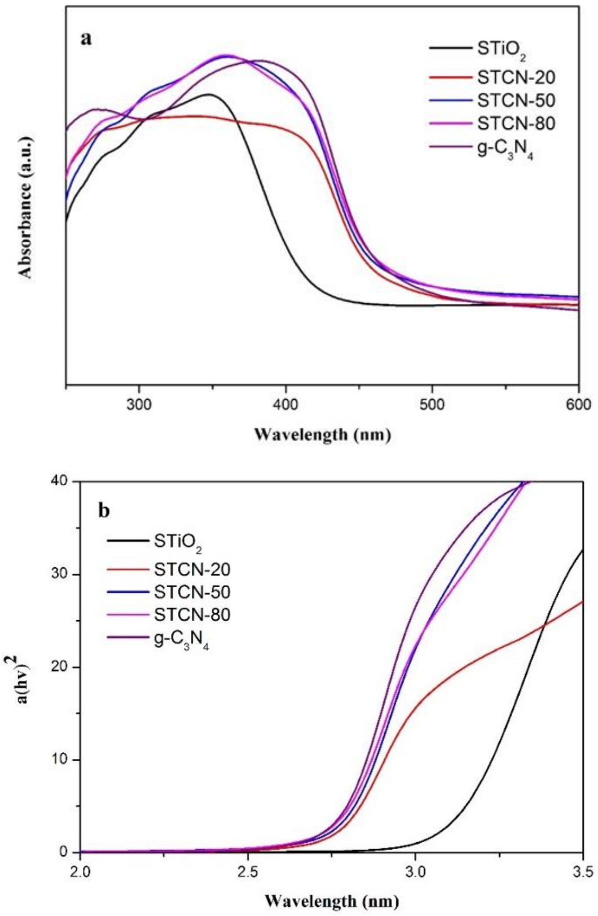

Figure 5.7. a) Absorbance edge spectra, b) $(\alpha h\nu)^2$versus photon energy $(h\nu)$ graph of the STCN powders.

5.2.5 Photocatalytic Activity of the Powders

Photocatalytic performances measured for the STCN powders and for some control groups under 3 h solar light irradiation is shown in Figure 5.8. The absorption and MB degradation values of the STCN powders in terms of percentage are presented in Table 5.4.

STiO$_2$ powder has a lower MB absorption value (3.92 %) in dark while the degradation value of STiO$_2$ powder is 49.10% under solar light illumination. As mentioned in Section 4.2.7, pristine g-C$_3$N$_4$ has 11.6% absorption and 45.5% MB degradation ability. All of the STCN powders exhibit higher absorption degradation value than $STiO_2$ powder and pristine g-C_3N_4 powder. See Figure 5.8 (a). STCN-20 powder has 82.63% MB degradation. By comparison of the MB degradation value of TCN-20 powders (see Table 4.6), STCN-20 powder exhibits quite higher photocatalytic activity. Data implies that there is a well-defined heterojunction between the g-C_3N_4 sheets and TiO_2 nanoparticles in the STCN powders as a result of long synthesizing time i.e, 48 h. Additionally, heat treatment is beneficial for photocatalytic activity [96]. Figure 5.8 (b) demonstrates the absorbance spectra of SCTN-50 nanopowder in the MB solution upon exposure to solar light for 180 min. Absorption peak intensity located at 664 nm decreased gradually with increasing exposure time. Increasing g-C_3N_4 content is beneficial for the MB degradation value of the STCN powders to some extent. STCN-50 powder has higher degradation value (87.05%) than STCN-80 powder that has a degradation value of 83.96%. The reason may be low content of TiO_2 nanoparticles limit the coated sites of the surface of the g-C_3N_4 [88].

Although their Eg values are closest the each other, their microstructures are different from each other which is another effect for photocatalytic activity. TiO_2 nanoparticles in STCN-50 powder are more dispersive than in $STiO_2$ powders. This dispersity of TiO_2 nanoparticles accelerates the movement of photogenerated carriers and affects the photocatalytic activity of the powders positively [83].

Figure 5.8 (c) demonstrates the photocatalytic activity of STCN-50 powder with a comparison between the control groups namely; $STiO_2$ powder, g-C_3N_4 powder, blank (MB), and P25 powder. As stated previously, $STiO_2$ powder have 49.1% MB degradation ability under solar light. This result is very higher when compared to pristine TiO_2 powder. See Table 4.6. The calcination at temperature of 400 °C and higher amounts of brookite may affect the degradation ability positively.

These results reveal that STCN-50 powder have better photocatalytic ability than pristine g-C_3N_4 powder under solar light illumination. Photocatalytic activity of STCN-50 powder (87.05%) almost two times better than pristine g-C_3N_4 (45.5%). Furthermore, this nanopowder has better photocatalytic activity than P25 powder

(80.58%). See Table 4.6. P25 owns the better photocatalytic activity regarding to literature thanks to its special structure that contains both anatase and rutile phases [105].

STCN-50 powder has higher degradation ability than TCN-50 powder (70.7%). The higher degradation ability is attributed to different reasons. Lower Eg value of STCN-50 powder may be the one of the reasons, which increase the photogenerated charge carriers. Also, calcination applied to STCN-50 powder is beneficial for photocatalytic activity.

When compared to the TCN powders, most of the STCN powders exhibit better degradation ability due to their nano size effect. Yu et al. [106] proved that anatase and brookite mixture exhibits the higher photocatalytic activity than P25 powder. The STCN powders consist of anatase, brookite and g-C_3N_4 mixture. Thus, interaction between these three phases may affect the photocatalytic activity.

Table 5.4 Absorbance and MB degradation results of sol-gel synthesized powders.

Powder	Absorbance (%) (at dark)	MB Degradation (%) (under solar light illumination)		
	30 min	1 h	2 h	3 h
$STiO_2$	3.92	9.81	26.68	49.10
STCN-20	34.35	57.75	72.66	82.63
STCN-50	19.03	58.03	79.82	87.05
STCN-80	40.98	61.43	75.72	83.96

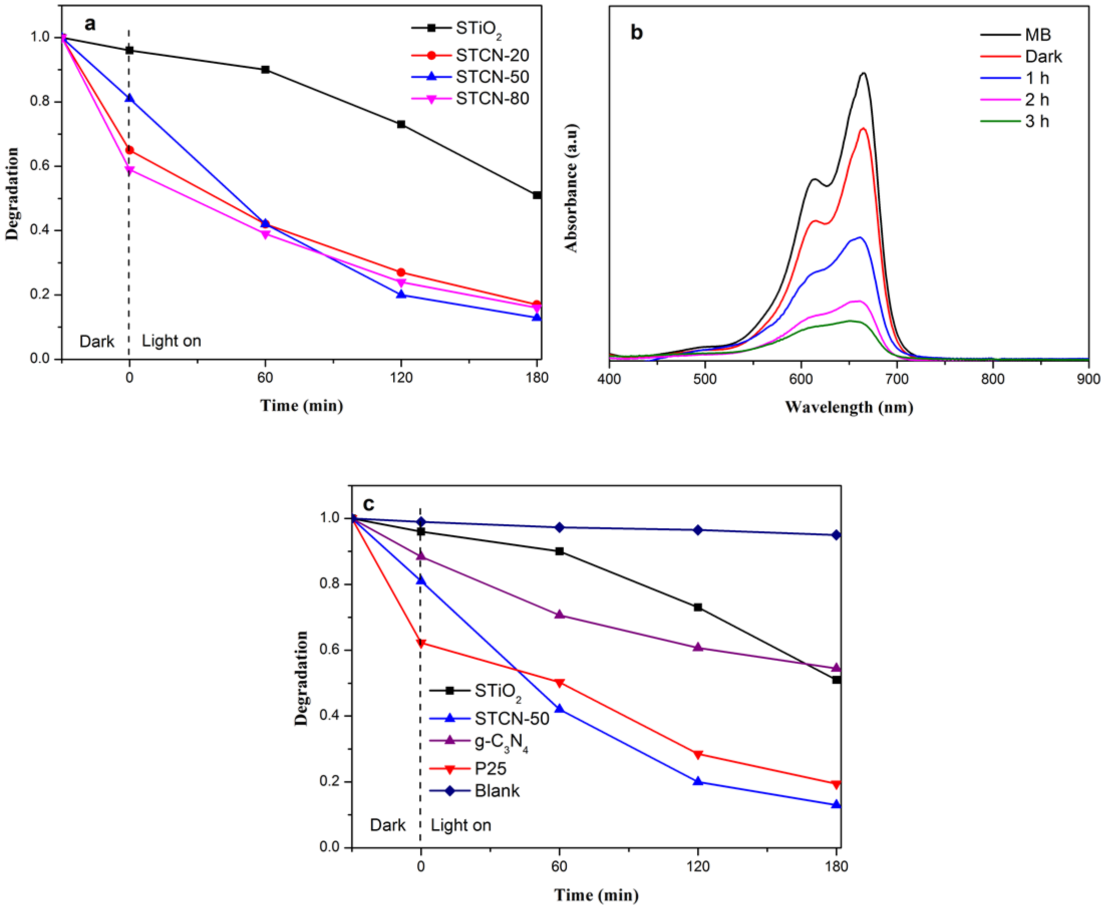

Figure 5.8. a) Photodegradation values of STCN powders, b) UV-vis absorption spectra of STCN-50 powder, c) photodegradation of STCN-50 powder compared with control groups.

CHAPTER 6

CONCLUSIONS

The solar light sensitive g-C_3N_4/TiO_2 composites containing various amounts of graphitic carbon nitride (g-C_3N_4) and titania (TiO_2) are successfully prepared by the hydrothermal and sol-gel processes for photocatalytic applications. FESEM and EDS analyses revealed that all composites prepared are in nano size range and developed through deposit of TiO_2 nanoparticles on g-C_3N_4 sheets via hydrothermal or sol-gel reactions. An interface between the constituents of the nanocomposites was evidenced through the XRD, FTIR, and Raman analyses. The heterojunction construction among g-C_3N_4 and TiO_2 powders extends the absorption edge of pristine TiO_2 powders by redshifting. The redshift of visible light regions improves separation time of the photogenerated charge carriers. All g-C_3N_4/TiO_2 composites exhibit the photocatalytic ability to degrade aqueous Methylene Blue (MB) solution under solar light illumination. Except for the hydrothermally derived g-C_3N_4/TiO_2 composite containing 20 wt% g-C_3N_4, all g-C_3N_4/TiO_2 composites exhibit superior photocatalytic activity for the degradation of MB to both pristine TiO_2 powder and pristine g-C_3N_4 powder. Among all hydrothermally prepared composites, the g-C_3N_4/TiO_2 composite containing 80 wt% g-C_3N_4 shows the best photocatalytic activity. The photocatalytic efficiency of the hydrothermally derived g-C_3N_4/TiO_2 composites are improved if they are subjected to regulated heat treatments at temperatures ranging from 350 to 500 ^oC for 1 h. Hydrothermally derived and sol-gel derived g-C_3N_4/TiO_2 composites exhibited good photocatalytic efficiency in 180 min solar light illumination. The composite containing 80 wt% g-C_3N_4 and heat-treated at 400 ^oC for 1 h exhibited MB photodegradation efficiency ~2.2 times better than pristine g-C_3N_4 powder besides ~1.5 times better than pristine TiO_2 powder. The enhancement in photocatalytic activity was related to the creation of reactive oxidation species encouraged by photogenerated electrons and reduced recombination rate of the e^-/h^+ pairs.

The sol-gel derived g-C_3N_4/TiO_2 composite containing 50 wt% g-C_3N_4 showed better photocatalytic efficiency than pristine g-C_3N_4 and P25 powders. This composite shows the photocatalytic efficiency ~1.8 times better than pristine TiO_2 powder and ~2.2 times better than pristine g-C_3N_4 powder.

Hydrothermally synthesized composites exhibit 100% while sol-gel prepared exhibits 87.05% photocatalytic activity under 3 h solar light illumination.

REFERENCES

[1] L. Zhou, L. Wang, J. Zhang, J. Lei, and Y. Liu, “The preparation, and applications of g-C_3N_4/TiO_2 heterojunction catalysts—a review,” Res. Chem. Intermed., vol. 43, no. 4, pp. 2081–2101, 2017.

[2] M. B. Ansari, B. H. Min, Y. H. Mo, and S. E. Park, “CO_2 activation and promotional effect in the oxidation of cyclic olefins over mesoporous carbon nitrides,” Green Chem., vol. 13, no. 6, pp. 1416–1421, 2011.

[3] Y. Peng, X. Shen, L. Wang, B. Tian, Y. Liu, and H. Chen, “Preparation of porous TiO_2 photocatalyts with different crystal phases and high catalytic activity by simple calcination of titanate nanofibers,” RSC Adv., vol. 7, no. 72, pp. 45742–45745, 2017.

[4] M. Xing, J. Zhang, F. Chen, and B. Tian, “An economic method to prepare vacuum activated photocatalysts with high photo-activities and photosensitivities,” Chem. Commun., vol. 47, no. 17, pp. 4947–4949, 2011.

[5] L. Gracia and J. Andre, “Density Functional Theory Study of the Brookite Surfaces and Phase Transitions between Natural Titania Polymorphs,” pp. 23417–23423, 2006.

[6] R. Kaplan and G. Draˇ, “Applied Catalysis B : Environmental Simple synthesis of anatase/rutile/brookite TiO_2 nanocomposite with superior mineralization potential for photocatalytic degradation of water pollutants,” vol. 181, pp. 465–474, 2016.

[7] N. Erdogan, A. Ozturk, and J. Park, “Hydrothermal synthesis of 3D TiO_2 nanostructures using nitric acid: Characterization and evolution mechanism,” Ceram. Int., vol. 42, pp. 5985–5994, 2015.

[8] Y. Liao, W. Que, Q. Jia, Y. He, and P. Zhong, “Journal of Materials Chemistry,” pp. 7937–7944, 2012.

[9] Y. Li, K. Lv, W. Ho, F. Dong, X. Wu, and Y. Xia, “Hybridization of rutile TiO_2($rTiO_2$) with g-C_3N_4 quantum dots (CN QDs): An efficient visible-light-driven Z-scheme hybridized photocatalyst,” Appl. Catal. B Environ., vol. 202, pp. 611–619, 2017.

[10] H. Diker, C. Varlikli, K. Mizrak, and A. Dana, “Characterizations and photocatalytic activity comparisons of N-doped nc-TiO_2 depending on synthetic conditions and structural differences of amine sources,” Energy, vol. 36, no. 2, pp. 1243–1254, 2011.

[11] S. Ouyang, Y. Bi, N. Umezawa, J. Ye, H. Tong, and M. Oshikiri, “Nano-photocatalytic Materials: Possibilities and Challenges,” Adv. Mater., vol. 24, no. 2, pp. 229–251, 2011.

[12] S. M. Gupta and M. Tripathi, “A review of TiO_2 nanoparticles,” Chinese Sci. Bull., vol. 56, no. 16, pp. 1639–1657, 2011.

[13] L. Zheng, X. Xiao, Y. Li, and W. Zhang, “Enhanced photocatalytic activity of TiO_2 nanoparticles using WS_2/g-C_3N_4 hybrid as co-catalyst,” Trans. Nonferrous Met. Soc. China, vol. 27, no. 5, pp. 1117–1126, 2017.

[14] N. Erdogan, J. Park, W. Choi, S. Y. Kim, and A. Ozturk, “ Alkaline Hydrothermal Synthesis, Characterization, and Photocatalytic Activity of TiO_2 Nanostructures: The Effect of Initial TiO_2 Phase ,” J. Nanosci. Nanotechnol., vol. 19, no. 3, pp. 1511–1519, 2018.

[15] H. Wang, X. Gao, G. Duan, X. Yang, and X. Liu, “Facile preparation of anatase-brookite-rutile mixed-phase N-doped TiO_2 with high visible-light photocatalytic activity,” J. Environ. Chem. Eng., vol. 3, no. 2, pp. 603–608, 2015.

[16] H. Chen, D. Kuang, and C. Su, “Hierarchically micro/nanostructured photoanode materials for dye-sensitized solar cells,” J. Mater. Chem., vol. 22, no. 31, p. 15475, 2012.

[17] T. Xiao, Z. Tang, Y. Yang, L. Tang, Y. Zhou, and Z. Zou, “In situ construction of hierarchical WO_3/g-C_3N_4 composite hollow microspheres as a Z-scheme photocatalyst for the degradation of antibiotics,” Appl. Catal. B Environ., vol. 220, no. June 2017, pp. 417–428, 2018.

[18] G. Dong, Y. Zhang, Q. Pan, and J. Qiu, “A fantastic graphitic carbon nitride (g-C_3N_4) material: Electronic structure, photocatalytic and photoelectronic properties,” J. Photochem. Photobiol. C Photochem. Rev., vol. 20, no. 1, pp. 33–50, 2014.

[19] Z. Tong, D. Yang, T. Xiao, Y. Tian, and Z. Jiang, “Biomimetic fabrication of g-C_3N_4/TiO_2 nanosheets with enhanced photocatalytic activity toward organic pollutant degradation,” Chem. Eng. J., vol. 260, pp. 117–125, 2015.

[20] S. Siuleiman, N. Kaneva, A. Bojinova, D. Dimitrov, and K. Papazova, “ZnO/TiO_2 coupled semiconductor photocatalysts,” vol. 49, pp. 199–204, 2017.

[21] M. Scarisoreanu, C. Fleaca, I. Morjan, A. Niculescu, E. Dutu, and E. Vasila, “High photoactive TiO_2/SnO_2 nanocomposites prepared by laser pyrolysis,” Appl. Surf. Sci., vol. 418, pp. 491–498, 2017.

[22] N. Abbas, G. N. Shao, M. S. Haider, S. M. Imran, S. S. Park, and H. T. Kim, “Sol–gel synthesis of TiO_2-Fe_2O_3 systems: Effects of Fe_2O_3 content and their photocatalytic properties,” J. Ind. Eng. Chem., vol. 39, pp. 112–120, 2016.

[23] Z. Lian et al., “C60-decorated CdS/TiO_2 mesoporous architectures with enhanced photostability and photocatalytic activity for H_2 evolution,” ACS Appl. Mater. Interfaces, vol. 7, no. 8, pp. 4533–4540, 2015.

[24] Q. Gao, L. Duan, X. Zhang, I. Kamiya, and W. Lü, “Graphitic carbon nitride modified {001}-faceted TiO_2 nanosheet photoanodes for efficient quantum dot sensitized solar cells,” Superlattices Microstruct., vol. 109, pp. 860–868, 2017.

[25] A. Nikokavoura and C. Trapalis, "Graphene and g-C_3N_4 based photocatalysts for NO_x removal: A review," Appl. Surf. Sci., vol. 430, no. x, pp. 18–52, 2018.

[26] A. T. Kuvarega, R. W. M. Krause, and B. B. Mamba, "Multiwalled carbon nanotubes decorated with nitrogen, palladium co-doped TiO_2 (MWCNT/n, Pd co-doped TiO_2) for visible light photocatalytic degradation of eosin yellow in water," Nanotechnol. Sustain. Dev. First Ed., vol. 2, pp. 73–88, 2014.

[27] S. Kumar, S. Karthikeyan, and A. Lee, "g-C_3N_4-Based Nanomaterials for Visible Light-Driven Photocatalysis," Catalysts, vol. 8, no. 2, p. 74, 2018.

[28] R. Fagan, D. E. McCormack, S. J. Hinder, and S. C. Pillai, "Photocatalytic properties of g-C_3N_4-TiO_2 heterojunctions under UV and visible light conditions," Materials (Basel)., vol. 9, no. 4, 2016.

[29] H. Li, X. Wu, S. Yin, K. Katsumata, and Y. Wang, "Effect of rutile TiO_2 on the photocatalytic performance of g-C_3N_4/brookite-TiO_2-xNy photocatalyst for NO decomposition," Appl. Surf. Sci., vol. 392, pp. 531–539, 2017.

[30] L. Zhou, L. Wang, J. Lei, Y. Liu, and J. Zhang, "Fabrication of TiO_2/Co-g-C_3N_4 heterojunction catalyst and its photocatalytic performance," Catal. Commun., vol. 89, pp. 125–128, 2017.

[31] H. Zhao, X. Quan, S. Chen, Y. Zhan and H. Wang, "Fabrication of atomic single layer graphitic-C_3N_4 and its high performance of photocatalytic disinfection under visible light irradiation," Appl. Catal. B Environ., vol. 152–153, pp. 46–50, 2014.

[32] D. Fu, G. Han, F. Liu, Y. Xiao, H. Wang and R. Liu"Visible-light enhancement of methylene blue photodegradation by graphitic carbon nitride-titania composites," Mater. Sci. Semicond. Process., vol. 27, pp. 966–974, 2014.

[33] C. Wang et al., "Preparation of TiO_2/g-C_3N_4 composites and their application in photocatalytic oxidative desulfurization," Ceram. Int., vol. 40, no. 8 PART

A, pp. 11627–11635, 2014.

[34] X. Chen, W. Zhu, Y. Xu, H. Xu, M. Zhang, S. Yin and H. Li , “Growth of g-C_3N_4 on mesoporous TiO_2 spheres with high photocatalytic activity under visible light irradiation,” Appl. Catal. B Environ., vol. 188, pp. 342–350, 2016.

[35] D. Fan, C. Guo, H. Ma, D. Zhao, Y. Li, D. Wu, and Q. Wei, “Facile fabrication of an aptasensor for thrombin based on graphitic carbon nitride/TiO_2 with high visible-light photoelectrochemical activity,” Biosens. Bioelectron., vol. 75, pp. 116–122, 2016.

[36] G. Jiang, X. Yang, Y. Wu, Z. Li, Y. Han, and X. Shen, “A study of spherical TiO_2/g-C_3N_4 photocatalyst: Morphology, chemical composition and photocatalytic performance in visible light,” Mol. Catal., vol. 432, pp. 232–241, 2017.

[37] J. Zhou, M. Zhang, and Y. Zhu, “Photocatalytic enhancement of hybrid C_3N_4/TiO_2 prepared via ball milling method,” Phys. Chem. Chem. Phys., vol. 17, no. 5, pp. 3647–3652, 2015.

[38] Y. Wang, W. Yang, X. Chen, J. Wang, and Y. Zhu, “Photocatalytic activity enhancement of core-shell structure g-C_3N_4@TiO_2 via controlled ultrathin g-C_3N_4 layer,” Appl. Catal. B Environ., vol. 220, pp. 337–347, 2018.

[39] Z. Li, G. Jiang, Z. Zhang, Y. Wu, and Y. Han, “Phosphorus-doped g-C_3N_4 nanosheets coated with square flake-like TiO2: Synthesis, characterization and photocatalytic performance in visible light,” J. Mol. Catal. A Chem., vol. 425, pp. 340–348, 2016.

[40] X. Yu, X. Fan, L. An, G. Liu, Z. Li and P. Hu, “Mesocrystalline Ti^{3+}-TiO_2 hybridized g-C_3N_4 for efficient visible-light photocatalysis,” Carbon N. Y., vol. 128, pp. 21–30, 2018.

[41] R. Saravanan, F. Gracia, and A. Stephen, “Basic Principles , Mechanism , and

Challenges of Photocatalysis," pp. 19–41, 2017.

[42] R. Ameta, M. S. Solanki, S. Benjamin, and S. C. Ameta, "Composites for environmental engineering". 2018.

[43] Y. Yuan, L. Zhang, J. Xing, M. Utama, X. Lu, K. Du and Q. Xiaong, "High-yield synthesis and optical properties of g-C_3N_4" Nanoscale, vol. 7, no. 29, pp. 12343–12350, 2015.

[44] H. Kato and A. Kudo, "Visible-light-response and photocatalytic activities of TiO_2 and $SrTiO_3$ photocatalysts codoped with antimony and chromium," J. Phys. Chem. B, vol. 106, no. 19, pp. 5029–5034, 2002.

[45] D. Jing and L. Guo, "A novel method for the preparation of a highly stable and active CdS photocatalyst with a special surface nanostructure," J. Phys. Chem. B, vol. 110, no. 23, pp. 11139–11145, 2006.

[46] W. Wang, B. Cheng, J. Yu, G. Liu, and W. Fan, "Visible-light photocatalytic activity and deactivation mechanism of Ag_3PO_4 spherical particles," Chem. - An Asian J., vol. 7, no. 8, pp. 1902–1908, 2012.

[47] C. Pan and Y. Zhu, "New Type of $BiPO_4$ Oxy-acid salt photocatalyst with high photocatalytic activity on degradation of dye," Environ. Sci. Technol., vol. 44, no. 14, pp. 5570–5574, 2010.

[48] Mohamed A. Barakat Rajeev Kumar, "Photocatalytic activity enhancement of TiO_2 nanoparticles," S. Briefs and I. N. Molecular.

[49] M. Ghanashyam Krishna, M. Vinjanampati, and D. Dhar Purkayastha, "Metal oxide thin films and nanostructures for self-cleaning applications: current status and future prospects," Eur. Phys. J. Appl. Phys., vol. 62, no. 3, p. 30001, 2013.

[50] S. G. Kumar and K. S. R. K. Rao, "Crystal structures using a solution-based approach :," Nanoscale, vol. 6, pp. 11574–11632, 2014.

[51] A. Di Paola, M. Bellardita, L. Palmisano, S. P. Group, D. Energia, and I. Informazione, Brookite, the Least Known TiO_2 Photocatalyst. 2013.

[52] Z. Sun, C. Li, G. Yao, and S. Zheng, "In situ generated g-C_3N_4/TiO_2 hybrid over diatomite supports for enhanced photodegradation of dye pollutants," Mater. Des., vol. 94, pp. 403–409, 2016.

[53] S. Rehman, R. Ullah, A. M. Butt, and N. D. Gohar, "Strategies of making TiO_2 and ZnO visible light active," vol. 170, pp. 560–569, 2009.

[54] J. Diaz-Angulo, I. Gomez-Bonilla, C. Jimenez-Tohapanta, M. Mueses, M. Pinzon, and F. Machuca-Martinez, "Visible-light activation of TiO_2 by dye-sensitization for degradation of pharmaceutical compounds," Photochem. Photobiol. Sci., vol. 18, no. 4, pp. 897–904, 2019.

[55] Y. Zhang, X. Xiang, Y. Han, X. Zhan and F. Shen, "Photoelectrocatalytic degradation of recalcitrant organic pollutants using TiO_2 film electrodes: An overview," Chemosphere, vol. 88, no. 2, pp. 145–154, 2012.

[56] A. Zaleska, "Doped-TiO_2: A Review," Recent Patents Eng., vol. 2, no. 3, pp. 157–164, 2008.

[57] R. Daghrir, P. Drogui, and D. Robert, "Modified TiO_2 For Environmental Photocatalytic Applications : A Review," 2013.

[58] K. Palanivelu, J.-S. Im, and Y.-S. Lee, " Carbon Doping of TiO_2 for Visible Light Photo Catalysis - A review ," Carbon Lett., vol. 8, no. 3, pp. 214–224, 2007.

[59] S. A. Ansari, M. M. Khan, M. O. Ansari, and M. H. Cho, "Nitrogen-doped titanium dioxide (N-doped TiO_2) for visible light photocatalysis," New J. Chem., vol. 40, no. 4, pp. 3000–3009, 2016.

[60] L. G. Devi and R. Kavitha, "Enhanced photocatalytic activity of sulfur doped TiO_2 for the decomposition of phenol: A new insight into the bulk and surface modification," Mater. Chem. Phys., vol. 143, no. 3, pp. 1300–1308, 2014.

[61] Q. Zhang, Y. Li, E. A. Ackerman, M. Gajdardziska-Josifovska, and H. Li, “Visible light responsive iodine-doped TiO_2 for photocatalytic reduction of CO_2 to fuels,” Appl. Catal. A Gen., vol. 400, no. 1–2, pp. 195–202, 2011.

[62] H. Wang and J. P. Lewis, “Second-generation photocatalytic materials: Anion-doped TiO_2,” J. Phys. Condens. Matter, vol. 18, no. 2, pp. 421–434, 2006.

[63] M. Ilieva, A. Nakova, and V. Tsakova, “TiO_2/WO_3 hybrid structures produced through a sacrificial polymer layer technique for pollutant photoand photoelectrooxidation under ultraviolet and visible light illumination,” J. Appl. Electrochem., vol. 42, no. 2, pp. 121–129, 2012.

[64] D. S. Su, S. Perathoner, and G. Centi, “Nanocarbons for the development of advanced catalysts,” Chem. Rev., vol. 113, no. 8, pp. 5782–5816, 2013.

[65] S. Ye, R. Wang, M. Z. Wu, and Y. P. Yuan, “A review on g-C_3N_4 for photocatalytic water splitting and CO_2 reduction,” Appl. Surf. Sci., vol. 358, pp. 15–27, 2015.

[66] H. Tang, S. Chang, L. Jiang, G. Tang, and W. Liang, “Novel spindle-shaped nanoporous TiO_2 coupled graphitic g-C_3N_4 nanosheets with enhanced visible-light photocatalytic activity,” Ceram. Int., vol. 42, no. 16, pp. 18443–18452, 2016.

[67] X. Zhou, F. Peng, H. Wang, H. Yu, and Y. Fang, “Carbon nitride polymer sensitized TiO_2 nanotube arrays with enhanced visible light photoelectrochemical and photocatalytic performance,” Chem. Commun., vol. 47, no. 37, pp. 10323–10325, 2011.

[68] S. Dyjak, W. Kiciński, and A. Huczko, “Thermite-driven melamine condensation to CxNyHz graphitic ternary polymers: Towards an instant, large-scale synthesis of g-C_3N_4,” J. Mater. Chem. A, vol. 3, no. 18, pp. 9621–9631, 2015.

[69] H. Y. Xu, L. C. Wu, H. Zhao, L. G. Jin, and S. Y. Qi, “Synergic Effect between Adsorption and Photocatalysis of Metal-Free g-C_3N_4 Derived from Different Precursors,” PLoS One, vol. 10, no. 11, pp. 1–20, 2015.

[70] G. Mamba and A. K. Mishra, “Graphitic carbon nitride (g-C_3N_4) nanocomposites: A new and exciting generation of visible light driven photocatalysts for environmental pollution remediation,” Appl. Catal. B Environ., vol. 198, pp. 347–377, 2016.

[71] X. Zhou et al., “A carbon nitride/TiO_2 nanotube array heterojunction visible-light photocatalyst: Synthesis, characterization, and photoelectrochemical properties,” J. Mater. Chem., vol. 22, no. 34, pp. 17900–17905, 2012.

[72] Y. Wang, J. Hong, W. Zhang, and R. Xu, “Carbon nitride nanosheets for photocatalytic hydrogen evolution: Remarkably enhanced activity by dye sensitization,” Catal. Sci. Technol., vol. 3, no. 7, pp. 1703–1711, 2013.

[73] S. M. Lam, J. C. Sin, and A. R. Mohamed, “A review on photocatalytic application of g-C_3N_4/semiconductor (CNS) nanocomposites towards the erasure of dyeing wastewater,” Mater. Sci. Semicond. Process., vol. 47, pp. 62–84, 2016.

[74] C. Yang, J. Qin, Z. Xue, M. Ma, X. Zhang, and R. Liu, “Rational design of carbon-doped TiO_2 modified g-C_3N_4 via in-situ heat treatment for drastically improved photocatalytic hydrogen with excellent photostability,” Nano Energy, vol. 41, no. August, pp. 1–9, 2017.

[75] H. Yan and H. Yang, “TiO_2 -g-C_3N_4 composite materials for photocatalytic H_2 evolution under visible light irradiation,” J. Alloys Compd., vol. 509, no. 4, pp. 26–29, 2011.

[76] L. Gu, J. Wang, Z. Zou, and X. Han, “Graphitic-C_3N_4-hybridized TiO_2 nanosheets with reactive {001} facets to enhance the UV- and visible-light photocatalytic activity,” J. Hazard. Mater., vol. 268, pp. 216–223, 2014.

[77] J. Wang and W. De Zhang, “Modification of TiO_2 nanorod arrays by graphite-like C_3N_4 with high visible light photoelectrochemical activity,” Electrochim. Acta, vol. 71, pp. 10–16, 2012.

[78] N. Boonprakob et al., “Enhanced visible-light photocatalytic activity of g-C_3N_4/TiO_2 films,” J. Colloid Interface Sci., vol. 417, pp. 402–409, 2014.

[79] X. Lu, Q. Wang, and D. Cui, “Preparation and Photocatalytic Properties of g-C_3N_4/TiO_2 Hybrid Composite,” J. Mater. Sci. Technol., vol. 26, no. 10, pp. 925–930, 2010.

[80] J. Shen, H. Yang, Q. Shen, Y. Feng, and Q. Cai, “Template-free preparation and properties of mesoporous g-C_3N_4/TiO_2 nanocomposite photocatalyst,” CrystEngComm, vol. 16, no. 10, pp. 1868–1872, 2014.

[81] Y. Li, J. Wang, Y. Zhang and D. He, “Seed-induced growing various TiO_2 nanostructures on g-C_3N_4 nanosheets with much enhanced photocatalytic activity under visible light,” J. Hazard. Mater., vol. 292, pp. 79–89, 2015.

[82] C. Li, Z. Sun, Y. Xue, G. Yao, and S. Zheng, “A facile synthesis of g-C_3N_4/TiO_2 hybrid photocatalysts by sol-gel method and its enhanced photodegradation towards methylene blue under visible light,” Adv. Powder Technol., vol. 27, no. 2, pp. 330–337, 2016.

[83] K. Namratha and K. Byrappa, “Novel solution routes of synthesis of metal oxide and hybrid metal oxide nanocrystals,” Prog. Cryst. Growth Charact. Mater., vol. 58, no. 1, pp. 14–42, 2012.

[84] R. Hao, G. Wang, C. Jiang, H. Tang, and Q. Xu, “In situ hydrothermal synthesis of g-C_3N_4/TiO_2 heterojunction photocatalysts with high specific surface area for Rhodamine B degradation,” Appl. Surf. Sci., vol. 411, pp. 400–410, 2017.

[85] B. G. Rao, D. Mukherjee and B. Reddy, “Sol Gel Process Novel approaches for preparation of nanoparticles,” 2017.

[86] Z. Chen, G. Zhao, H. Li, G. Han, and B. Song, "Effects of Water Amount and pH on the Crystal Behavior of a TiO_2 Nanocrystalline Derived from a Sol–Gel Process at a Low Temperature," vol. 1029, no. 25521, pp. 1024–1029, 2009.

[87] J. Li, Y. Liu, H. Li, and C. Chen, "Fabrication of g-C_3N_4/TiO_2 composite photocatalyst with extended absorption wavelength range and enhanced photocatalytic performance," J. Photochem. Photobiol. A Chem., vol. 317, pp. 151–160, 2016.

[88] X. Wang, Q. Wang, F. Li, W. Yang and Y. Hao, "Novel BiOCl-C_3N_4 heterojunction photocatalysts : In situ preparation via an ionic-liquid-assisted solvent-thermal route and their visible-light photocatalytic activities," Chem. Eng. J., vol. 234, pp. 361–371, 2013.

[89] R. Hao, G. Wang, H. Tang, L. Sun, C. Xu, and D. Han, "Template-free preparation of macro/mesoporous g-C_3N_4/TiO_2 heterojunction photocatalysts with enhanced visible light photocatalytic activity," Appl. Catal. B Environ., vol. 187, pp. 47–58, 2016.

[90] N. Erdogan, A. Bouziani, J. Park, M. Micusik, S. Kim, E. Majkova, M. Omastova, and A. Öztürk, "Synthesis and enhanced photocatalytic activity of nitrogen-doped triphasic TiO_2 nanoparticles," J. Photochem. Photobiol. A Chem., vol. 377, no. April, pp. 92–100, 2019.

[91] L. Svoboda, P. Praus, M. Lima, M. Ritz, and J. Faria, "Graphitic carbon nitride nanosheets as highly efficient photocatalysts for phenol degradation under high-power visible LED irradiation," Mater. Res. Bull., vol. 100, no. October, pp. 322–332, 2018.

[92] W. N. Wang, W. Widiyastuti, T. Ogi, I. W. Lenggoro, and K. Okuyama, "Correlations between crystallite/particle size and photoluminescence properties of submicrometer phosphors," Chem. Mater., vol. 19, no. 7, pp. 1723–1730, 2007.

[93] C. Li, Z. Sun, W. Zhang, C. Yu, and S. Zheng, “Highly efficient g-C_3N_4/TiO_2/kaolinite composite with novel three-dimensional structure and enhanced visible light responding ability towards ciprofloxacin and S. aureus,” Appl. Catal. B Environ., vol. 220, no. May 2017, pp. 272–282, 2018.

[94] Y. Hu, H. L. Tsai, and C. L. Huang, “Phase transformation of precipitated TiO_2 nanoparticles,” Mater. Sci. Eng. A, vol. 344, no. 1–2, pp. 209–214, 2003.

[95] G. Zhang et al., “An ingenious strategy of preparing TiO_2/g-C_3N_4 heterojunction photocatalyst: In situ growth of TiO_2 nanocrystals on g-C_3N_4 nanosheets via impregnation-calcination method,” Appl. Surf. Sci., vol. 433, pp. 963–974, 2018.

[96] C. Wang, W. Zhu, Y. Xu, M. Zhang, “Preparation of TiO_2/g-C_3N_4 composites and their application in photocatalytic oxidative desulfurization,” Ceram. Int., vol. 40, no. 8, pp. 11627–11635, 2014.

[97] M. H. Liao, C. H. Hsu, and D. H. Chen, “Preparation and properties of amorphous titania-coated zinc oxide nanoparticles,” J. Solid State Chem., vol. 179, no. 7, pp. 2020–2026, 2006.

[98] R. A. Senthil, J. Theerthagiri, A. Selvi, and J. Madhavan, “Synthesis and characterization of low-cost g-C_3N_4/TiO_2 composite with enhanced photocatalytic performance under visible-light irradiation,” Opt. Mater. (Amst)., vol. 64, pp. 533–539, 2017.

[99] G. Liao, S. Chen, X. Quan, H. Yu, and H. Zhao, “Graphene oxide modified g-C_3N_4 hybrid with enhanced photocatalytic capability under visible light irradiation,” J. Mater. Chem., vol. 22, no. 6, pp. 2721–2726, 2012.

[100] C. Wang and J. Yao, “Decolorization of methylene blue with TiO_2 sol via UV irradiation photocatalytic degradation,” Int. J. Photoenergy, vol. 2010, 2010.

[101] G. Song, Z. Chu, W. Jin, and H. Sun, “Enhanced performance of g-C_3N_4/TiO_2 photocatalysts for degradation of organic pollutants under visible light,”

Chinese J. Chem. Eng., vol. 23, no. 8, pp. 1326–1334, 2015.

[102] B. K. Mutuma, G. N. Shao, W. D. Kim, and H. T. Kim, “Sol-gel synthesis of mesoporous anatase-brookite and anatase-brookite-rutile TiO_2 nanoparticles and their photocatalytic properties,” J. Colloid Interface Sci., vol. 442, pp. 1–7, 2015.

[103] S. Gunnar, S. Sommer, A. Lotsari, B. Elgh, B. B. Iversen, and A. E. C. Palmqvist, “Evolution of the Polymorph Selectivity of Titania Formation under Acidic and Low-Temperature Conditions,” 2019.

[104] L. Code, “Dissertation for the degree of Doctor of Philosophy Synthesis, Characterizations and Industrial Applications of g-C_3N_4 based Hybrid Composites Chonbuk National University Graduate School Department of Bionanosystem Engineering By Surya Prasad Adhikari.”

[105] N. Xu, H. Huang, H. Ouyang, and H. Wang, “Preparation of the heterojunction catalyst N-doping carbon quantum dots/P25 and its visible light photocatalytic activity,” Sci. Rep., vol. 9, no. 1, pp. 1–10, 2019.

[106] J. C. Yu, L. Zhang, and J. Yu, “Direct sonochemical preparation and characterization of highly active mesoporous TiO_2 with a bicrystalline framework,” Chem. Mater., vol. 14, no. 11, pp. 4647–4653, 2002.